

**NASA CONTRACTOR
REPORT**

NASA CR-1525



NASA CR-1525

pt. 1
C.1

0060707

TECH LIBRARY KAFB, NM

LOAN COPY: RETURN TO
AFWL (WL-OL)
KIRTLAND AFB, N MEX

**THE EFFECT OF COMPOSITION ON THE
MECHANISM OF STRESS-CORROSION
CRACKING OF TITANIUM ALLOYS IN N_2O_4 ,
AND AQUEOUS AND HOT-SALT ENVIRONMENTS**

*by J. D. Boyd, P. J. Moreland, W. K. Boyd, R. A. Wood,
D. N. Williams, and R. I. Jaffee*

Prepared by
BATTELLE MEMORIAL INSTITUTE
Columbus, Ohio
for

NATIONAL AERONAUTICS AND SPACE ADMINISTRATION • WASHINGTON, D. C. • FEBRUARY 1970



THE EFFECT OF COMPOSITION ON THE MECHANISM OF
STRESS-CORROSION CRACKING OF TITANIUM ALLOYS IN N_2O_4 ,
AND AQUEOUS AND HOT-SALT ENVIRONMENTS

By J. D. Boyd, P. J. Moreland, W. K. Boyd, R. A. Wood,
D. N. Williams, and R. I. Jaffee

Distribution of this report is provided in the interest of
information exchange. Responsibility for the contents
resides in the author or organization that prepared it.

Prepared under Contract No. NASr-100(09) by
BATTELLE MEMORIAL INSTITUTE
Columbus, Ohio

for

NATIONAL AERONAUTICS AND SPACE ADMINISTRATION

For sale by the Clearinghouse for Federal Scientific and Technical Information
Springfield, Virginia 22151 - Price \$3.00

TABLE OF CONTENTS

	<u>Page</u>
SUMMARY	1
TESTING OF EXPERIMENTAL ALLOYS	2
Effect of Composition on Aqueous and Hot-Salt Stress-Corrosion	
Cracking	2
Determination of Critical Aluminum Content	2
Materials and Specimen Preparation	3
Tensile Tests	5
Creep Tests	5
Aqueous Stress-Corrosion Tests	8
Discussion of Results	8
Effect of Heat Treatment on Aqueous and Hot-Salt Stress-Corrosion	
Cracking	15
Beta Processing	15
Solution Treating and Aging	23
Ti ₃ Al Stabilization Treatments	24
MECHANISMS OF STRESS-CORROSION CRACKING	31
Aqueous Environments	31
Crack Velocity Measurements	31
Effect of Specimen Thickness and Strain Rate on Yielding and	
Fracture of Ti-8Al-1Mo-1V in Air and Salt Water	38
Kinetics of Hydrogen Absorption	40
Mechanism of Hydride Nucleation	46
Effect of Hydrogen on the Tensile Properties of Ti-8Al-1Mo-1V	52
Discussion of Results	54
N ₂ O ₄ Environments	58
Chemical Study	58
Fractographic Studies	66
Discussion of Results	75
Future Work on N ₂ O ₄ Cracking Mechanism	77
REFERENCES	78
APPENDIX	
STRESS ANALYSIS IN THREE-POINT LOAD SYSTEM	A-1

THE EFFECT OF COMPOSITION ON THE MECHANISM OF
STRESS-CORROSION CRACKING OF TITANIUM ALLOYS
IN N_2O_4 , AND AQUEOUS AND HOT-SALT ENVIRONMENTS

by

J. D. Boyd, P. J. Moreland, W. K. Boyd, R. A. Wood,
D. N. Williams, and R. I. Jaffee

SUMMARY

A series of Ti-7Al-base alloys has been evaluated for susceptibility to aqueous and hot-salt stress-corrosion cracking. All of the alloys were found to be susceptible to aqueous stress-corrosion cracking. The hot-salt tests were not conclusive and are being repeated. Oxygen has the same effect as aluminum on the susceptibility to aqueous cracking.

To further characterize the Ti-4Al- and Ti-8Al-base alloys studied originally in the annealed-plus-stabilized condition, selected compositions were heat treated and/or processed to evaluate (1) the solution-heat-treated-plus-aged condition, (2) the acicular transformed beta condition, and (3) the stabilized condition which promotes Ti_3Al formation. The solution-heat-treated-and-aged alloys show an inverse relationship between strength and fracture toughness in air and salt water and have the same stress-corrosion characteristics as the equiaxed alloys.

The alloys with acicular microstructures have only marginally better combinations of strength and fracture toughness. However, the effect of stabilizing the ordered Ti_3Al phase is very dramatic. For a given aluminum content, the fracture toughness in air and salt water decreases sharply with an increasing amount of Ti_3Al , but the yield stress does not change appreciably. Apparently the effect of Ti_3Al on the fracture behavior is independent of the yielding process.

In order to clarify the mechanism of aqueous stress-corrosion cracking, a series of specialized experiments has been performed. The kinetics of hydrogen absorption were studied as a function of composition and heat treatment. The mechanism of hydride nucleation in slip bands was investigated further by transmission electron microscopy, and the effects of dissolved hydrogen and hydrides on the mechanical properties of Ti-8Al-1Mo-1V were determined. In addition, environmental effects were studied by measuring subcritical crack growth rate in Ti-8Al-1Mo-1V as a function of stress intensity, temperature, and concentration of chloride ions in the environment. Also, studies were made to determine the stress-strain curves for this alloy for various specimen thicknesses, strain rates, and environments. The mechanism that is most consistent with all the experimental observations presently available is the one outlined in the previous report whereby strain-induced hydrides form in the active $\{10\bar{1}0\}$ slip bands and inhibit plastic flow around the crack tip.

The mechanism of stress-corrosion cracking in N_2O_4 has been clarified by electrochemical and fractographic investigations. Cracking is initiated by electrochemical

attack which produces a transgranular crack. Crack propagation proceeds by intergranular attack, except in the high-strength alloys where transgranular cleavage occurs above a critical stress intensity. The electrochemistry of the reactions between titanium and the N_2O_4 environments has been studied theoretically and experimentally, and a mechanism is proposed.

TESTING OF EXPERIMENTAL ALLOYS

Effect of Composition on Aqueous and Hot-Salt Stress-Corrosion Cracking

Determination of Critical Aluminum Content

The first year's work on this program showed that the composition of the α phase, in particular the aluminum content, largely determines the aqueous stress-corrosion susceptibility of α/β titanium alloys. ^{(1)*} The amount or kind of beta-stabilizer addition has little effect on the susceptibility compared with that of aluminum. In the initial study, a series of alloys representing two aluminum levels was investigated, and it was found that Ti-4Al-base alloys are immune, whereas Ti-8Al-base alloys are susceptible. In order to identify the critical aluminum content associated with the transition from the immune to the susceptible condition, a series of alloys with aluminum contents ranging from 6.0 to 8.0 weight percent was prepared and evaluated. The beta-stabilizer content was 1.5 weight percent Mo and 0.5 weight percent V for each alloy in this series. The alloys were prepared in the form of 350-gram ingots and fabricated to 0.125-inch sheet. The specimen geometry, heat treatment, and testing procedure were the same as before⁽¹⁾, except that longitudinal specimens had to be used because of the limited amount of material available. Table 1 gives the air and salt-water fracture toughness values for each alloy.

From the data in Table 1 it is concluded that the transition from the immune to the susceptible condition occurs near 7.0 weight percent aluminum. The transition is sufficiently gradual that Ti-7.0Al-1.5Mo-0.5V has an intermediate susceptibility to aqueous stress-corrosion cracking. Thus, it is a suitable alloy base to use for identifying the effects of other alloy additions which would normally be masked by the effects of aluminum. Accordingly, a series of Ti-7Al-base alloys was prepared and the following alloy additions were evaluated:

- (1) Beta stabilizers previously evaluated (Mo and V)
- (2) Oxygen
- (3) Palladium
- (4) Manganese.

*References are listed at the end of the report on page 78.

TABLE 1. FRACTURE TOUGHNESS IN AIR AND SALT WATER
AS A FUNCTION OF ALUMINUM CONTENT

Composition, weight percent	Stress Intensity at Fracture, ksi $\sqrt{\text{in.}}$ (a)	
	Air	Salt Water
Ti-4Al-1.5Mo-0.5V(b)	91.7	90.4
Ti-6Al-1.5Mo-0.5V	88.5	77.9
Ti-6.5Al-1.5Mo-0.5V	88.4	74.8
Ti-7.0Al-1.5Mo-0.5V	85.8	50.0
Ti-7.5Al-1.5Mo-0.5V	50.8	31.0
Ti-8.0Al-1.5Mo-0.5V	95.2	38.8
Ti-8.0Al-1.5Mo-0.5V(b)	78.8	16.9

(a) Values obtained after incremental loading.

(b) Transverse values obtained primarily on samples cut from 20 pound heats.

Materials and Specimen Preparation

The 11 experimental alloys for the present study were obtained from the Titanium Metals Corporation of America in the form of double-melted 22-pound ingots. The manufacturer's analyses are given in Table 2, and the Battelle analyses for oxygen and hydrogen on selected alloys are given in Table 3. These materials were fabricated to

TABLE 2. COMPOSITIONS OF EXPERIMENTAL ALLOYS

Alloy	Composition, weight percent	Average Analyses From Ingot Top, Middle, and Bottom, weight percent						
		Al	Mo	V	Fe	O	N	C
977	Ti-7Al-1.5Mo-0.5V(a)	7.19	1.46	0.48	.072	.084	.007	.027
978	Ti-7Al-2Mo(a)	7.08	1.93	--	.073	.105	.007	.023
979	Ti-7Al-2V(a)	6.96	--	1.92	.083	.099	.006	.022
980	Ti-7Al-3Mo-1V(a)	7.10	2.82	0.94	.086	.102	.005	.022
981	Ti-7Al(a)	7.07	--	--	.073	.101	.008	.022
982	Ti-7Al-1.5Mo-0.5V(b)	7.24	1.49	0.50	.075	.233	.007	.022
983	Ti-7Al-1.5Mo-0.5V(c)	7.03	1.44	0.49	.023	.048	.004	.030
984	Ti-6.5Al-1.5Mo-0.5V(a)	6.49	1.51	0.48	.085	.091	.006	.023
985	Ti-6.5Al-1.5Mo-0.5V(b)	6.51	1.51	0.48	.087	.215	.006	.024
986	Ti-7Al-1.5Mo-0.5V-0.208Pd(a, d)	6.87	1.45	0.47	--	.089	.007	.023
987	Ti-7Al-1.85Mn(a, d)	7.03	--	--	.089	.101	.004	.023

(a) Standard oxygen.

(b) High oxygen.

(c) Low oxygen.

(d) Analyses for Pd and Mn are given.

0.25-inch plate and 0.125-inch sheet according to the schedule given in Table 4. The beta transus temperature was determined metallographically as before and a suitable solution annealing temperature was selected for each alloy (Table 5). Coupons for stress corrosion, creep, and tensile tests were annealed to produce an equiaxed- α grain structure comparable to that achieved in the previous studies.⁽¹⁾

TABLE 3. OXYGEN AND HYDROGEN ANALYSIS FOR SELECTED ALLOYS^(a)

Alloy	Composition, weight percent	Oxygen, ppm	Hydrogen, ppm
983	Ti-7Al-1.5Mo-0.5V (low O)	590	24
977	Ti-7Al-1.5Mo-0.5V (std. O)	900	27
982	Ti-7Al-1.5Mo-0.5V (high O)	2500	18
984	Ti-6.5Al-1.5Mo-0.5V (std. O)	935	21
985	Ti-6.5Al-1.5Mo-0.5V (high O)	2100	16

(a) Analyses made after vacuum anneal.

TABLE 4. FABRICATION SCHEDULE FOR EXPERIMENTAL ALLOYS

Alloy	Composition, weight percent	Press Forging		Cross and Direct Rolling to 7" Width ^(a)		Direct Rolling		
		Temp, F	Thickness, inch	Temp, F	Thickness, inch	To 1/2" Thick ^(a)	To 1/4" Thick ^(b)	To 1/8" Thick
						Temp, F	Temp, F	Temp, F
977	Ti-7Al-1.5Mo-0.5V	2000	2	1800	1	1720	1670	1620
978	Ti-7Al-2Mo	2000	2	1800	1	1720	1670	1620
979	Ti-7Al-2V	2000	2	1800	1	1720	1670	1620
980	Ti-7Al-3Mo-1V	2000	2	1750	1	1680	1650	1600
981	Ti-7Al	2000	2	1800	1	1720	1670	1620
982	Ti-7Al-1.5Mo-0.5V (HiOx)	2000	2	1800	1	1720	1670	1620
983	Ti-7Al-1.5Mo-0.5V (LoOx)	2000	2	1800	1	1720	1670	1620
984	Ti-6.5Al-1.5Mo-0.5V	2000	2	1750	1	1680	1650	1600
985	Ti-6.5Al-1.5Mo-0.5V (HiOx)	2000	2	1750	1	1680	1650	1600
986	Ti-7Al-1.5Mo-0.5V-0.2Pd	2000	2	1800	1	1720	1670	1620
987	Ti-7Al-2Mn	2000	2	1800	1	1720	1670	1620

(a) All material from each heat subsequently rolled to 0.25-inch plate.

(b) One-half length of 0.25-inch plates subsequently rolled to 0.125-inch sheet.

TABLE 5. BETA TRANSUS TEMPERATURES AND
SOLUTION-ANNEALING TEMPERATURES
OF EXPERIMENTAL ALLOYS

Alloy	Composition, weight percent	Beta Transus Temp, F	Solution Annealing Temp, F
977	Ti-7Al-1.5Mo-0.5V(a)	1910	1785
978	Ti-7Al-2Mo(a)	1880	1785
979	Ti-7Al-2V(a)	1890	1785
980	Ti-7Al-3Mo-1V(a)	1880	1725
981	Ti-7Al(a)	1910	1725
982	Ti-7Al-1.5Mo-0.5V (high O)	1960	1850
983	Ti-7Al-1.5Mo-0.5V (low O)	1880	1775
984	Ti-6.5Al-1.5Mo-0.5V(a)	1870	1775
985	Ti-6.5Al-1.5Mo-0.5V (high O)	1930	1785
986	Ti-7Al-1.5Mo-0.5V-0.2Pd(a)	1910	1785
987	Ti-7Al-2Mn(a)	1880	1785

(a) Standard oxygen ≈ 0.1 percent.

Tensile Tests

The room-temperature tensile data obtained for this series of alloys are given in Table 6. In addition, tensile tests were run on samples which had been creep-exposed at 600 F. The room-temperature tensile properties of the specimens which had been creep-exposed without salt (Table 7) afford a measurement of the alloys' metallurgical stability. The average room-temperature tensile properties from Table 6 are included in Table 7 for comparison. Although the short-term, 600 F creep exposure is not particularly severe, appreciable plastic strain was obtained (between 0.14 and 2.94 percent, see Table 8). Since creep exposure has little effect on tensile ductility, it may be concluded that the materials are metallurgically stable after creep at 600 F.

Creep Tests

Specimens of each alloy were exposed under load at 600 F in order to determine stress levels which would produce 0.2 to 1.0 percent plastic creep strain during exposure times of 50 to 100 hours. Unfortunately, the initial choice of stress levels was generally too high and most of the specimens were overstrained, although third-stage creep was not experienced (Table 8). Therefore, the creep tests will be repeated on duplicate specimens at more suitable stresses, and the adjusted exposure conditions will be used for the hot-salt stress-corrosion evaluation.

TABLE 6. ROOM-TEMPERATURE TENSILE PROPERTIES FOR
EXPERIMENTAL ALLOYS AS ANNEALED^(a)

Alloy	Composition, weight percent	Solution Temp, F	Yield Stress, ksi	Ultimate Stress, ksi	Elongation, percent	Reduction in Area, percent
977	Ti-7Al-1.5Mo-0.5V-0.1 O ₂	1785	123.6	136.1	15	29
		1785	121.7	134.5	15	31
978	Ti-7Al-2Mo-0.1 O ₂	1785	123.2	135.8	14	30
		1785	123.3	136.8	16	30
979	Ti-7Al-2V-0.1 O ₂	1785	112.8	119.7	16	26
		1785	110.2	117.3	15	39
980	Ti-7Al-3Mo-1V-0.1 O ₂	1725	133.9	149.3	17	33
		1725	133.6	148.5	16	31
981	Ti-7Al-0.1 O ₂	1725	92.4	96.0	24	37
		1725	92.2	95.3	22	38
982	Ti-7Al-1.5Mo-0.5V-0.23 O ₂	1850	133.4	148.4	15	27
		1850	135.7	145.7	6	12
983	Ti-7Al-1.5Mo-0.5V-0.05 O ₂	1775	116.6	128.9	16	30
		1775	115.0	125.5	15	24
984	Ti-6.5Al-1.5Mo-0.5V-0.1 O ₂	1775	114.9	122.9	13	27
		1775	115.4	123.2	15	26
985	Ti-6.5Al-1.5Mo-0.5V-0.22 O ₂	1785	129.9	140.0	12	17
		1785	129.9	139.0	13	22
986	Ti-7Al-1.5Mo-0.5V-0.2Pd	1785	120.8	131.9	12	22
		1785	120.0	131.3	15	33
987	Ti-7Al-2Mn-0.1 O ₂	1785	125.0	137.2	16	26
		1785	124.1	137.1	16	26

(a) Transverse samples.

TABLE 7. ROOM-TEMPERATURE TENSILE PROPERTIES FOR TRANSVERSE SAMPLES OF EXPERIMENTAL ALLOYS BEFORE AND AFTER 600 F CREEP EXPOSURE^(a)

Alloy	Composition, weight percent	Creep Exposure	Yield Stress, ksi	Ultimate Stress, ksi	Elonga- tion, percent	Reduction in Area, percent
977	Ti-7Al-1.5Mo-0.5V	No	122.6	135.3	15	30
		Yes	126.6	138.2	13	33
978	Ti-7Al-2Mo	No	123.2	136.3	15	30
		Yes	129.2	141.9	13	26
979	Ti-7Al-2V	No	111.5	118.5	15	28
		Yes	114.2	121.3	14	25
980	Ti-7Al-3Mo-1V	No	133.7	148.9	16	32
		Yes	136.2	165.1	17	32
981	Ti-7Al	No	92.3	95.7	23	38
		Yes	91.6	97.8	23	37
982	Ti-7Al-1.5Mo-0.5V (High O)	No	134.5	147.0	11	20
		Yes	147.1	157.3	13	26
983	Ti-7Al-1.5Mo-0.5V (Low O)	No	115.8	127.2	15	27
		Yes	119.1	129.6	15	26
984	Ti-6.5Al-1.5Mo-0.5V	No	115.1	123.0	14	26
		Yes	120.8	127.8	10	19
985	Ti-6.5Al-1.5Mo-0.5V (High O)	No	129.9	139.5	12	20
		Yes	137.1	143.9	11	20
986	Ti-7Al-1.5Mo-0.5V-0.2Pd	No	120.4	131.6	14	28
		Yes	130.8	141.6	14	24
987	Ti-7Al-2Mn	No	124.6	137.1	16	26
		Yes	124.0	136.8	13	26

(a) See Table 8 for details of creep exposure.

TABLE 8. 600 F CREEP DATA

Alloy	Composition, weight percent	600 F Creep Exposure		Strain, percent	
		Stress, ksi	Time, hr	Total(a)	Total Plastic(b)
977	Ti-7Al-1.5Mo-0.5V	90	69.4	2.920	2.230
978	Ti-7Al-2Mo	90	69.3	2.250	1.610
979	Ti-7Al-2V	85	(Failed on loading)		
		75	93.1	1.800	1.260
980	Ti-7Al-3Mo-1V	96	93.0	0.895	0.305
981	Ti-7Al	50	91.4	0.595	0.233
982	Ti-7Al-1.5Mo-0.5V (High O)	96	91.0	3.580	2.940
983	Ti-7Al-1.5Mo-0.5V (Low O)	82	90.6	1.540	1.000
984	Ti-6.5Al-1.5Mo-0.5V	80	93.2	2.790	2.240
985	Ti-6.5Al-1.5Mo-0.5V (High O)	85	90.8	2.640	2.050
986	Ti-7Al-1.5Mo-0.5V-0.2Pd	85	90.8	1.430	0.867
987	Ti-7Al-2Mn	85	90.8	0.657	0.143

(a) Strain measured immediately prior to unloading.

(b) Load-off measurement.

Aqueous Stress-Corrosion Tests

The experimental alloys were evaluated for susceptibility to aqueous stress-corrosion cracking by means of the single-edge-notched cantilever tests, as described previously. (1) The critical stress intensities to produce crack propagation in air and in salt water (3.5 percent NaCl) are given in Table 9. Testing was routine except in two cases. The Ti-7Al binary alloy was very resistant to cracking in air, necessitating a deep fatigue crack to prevent sample twisting, and the low oxygen content alloy of Ti-7Al-1.5Mo-0.5V (No. 983) behaved erratically in the constant-load tests, perhaps indicating some localized segregation. A photomicrograph of a typical aqueous stress-corrosion crack is shown in Figure 1.

Discussion of Results

When comparing the various alloys it is useful to consider together yield stress, toughness in air, and toughness in salt water. It should be pointed out that the state of stress during fracture was not the same for each alloy. For the single-edge-cracked cantilever test, plane-strain conditions obtain when a specimen thickness of more than $2.5 (K_C/\sigma_y)^2$ is tested. Since the specimens used in this study were 0.125 inches thick, the fracture toughness values are true plane-strain values only for those cases where K_C is less than $0.2 \sigma_y$. For example, air tests are predominantly plane-stress or mixed-mode failures, while the salt-water tests are predominantly mixed-mode. Although these test values cannot be used to predict the behavior of the alloys under actual service conditions, it is valid to compare alloying effects on a qualitative basis.

The Ti-7Al-base alloys turned out to be much more susceptible to aqueous stress-corrosion cracking than predicted by the preliminary results obtained on material from small heats. The Ti-6.5Al-base alloys also are quite susceptible as shown by the tabulation at the top of page 12.

TABLE 9. FRACTURE TOUGHNESS DATA IN AIR AND 3.5 PERCENT NaCl
(Step-Loaded and Constant-Load Tests on Transverse Samples)

Alloy	Composition, weight percent	Environment	Loading Method	Stress Intensity, ksi $\sqrt{\text{in.}}$	Total Exposure Time, min
977	Ti-7Al-1.5Mo-.5V	Air	Step	84.0	27
		Salt water	Step	24.4	11
		Salt water	Constant	21.6	5
		Salt water	Constant	18.9	360(a)
978	Ti-7Al-2Mo	Air	Step	71.8	20
		Salt water	Step	20.7	8
		Salt water	Step	23.0	16
		Salt water	Constant	22.7	4
		Salt water	Constant	20.2	360(a)
		Salt water	Constant	17.8	360(a)
979	Ti-7Al-2V	Air	Step	107.8	40
		Salt water	Step	29.4	6
		Salt water	Constant	28.4	5
		Salt water	Constant	27.3	360(a)
980	Ti-7Al-3Mo-1V	Air	Step	55.9	10
		Salt water	Step	22.0	10
		Salt water	Constant	24.2	<2
		Salt water	Constant	20.0	3
		Salt water	Constant	17.1	360(a)
981	Ti-7Al	Air	Step	104.3	34(b)
		Air	Step	92.5	23
		Salt water	Step	32.5	3
		Salt water	Constant	30.2	3
		Salt water	Constant	28.3	4
		Salt water	Constant	24.8	360(a)
982	Ti-7Al-1.5Mo-.5V (High O)	Air	Step	52.3	7
		Salt water	Step	16.2	7
		Salt water	Step	18.7	7
		Salt water	Constant	18.2	3
		Salt water	Constant	31.1	<1
		Salt water	Constant	15.5	360(a)
		Salt water	Constant	13.1	360(a)

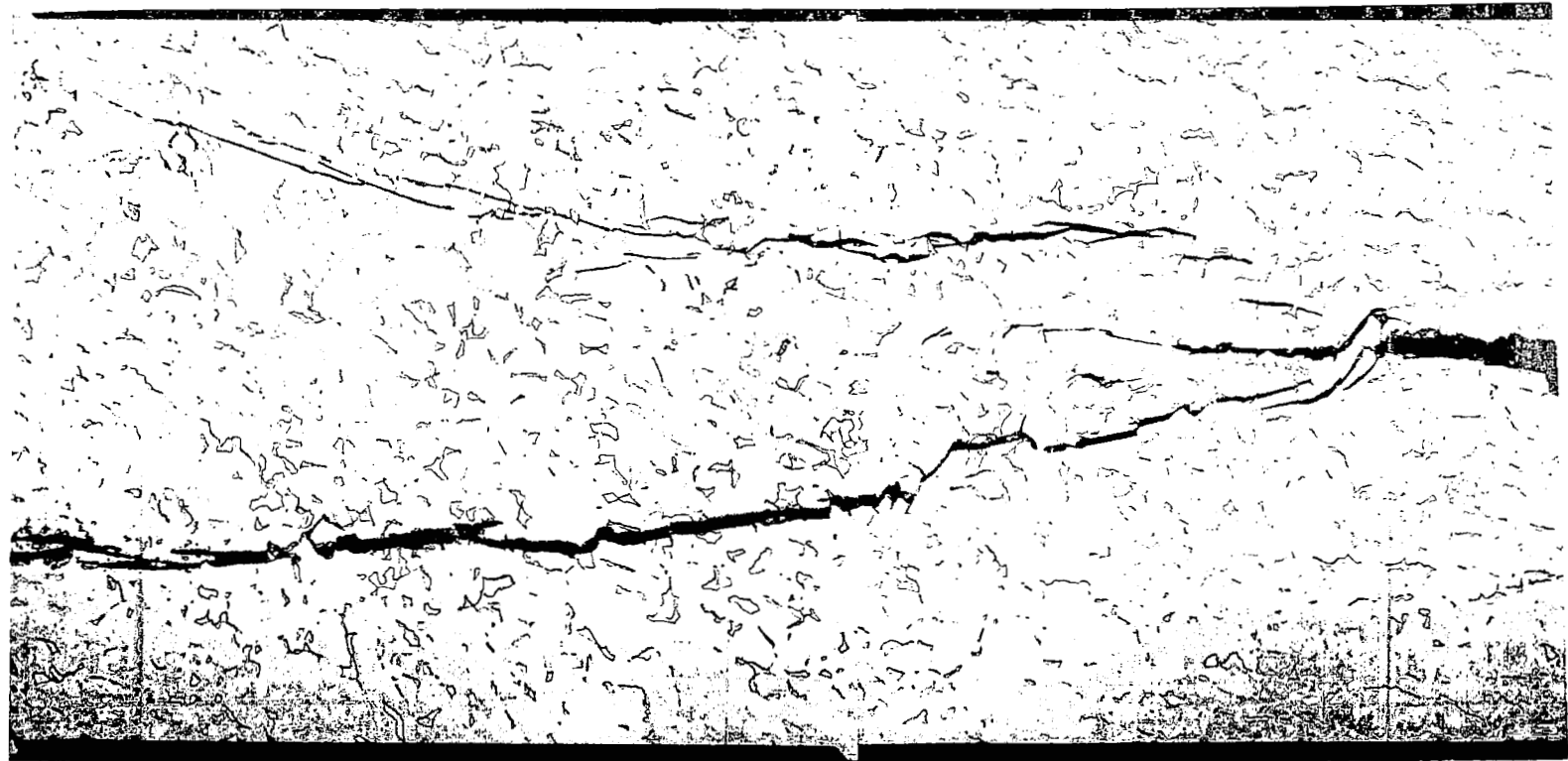
TABLE 9. (Continued)

Alloy	Composition, weight percent	Environment	Loading Method	Stress Intensity, ksi√in.	Total Exposure Time, min
983	Ti-7Al-1.5Mo-.5V (Low O)	Air	Step	93.8	33
		Salt water	Step	58.2	52
		Salt water	Step	57.6	52
		Salt water	Constant	54.7	3
		Salt water	Constant	51.4	10
		Salt water	Constant	47.7	193
		Salt water	Constant	45.1	42
		Salt water	Constant	42.8	7
		Salt water	Constant	35.7	68
		Salt water	Constant	28.7	360(c)
		Salt water	Constant	26.8	360(c)
		Salt water	Constant	32.5	360(c)
		Salt water	Constant	36.3	360(c)
		Salt water	Constant	41.9	360(c)
		Salt water	Constant	49.4	5
984	Ti-6.5Al-1.5Mo-.5V	Air	Step	92.0	28
		Salt water	Step	34.7	8
		Salt water	Constant	32.2	4
		Salt water	Constant	30.2	360(a)
985	Ti-6.5Al-1.5Mo-.5V (High O)	Air	Step	55.5	11
		Salt water	Step	19.9	8
		Salt water	Constant	17.6	4
		Salt water	Constant	16.0	360(a)
986	Ti-7Al-1.5Mo-.5V- .2Pd	Air	Step	92.8	30
		Salt water	Step	26.7	4
		Salt water	Constant	24.0	5
		Salt water	Constant	21.5	290
		Salt water	Constant	20.2	360(a)
987	Ti-7Al-2Mn	Air	Step	60.7	13
		Salt water	Step	16.5	4
		Salt water	Constant	15.9	53
		Salt water	Constant	14.9	360(a)

(a) Sample did not fail - removed from test.

(b) Sample twisted in test rig - removed from test. A second sample was cracked in fatigue to a greater depth and successfully tested.

(c) Load increased on same sample after 360 minute exposure.



Direction of
Crack
Propagation



500 X

Rolling
Direction



7D922 and 7D923

FIGURE 1. PHOTOMICROGRAPH OF AQUEOUS STRESS-CORROSION CRACK
IN Ti-7Al-1.5Mo-0.5V (CROSS SECTION)

Note transgranular path of crack through alpha grains but
devious path of crack around beta grains.

Alloy	Composition, weight percent	Yield Stress, ksi	Ultimate Stress, ksi	Elongation, percent	Reduction in Area, percent	Stress Intensity, ksi $\sqrt{\text{in.}}$	
						Air	Salt Water
72	Ti-4Al-1.5Mo- 0.5V-0.1 O ₂	102	107	20	36	92	83
984	Ti-6.5Al-1.5Mo- 0.5V-0.1 O ₂	115	123	14	27	92	31
977	Ti-7Al-1.5Mo- 0.5V-0.1 O ₂	123	135	15	30	84	20
77	Ti-8Al-1.5Mo- 0.5V-0.1 O ₂	130	146	18	28	79	15

The data obtained on small heats are (from Table 1):

--	Ti-6Al-1.5Mo- 0.5V-0.1 O ₂	--	--	--	--	88	78
--	Ti-6.5Al-1.5Mo- 0.5V-0.1 O ₂	--	--	--	--	88	75
--	Ti-7.0Al-1.5Mo- 0.5V-0.1 O ₂	--	--	--	--	86	50
--	Ti-7.5Al-1.5Mo- 0.5V-0.1 O ₂	--	--	--	--	50	31

The air toughness and aqueous stress-corrosion susceptibility differences observed between these two series of similar compositions are probably due to directionality and to differences in interstitial content. Therefore, in the current study of Ti-6.5Al- and Ti-7Al-base alloys, a series of susceptible alloys is being evaluated. Presumably, marginal susceptibility would then be found at an aluminum content lower than 6.5 percent with other variables unchanged.

The absolute values obtained for yield stress and toughness of the new compositions fit well within the range of values determined previously for lower and higher aluminum-content alloys. Generally, strength increases and toughness decreases with increasing aluminum content. Tensile and toughness data for the Ti-7Al binary alloy are shown below in comparison with the Ti-4Al and Ti-8Al results.

Alloy	Composition, weight percent	Yield Stress, ksi	Ultimate Stress, ksi	Elongation, percent	Reduction in Area, percent	Stress Intensity, ksi $\sqrt{\text{in.}}$	
						Air	Salt Water
67	Ti-4Al	67	79	22	42	86	82
981	Ti-7Al	92	96	23	38	93	28
73	Ti-8Al	100	101	25	36	96	27

Increasing strength level with increasing aluminum content is found, as expected. The unexpected relationship between increasing air toughness with increasing aluminum content is believed due to the inability to test for true air toughness using thin (0.125 in.)

samples at relatively low strength levels (≤ 100 ksi). The salt-water toughness values show the susceptibility of the Ti-7Al and 8Al alloys.

Both aluminum and oxygen additions predictably increase the strengths of Ti-1.5Mo-0.5V-base alloys as shown in Figure 2. The same effect would be expected in alloys with other but similar beta-stabilizer content. Oxygen additions to the alloys also decrease air and salt-water toughness as expected (Figure 3). Here it is observed that by lowering the oxygen content, compositions having susceptible aluminum content (e. g., Ti-7Al base) can be made less susceptible to salt-water stress-corrosion cracking. Extrapolation of the Ti-7Al-base alloy data of Figure 3 would indicate a very large improvement in salt-water toughness at an oxygen level of 300 ppm or below. The data on the effect of oxygen are tabulated below.

Alloy	Composition, weight percent (Balance Ti-1.5Mo-0.5V)	Yield Stress, ksi	Ulti- mate Stress, ksi	Elonga- tion, percent	Reduction in Area, percent	Stress Intensity, ksi $\sqrt{\text{in.}}$	
						Air	Salt Water
72	4.0Al-0.1000 O ₂	102	107	20	36	92	83
984	6.5Al-0.0935 O ₂	115	123	14	27	92	31
985	6.5Al-0.2100 O ₂	130	140	12	20	56	17
983	7.0Al-0.0590 O ₂	116	127	15	27	94	42
977	7.0Al-0.0900 O ₂	123	135	15	30	84	20
982	7.0Al-0.2500 O ₂	134	147	11	20	52	16
77	8.0Al-0.1000 O ₂	130	146	18	28	79	15

The effect of increasing aluminum content on the properties of alloys having a similar beta-stabilizer content is further illustrated by the data obtained with the 3Mo-1V, 2-4Mo, and 2-4V series.

Alloy	Composition, weight percent	Yield Stress, ksi	Ultimate Stress, ksi	Elongation, percent	Reduction in Area, percent	Stress Intensity, ksi $\sqrt{\text{in.}}$	
						Air	Salt Water
70	Ti-4Al-3Mo-1V	114	119	17	46	95	88
980	Ti-7Al-3Mo-1V	134	149	17	32	56	18
74	Ti-8Al-3Mo-1V	140	158	20	24	55	13
68	Ti-4Al-4Mo	110	116	18	44	93	86
978	Ti-7Al-2Mo	123	136	15	30	72	22
21	Ti-8Al-2Mo	138	152	17	24	65	21
69	Ti-4Al-4V	106	112	20	42	88	86
979	Ti-7Al-2V	112	119	16	27	108	28
76	Ti-8Al-2V	118	127	13	22	102	23

These data again show the effect of aluminum to increase strength, usually accompanied by decreasing ductility and toughness, and further illustrate that the Ti-7Al-base is a susceptible (to aqueous stress-corrosion) composition.

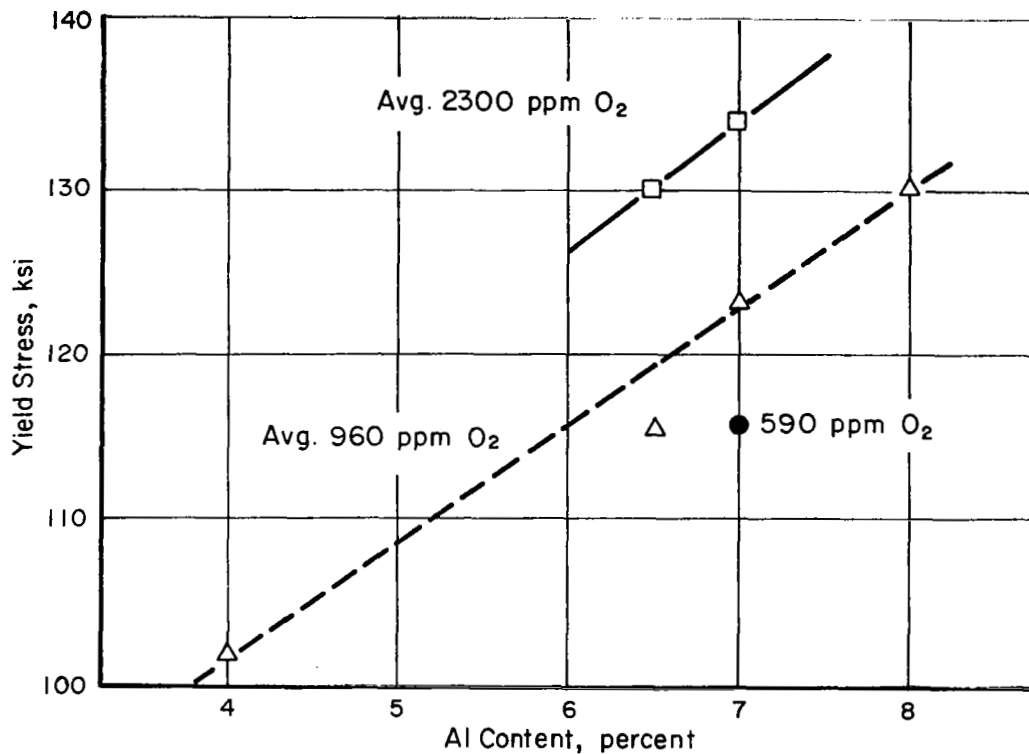


FIGURE 2. EFFECT OF ALUMINUM AND OXYGEN ADDITIONS ON THE YIELD STRESS OF Ti-1.5Mo-0.5V-BASE ALLOY

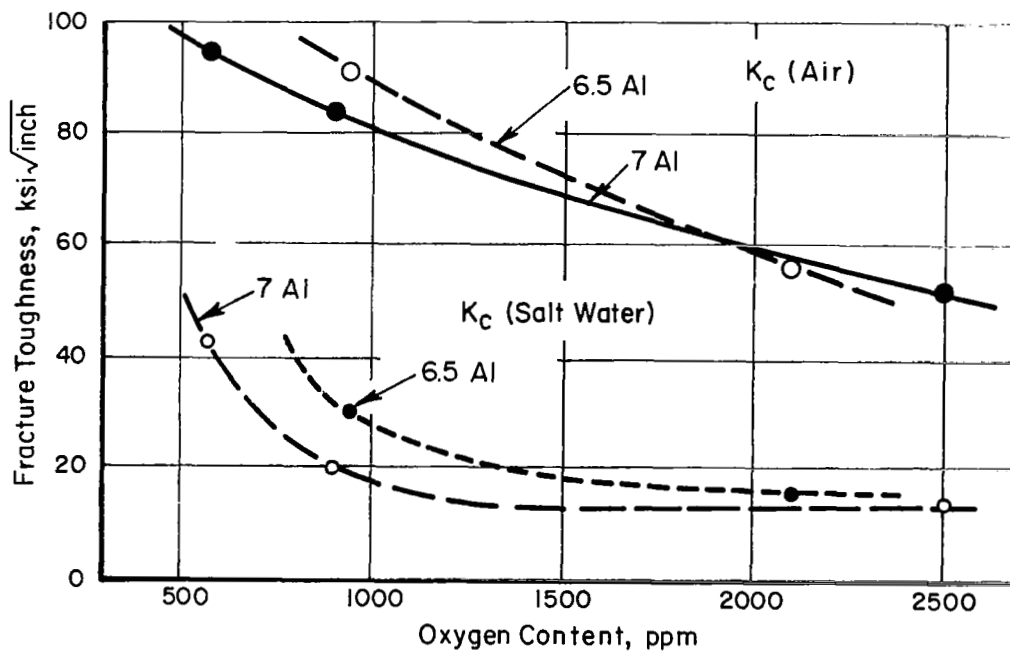


FIGURE 3. EFFECT OF OXYGEN CONTENT ON THE TOUGHNESS OF Ti-7Al-1.5Mo-0.5V AND Ti-6.5Al-1.5Mo-0.5V

The effect of the various beta-stabilizer contents on the properties of the Ti-7Al-base alloy are approximately as expected. Yield-stress-toughness relationships for selected alloys are shown in Figure 4. Vanadium is a weak beta stabilizer compared with molybdenum and this is reflected in the strength and toughness levels found. Although the 2 percent vanadium content alloy has a better salt-water toughness than the molybdenum-containing alloys, the effect is believed to be due to the lower strength of the vanadium alloy. Manganese is quite potent in promoting strength, equivalent to molybdenum for example, but renders the Ti-7Al-base less tough than molybdenum- and vanadium-containing alloys at equivalent strength levels. Manganese makes the material susceptible to salt-water stress-corrosion cracking to a marked degree. The addition of palladium to the Ti-7Al-1.5Mo-0.5V alloy does not appear to benefit the material for salt-water toughness although the air toughness is improved over the base alloy. As in earlier work, the 3Mo-1V combination is shown to have the highest strength but at this strength level the alloy is not very tough in air or salt water. A tabulation of the data for these alloys is included for convenience.

Alloy	Composition, weight percent (Balance Ti-7Al)	Yield Stress, ksi	Ultimate Stress, ksi	Elongation, percent	Reduction in Area, percent	Stress Intensity, ksi√in.	
						Air	Salt Water
979	2V	111	118	15	28	108	28
978	2Mo	123	136	15	30	72	21
987	2Mn	124	136	16	26	31	15
977	1.5Mo-0.5V	123	135	15	30	84	20
986	1.5Mo-0.5V-0.2Pd	120	132	14	27	93	21
980	3Mo-1V	134	149	17	32	56	18

The effect of beta stabilizers at different aluminum levels is illustrated graphically in Figure 5. Clearly, additions of beta stabilizers to binary Ti-Al increase the yield stress at all aluminum levels, but the resistance to aqueous stress corrosion cracking is principally determined by the aluminum content. Effects of beta stabilizers may be illustrated in an aluminum level which gives marginal susceptibility, but in the alloys investigated to date the aluminum content is the dominant factor.

Effect of Heat Treatment on Aqueous and Hot-Salt Stress-Corrosion Cracking

To further characterize the Ti-4Al- and Ti-8Al-base alloys studied originally in the annealed-plus-stabilized condition, selected compositions were heat treated and/or processed to evaluate the solution-heat-treated-plus-aged condition, the acicular transformed beta condition, and the stabilized condition which promotes Ti₃Al formation. Tensile, hardness, creep, creep-stability, hot-salt stress-corrosion, and aqueous stress-corrosion susceptibility tests were conducted to afford a comprehensive evaluation of the alloys in these special conditions.

Beta Processing

Selected compositions of Ti-4Al- and Ti-8Al-base alloys available from the previous investigations were either beta annealed (after standard processing and annealing), or beta fabricated. The beta fabrication schedule is given in Table 10. In each case the

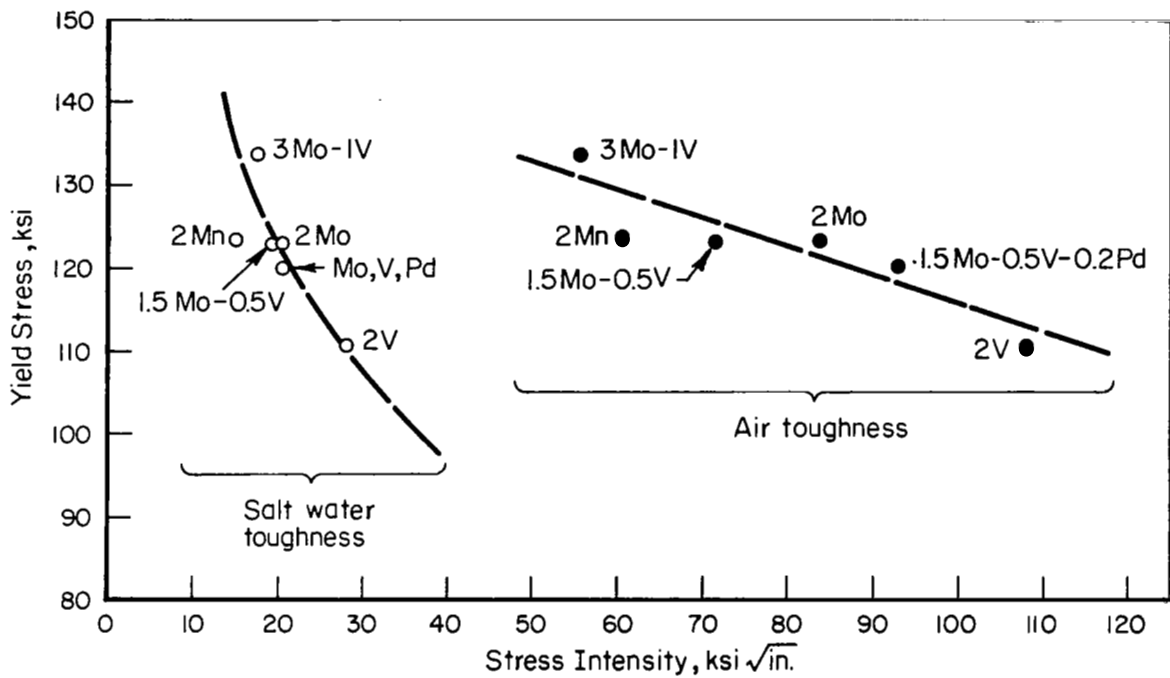


FIGURE 4. YIELD-STRESS-TOUGHNESS RELATIONSHIPS OF SELECTED Ti-7Al-BASE ALLOYS

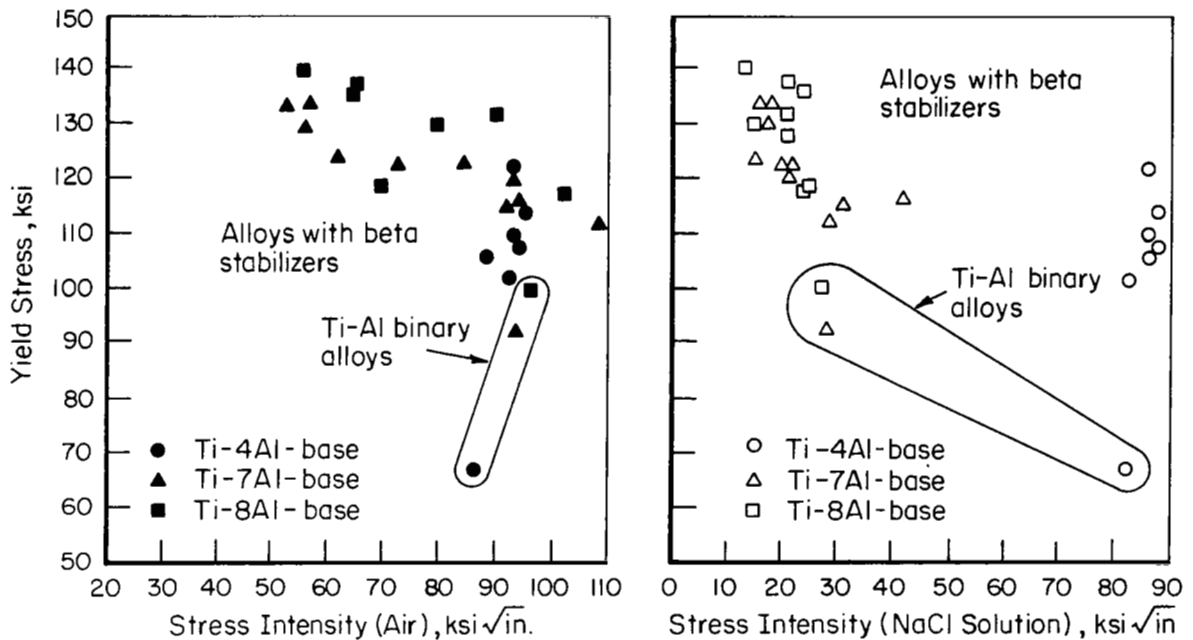


FIGURE 5. YIELD-STRESS-TOUGHNESS RELATIONSHIPS FOR ALL EXPERIMENTAL ALLOYS

beta-annealing temperatures were 50 F below the beta-fabrication temperature. Following both types of beta processing, the materials were solution heat treated and overaged. Room-temperature tensile and aqueous stress-corrosion tests were carried out, and the results are summarized in Table 11.

TABLE 10. BETA FABRICATION SCHEDULE FOR
Ti-4Al AND Ti-8Al-BASE ALLOYS

Alloy	Composition, weight percent	Beta Transus Temp, F	Beta (Rolling) Fabrication Temp, F*
70	Ti-4Al-3Mo-1V	1675	1775
74	Ti-8Al-3Mo-1V	1810	1910
78	Ti-8Al-1Mo-1V	1860	1960

*Samples rolled from 0.25-inch plate to 0.125-inch sheet in 6 passes with reheating to indicated temperature between each pass.

In general, the alloys with acicular microstructures have only marginally better combinations of strength and fracture toughness compared with those having equiaxed grains. Furthermore, susceptibility to aqueous stress-corrosion cracking is not changed significantly. The greatest improvement in air toughness is found for Ti-8Al-1Mo-1V. However, the beta conditioning of this alloy does not notably improve its salt-water toughness. The Ti-8Al-3Mo-1V alloy shows the biggest improvements in salt-water fracture toughness following the beta processing. There does not appear to be an appreciable difference in properties between beta-heat-treated material and beta-fabricated material when a final alpha-beta solution-treatment-plus-aging treatment is employed.

The results of these processing studies are summarized below.

Alloy	Composition, weight percent	Condition	Yield Stress, ksi	Stress Intensity, ksi $\sqrt{\text{in.}}$	
				Air	Salt Water
70	Ti-4Al-3Mo-1V	Standard anneal	114	94.9	88.2
		Beta fabricated ^(a)	115	106.3	98.5
		Beta heat treated ^(a)	118	100.3	92.1
78	Ti-8Al-1Mo-1V	Standard anneal	136	64.4	24.0
		Beta fabricated ^(a)	139	98.5	22.8
		Beta heat treated ^(a)	134	95.2	28.9
74	Ti-8Al-3Mo-1V	Standard anneal	140	54.9	14.0
		Beta fabricated ^(a)	161	59.0	12.0
		Beta heat treated ^(a)	156	59.7	22.2
		Alpha-beta heat treated ^(b)	164	23.6	13.8

(a) Aged 16 hours at 1200 F after alpha-beta solution heat treatment.

(b) Aged 24 hours at 1200 F after alpha-beta solution heat treatment.

TABLE 11. ROOM-TEMPERATURE TENSILE AND AQUEOUS STRESS-CORROSION DATA
FOR BETA PROCESSED AND OVERAGED ALLOYS^(a)

Alloy	Composition, weight percent	Processing and Heat Treatment ^(b)	Fracture Toughness				Room-Temperature Tensile			
			Environment ^(c)	Loading Method ^(d)	Stress Intensity for Failure, ksi $\sqrt{\text{in.}}$	Total Exposure Time, min	0.2 Percent Offset Yield Stress, ksi	Ultimate Stress, ksi	Elongation in 1 Inch, percent	Reduction in Area, percent
70	Ti-4Al-3Mo-1V	Beta rolled + (1/4) 1650 F, WQ + (16) 1200 F, AC	Air	Step	106.3	67	114	129	16	38
			SW	Step	105.9	58	116	130	16	37
			SW	C	102.0	5				
			SW	C	95.0 ^(e)	360 ^(e)				
		Critical or average values	SW	C	98.5	—	115	129	16	37
		Beta annealed + (1/4) 1650 F, WQ + (16) 1200 F, AC	Air	Step	100.3	45	118	129	17	42
			SW	Step	97.8	42	119	133	17	38
			SW	C	93.9	45				
			SW	C	90.3 ^(e)	360 ^(e)				
		Critical or average values	SW	C	92.1	—	118	131	17	40
		Standard processing and annealing ^(f)	Air	Step	94.9	187				
			SW	Step	92.8	173				
			SW	C	89.3	12				
			SW	C	87.2 ^(e)	360 ^(e)				
		Critical or average values	SW	C	88.25	—	114	119	16	46
74	Ti-8Al-3Mo-1V	Beta rolled + (1/4) 1750 F, WQ + (16) 1200 F, AC	Air	Step	59.0	31	163	181	7	13
			SW	Step	22.5	12	159	176	7	13
			SW	C	21.9	19				
			SW	C	20.2 ^(e)	360 ^(e)				
		Critical or average values	SW	C	21.05	—	161	178	7	13
		Beta annealed + (1/4) 1750 F, WQ + (16) 1200 F, AC	Air	Step	59.7	27	150	177	10	19
			SW	Step	23.2	17	163	181	8	15
			SW	C	22.8	3				
			SW	C	21.7 ^(e)	360 ^(e)				
		Critical or average values	SW	C	22.25	—	156	179	9	17

TABLE 11. (Continued)

Alloy	Composition, weight percent	Processing and Heat Treatment ^(b)	Fracture Toughness				Room-Temperature Tensile			
			Environment ^(c)	Loading Method ^(d)	Stress Intensity for Failure, ksi./in.	Total Exposure Time, min	0.2 Percent Offset Yield Stress, ksi	Ultimate Stress, ksi	Elongation in 1 Inch, percent	Reduction in Area, percent
74	Ti-8Al-3Mo-1V	Standard processing and annealing ^(f)	Air	Step	54.9	101				
			SW	Step	13.3	17				
			SW	C	15.6	3				
			SW	C	12.5 ^(e)	360 ^(e)				
			Critical or average values	SW	C	14.05	—	140	158	20
78	Ti-8Al-1Mo-1V	Beta rolled + (1/4) 1775 F, WQ + (16) 1200 F, AC	Air	Step	98.5	52	139	159	15	18
			SW	Step	24.1	10	139	157	13	19
			SW	C	23.4	5				
			SW	C	22.2 ^(e)	360 ^(e)				
			Critical or average values	SW	C	22.8	—	139	158	14
		Beta annealed + (1/4) 1775 F, WQ + (16) 1200 F, AC	Air	Step	95.2	45	134	159	16	29
			SW	Step	26.2	23	135	152	10	14
			SW	C	31.4	60				
			SW	C	26.4 ^(e)	360 ^(e)				
			Critical or average values	SW	C	28.9	—	134	155	13
		Standard processing and annealing ^(f)	Air	Step	64.4	101				
			SW	Step	25.0	44				
			SW	C	24.3	23				
			SW	C	23.6 ^(e)	360 ^(e)				
			Critical or average values	SW	C	24.0	—	136	149	16

(a) 1/8-inch thick, transverse samples.

(b) Numbers in parentheses are hours exposure. WQ = water quench, AC = air cool.

(c) SW = 3, 5% of NaCl solution.

(d) C = constant load tests.

(e) No failure in 360 minutes. Test discontinued.

(f) Prior data.

The creep behavior, creep stability, and hot-salt stress corrosion susceptibility of the acicularized alloys was investigated by means of the standard 600 F creep tests with and without salt coatings. The results are given in Table 12.

Beta processing results in an increase in room-temperature strength and 600 F creep strength of these materials as shown below.

<u>Condition</u>	<u>Yield Stress, ksi</u>	<u>Ultimate Stress, ksi</u>	<u>Elongation, percent</u>	<u>Reduction in Area, percent</u>	<u>Creep Strain, percent</u>	<u>Creep Stress, ksi</u>
<u>Ti-4Al-3Mo-1V</u>						
1 Standard anneal	114	119	16	46	0.30-0.47	70
2 β processed	115	129	16	37	0.17-0.31	73-74
3 β heat treated	118	131	17	40	0.21	73
<u>Ti-8Al-3Mo-1V</u>						
1 Standard anneal	140	158	20	24	0.20-0.24	105-109
2 β processed	161	178	7	13	0.06-0.11	110-114
3 β heat treated	156	179	9	17	0.05-0.12	110-115
<u>Ti-8Al-1Mo-1V</u>						
1 Standard anneal	136	149	16	21	0.40-0.52	90-95
2 β processed	139	158	14	18	0.05-2.82	90-114
3 β heat treated	134	155	13	21	0.12	90

Where strength is greatly increased, e.g., Ti-8Al-3Mo-1V, tensile ductility shows a corresponding decrease. The materials with acicular microstructure show an improved 600 F creep strength as expected. This effect is most pronounced in the Ti-8Al-3Mo-1V alloy, the material which also shows the greatest increase in tensile strength. The creep stability of the acicularized materials compares very favorably with the stability of the previously examined equiaxed materials (condition 1, standard anneal).

<u>Condition</u>	<u>Before Creep</u>		<u>After Creep</u>	
	<u>Yield Stress, ksi</u>	<u>Elongation, percent</u>	<u>Yield Stress, ksi</u>	<u>Elongation, percent</u>
<u>Ti-4Al-3Mo-1V</u>				
1 Standard anneal	114	16	112	16
2 β processed	115	16	121	14
3 β heat treated	118	17	120	16
<u>Ti-8Al-3Mo-1V</u>				
1 Standard anneal	140	20	144	18
2 β processed	161	7	164	7
3 β heat treated	156	9	162	9
<u>Ti-8Al-1Mo-1V</u>				
1 Standard anneal	136	16	135	16
2 β processed	139	14	139	12
3 β heat treated	134	13	138	11

TABLE 12. CREEP EXPOSURE, CREEP, TENSILE, AND HOT-SALT STRESS-CORROSION DATA FOR Ti-4Al-3Mo-1V, Ti-8Al-3Mo-1V, AND Ti-8Al-1Mo-1V ALLOYS AS BETA-PROCESSED OR BETA-HEAT-TREATED AND OVERAGED

Alloy	Composition, weight percent	Heat Treatment and Processing	600 F Creep Exposure		Total Plastic Strain, percent	Room-Temperature Tensile Properties				Remarks
			Stress, ksi	Time, hr		Yield Stress, ksi	Ultimate Stress, ksi	Elongation, percent	Reduction in Area, percent	
70	Ti-4Al-3Mo-1V	Beta roll (1725 F) + 1650 F, WQ +	No exposure	—	—	115	129	16	37	Control
		16 hr, 1200 F, AC	73	97	0.171	121	132	15	43	No salt
		Ditto	74	90	0.314	121	130	13	39	No salt
		Ditto	74	75	Not gaged ^(a)	117	130	8	17	No salt cracks found
		Ditto	74	75	Not gaged ^(a)	120	130	15	33	No salt cracks found
70	Ti-4Al-3Mo-1V	Beta HT(1725 F, AC) + 1650 F, WQ +	No exposure	—	—	118	131	17	40	Control
		16 hr, 1200 F, AC	73	98	0.210	118	129	16	42	No salt
		Ditto	73	97	Not gaged	122	133	17	43	No salt
		Ditto	74	75	Not gaged ^(a)	123	133	17	42	No salt cracks found
		Ditto	74	75	Not gaged ^(a)	122	132	17	39	No salt cracks found
74	Ti-8Al-3Mo-1V	Beta roll (1910 F) + 1750 F, WQ +	No exposure	—	—	161	178	7	13	Control
		16 hr, 1200 F, AC	110	96	0.062	165	180	6	10	No salt
		Ditto	114	93	0.110	163	177	8	12	No salt
		Ditto	116	85	Not gaged ^(a)	—	154	~2	7	Many salt cracks ^(b)
		Ditto	116	85	Not gaged ^(a)	—	149	~2	4	Many salt cracks ^(b)
74	Ti-8Al-3Mo-1V	Beta HT(1860 F, AC) + 1750 F, WQ +	No exposure	—	—	156	179	9	17	Control
		16 hr, 1200 F, AC	110	95	0.052	159	172	10	18	No Salt
		Ditto	115	91	0.124	165	179	8	14	No Salt
		Ditto	116	85	Not gaged ^(a)	—	156	~2	3	Many salt cracks ^(b)
		Ditto	116	85	Not gaged ^(a)	159	159	2	6	Many salt cracks ^(b)

TABLE 12. (Continued)

Alloy	Composition, weight percent	Heat Treatment and Processing	600 F Creep Exposure		Total Plastic Strain, percent	Room-Temperature Tensile Properties				Remarks
			Stress, ksi	Time, hr.		Yield Stress, ksi	Ultimate Stress, ksi	Elongation, percent	Reduction in Area, percent	
78	Ti-8Al-1Mo-1V	Beta roll (1960 F) + 1775 F, WQ + 16 hr, 1200 F, AC	No exposure		—	139	158	14	18	Control
			90	90	0.048	139	157	13	19	No salt
		Ditto	114	91	2.820	154	158	11	20	No salt
		Ditto	95	85	Not gaged ^(a)	119	120	3	4	Few salt cracks ^(c)
		Ditto	95	85	Not gaged ^(a)	128	129	2	4	Few salt cracks ^(c)
78	Ti-8Al-1Mo-1V	Beta HT (1910 F, AC) + 1775 F, WQ + 16 hr, 1200 F, AC	No exposure		—	134	155	13	21	Control
			90	91	0.119	139	152	14	22	No salt
		Ditto	93	95	Not gaged	138	152	9	15	No salt
		Ditto	95	85	Not gaged ^(a)	137	137	3	7	Few salt cracks ^(c)
		Ditto	95	85	Not gaged ^(a)	137	141	2	8	Few salt cracks ^(c)
		Ditto	95	85	Not gaged ^(a)	136	136	2	6	Few salt cracks ^(c)

(a) Salted exposure.

(b) Damage plainly visible.

(c) Stress-corrosion damage slight.

While none of the materials is completely stable after 600 F creep, the increases in yield stresses caused by the exposures are small and in several cases, the losses in ductility are negligible.

In order to evaluate hot-salt stress-corrosion susceptibility of the three compositions, the same or higher stress levels were used in the creep exposures of salted samples as were used originally for the equiaxed alloys. Although only a few tests were run, it appears quite certain that materials with acicular microstructure are less susceptible to hot-salt stress corrosion.

Condition	After Creep							Salt Cracks
	Before Creep		Creep Stress, ksi	Yield Stress, ksi	Ultimate Stress, ksi	Elongation, percent	Reduction in Area, percent	
	Yield Stress, ksi	Elongation, percent						
<u>Ti-4Al-3Mo-1V</u>								
1 Standard anneal	114	16	73	114	121	9	16	Few
2 β processed	115	16	74	118	130	8-15	17-33	None
3 β heat treated	118	17	74	122	132	16	39	None
<u>Ti-8Al-3Mo-1V</u>								
1 Standard anneal	140	20	110	142	143	2	5	Several
2 β processed	161	7	116	--	152	~2	6	Several
3 β heat treated	156	9	116	159	159	2	6	Several
4*	164	7	116	--	128	~1	~1	Many
<u>Ti-8Al-1Mo-1V</u>								
1 Standard anneal	136	16	94	(All samples failed in the salt exposure)				
2 β processed	139	14	95	125	125	2	4	Few
3 β heat treated	134	13	95	136	138	2	7	Few

*Standard processing plus alpha-beta (1750 F) solution treating plus 24 hour, 1200 F aging.

The Ti-8Al-3Mo-1V alloy suffers from salt exposure equally in either the annealed plus stabilized (condition 1, standard anneal) or acicularized conditions, but all these conditions are less affected by hot salt than the alpha-beta-solution-treated plus aged condition (the asterisked condition in the preceding tabulation). A marginal improvement is found for acicularized Ti-4Al-3Mo-1V alloy as compared to the equiaxed condition. The properties of the acicularized Ti-8Al-1Mo-1V alloy are degraded markedly by the salt exposure but damage is less extensive than for the equiaxed condition.

Solution Treating and Aging

Specimens of Ti-4Al-3Mo-1V and Ti-8Al-3Mo-1V were solution heat treated and aged at the temperatures given in Table 13. Hardness tests were used to select heat treatments for each alloy that give comparable strengths. From Table 13 it may be seen

that aging Ti-4Al-3Mo-1V for 4 hours at 1000 F has approximately the same result as giving Ti-8Al-3Mo-1V the same treatment, or 24 hours at 1200 F. Therefore, these aging treatments were selected for comparing the tensile yield properties, fracture toughness, and aqueous stress-corrosion susceptibilities of the two alloys. In addition, comparisons were made with Ti-4Al-3Mo-1V in the solution-treated condition, and Ti-8Al-3Mo-1V in the alpha-beta-annealed-plus-stabilized condition (condition 1, standard anneal). The pertinent data for these comparisons are given in Table 14.

These experiments confirm the previous finding concerning the relationship between strength and fracture toughness. That is, higher strength levels are associated with lower toughness. Fracture toughness measured in salt water, for the purpose of determining stress-corrosion susceptibility, also decreases as the strength level increases, although alloy-content differences can produce irregularities in the relationship. Specifically, a high aluminum content results in low salt-water toughness regardless of heat treatment or strength level. Conversely, a low-aluminum alloy which is not susceptible to aqueous stress-corrosion cracking, Ti-4Al-3Mo-1V, has poor toughness in air and salt water when heat treated to a high strength level. These conclusions are illustrated by the data summary below:

Alloy	Composition, weight percent	Condition	Yield Stress, ksi	Stress Intensity, ksi $\sqrt{\text{in.}}$	
				Air	Salt Water
70	Ti-4Al-3Mo-1V	Standard anneal	114	94.9	88.2
70	Ti-4Al-3Mo-1V	1/2 hr 1650 F, WQ	120	89.3	79.4
74	Ti-8Al-3Mo-1V	Standard anneal	140	54.9	14.0
70	Ti-4Al-3Mo-1V	STA 4 hr 1000 F*	153	31.4	24.2
74	Ti-8Al-3Mo-1V	STA 4 hr 1000 F*	156	--	<15.2
74	Ti-8Al-3Mo-1V	STA 24 hr 1200 F*	164	23.6	13.8

*STA = Solution heat treated and aged as indicated.

The Ti-4Al-3Mo-1V and Ti-8Al-3Mo-1V alloys in the solution treated and aged conditions were examined for residual tensile properties after 600 F creep exposures with and without a salt coating. In general, the creep stress was adjusted upward to accommodate the higher strength of the solution-treated-plus-aged materials. The creep exposures, creep data, before and after creep tensile data, and hot-salt stress-corrosion data are given in Table 15.

Due to the small number of samples tested in this condition, observations are primarily limited to hot-salt corrosion phenomenon. Interestingly, the Ti-4Al-3Mo-1V alloy, as well as the Ti-8Al-3Mo-1V alloy, is susceptible to hot-salt cracking in the aged condition. The degradation by salt cracking is less pronounced in the lower strength solution-treated condition although a few cracks were observed. As expected, the creep exposure per se results in the aging of the Ti-4Al-3Mo-1V alloy, causing an increase in strength and a decrease in ductility.

Ti₃Al Stabilization Treatments

In order to promote the formation of the ordered Ti₃Al (α_2) phase, selected Ti-4Al- and Ti-8Al-base alloys were given the standard anneal, then aged 24 hours at 1112 F

TABLE 13. HARDNESS VALUES FOR HEAT-TREATED Ti-4Al-3Mo-1V
AND Ti-8Al-3Mo-1V ALLOYS

Heat Treatment(a)	Vickers Hardness No., 10-kg load	
	Ti-4Al-3Mo-1V	Ti-8Al-3Mo-1V
Alpha-beta annealed and stabilized at 1200 F	263	323
Alpha-beta annealed and stabilized, then alpha-beta solution heat treated	314	360
Alpha-beta annealed and stabilized, then alpha-beta solution heat treated, plus aged		
1 hr at 900 F	366	--
4 hr at 900 F	391	--
1 hr at 925 F	383	414
4 hr at 925 F	395	410
16 hr at 925 F	400	446
1 hr at 1000 F	376	445
4 hr at 1000 F	404	411
16 hr at 1000 F	388	422
1 hr at 1100 F	391	420
4 hr at 1100 F	376	447
16 hr at 1100 F	360	417
16 hr at 1200 F	338	398
24 hr at 1200 F	322	406
Alpha-beta annealed and stabilized, beta annealed, then alpha-beta solution heat treated and aged 16 hr at 1200 F	314	411
Beta fabricated, alpha-beta solution heat treated, and aged 16 hr at 1200 F	297	405

(a) Heat treatment and processing temperatures were as follows:

	Ti-4Al-3Mo-1V	Ti-8Al-3Mo-1V
Alpha-beta anneal (FC)	1650 F	1750 F
Alpha-beta solution heat treatment (WQ)	1650 F	1750 F
Beta anneal (AC)	1725 F	1860 F
Beta fabrication	1775 F	1910 F

TABLE 14. ROOM-TEMPERATURE TENSILE AND AQUEOUS STRESS-CORROSION DATA FOR SOLUTION-TREATED AND AGED ALLOYS^(a)

Alloy	Composition, weight percent	Heat Treatments ^(b) (As indicated after standard alpha-beta annealing and stabilization)	Fracture Toughness		Room-Temperature Tensile					
			Environment ^(c)	Loading Method ^(d)	Stress Intensity for Failure, ksi√in.	Total Exposure Time, min.	0.2 Percent Offset Yield Stress, ksi	Ultimate Stress, ksi	Elongation in 1 Inch, percent	Reduction in Area, percent
70	Ti-4 Al-3 Mo-IV	(1/2)1650F, WQ+(4)1000F, AC Vhn = 404	Air	Step	31.4	4	153	177	10	23
			Salt water	Step	26.5	27	153	176	11	26
			Salt water	C	25.2	1				
			Salt water	C	23.3 ^(e)	360 ^(e)				
			Salt water	C	24.25	--	153	176	10	24
74	Ti-8 Al-3 Mo-IV	(1/2)1750F, WQ+(4)1000F, AC Vhn = 411	Air	Step	-- ^(f)	--	159	200	8	14
			Salt water	Step	15.2	14	153	198	7	11
			Salt water	C	-- ^(f)	--				
			Salt water	C	<15.2	--	156	199	7	12
			Salt water	C	13.75	--	164	180	7	10
74	Ti-8 Al-3 Mo-IV	(1/2)1750F, WQ+(24)1200F, AC Vhn = 406	Air	Step	23.6	1				
			Salt water	Step	16.0	10	164	180	7	10
			Salt water	C	14.4	2				
			Salt water	C	13.1 ^(e)	360 ^(e)				
			Salt water	C	13.75	--	164	180	7	10
70	Ti-4 Al-3 Mo-IV	(1/2)1650F, WQ No aging Vhn = 314	Air	Step	89.3	40	120	144	18	40
			Salt water	Step	80.5	31				
			Salt water	C	80.1	275				
			Salt water	C	78.6 ^(e)	360 ^(e)				
			Salt water	C	79.35	--	120	144	18	40
74	Ti-8 Al-3 Mo-IV	None (except standard annealing) Vhn = 323	Air	step	54.9	101				
			Salt water	step	13.3	17				
			Salt water	C	15.6	3				
			Salt water	C	12.5 ^(e)	360 ^(e)				
			Salt water	C	14.05	--	140	158	20	24
70	Ti-4 Al-3Mo-IV	None (except standard annealing)(critical values)	Salt water	C	88.25	--	114	119	16	46

(a) 1/8-inch thick, transverse samples.

(b) Numbers in parentheses are hours exposure. WQ = water quench, AC = air cool.

(c) SW = 3.5% NaCl solution.

(d) C = Constant load tests.

(e) No failure in 360 minutes. Test discontinued.

(f) Two out of three samples failed catastrophically in fatigue cracking operation. Number of cycles for crack initiation was normal, but, once crack started, crack propagated catastrophically.

TABLE 15. CREEP EXPOSURE, CREEP, TENSILE, AND HOT-SALT STRESS-CORROSION DATA FOR Ti-4Al-3Mo-1V AND Ti-8Al-3Mo-1V ALLOYS IN THE SOLUTION-TREATED-AND-AGED CONDITIONS

Alloy	Composition, weight percent	Heat Treatment	600 F Creep Exposure		Total Plastic Strain, percent	Room-Temperature Tensile Properties				Remarks
			Stress, ksi	Time, hr		Yield Stress, ksi	Ultimate Stress, ksi	Elongation, percent	Reduction in Area, percent	
70	Ti-4Al-3Mo-1V	Std. + 1650 F, WQ (No aging)	No exposure		--	120	144	18	40	Control
		Std. + 1650 F, WQ (No aging)	74	75	Not gaged ^(a)	148	159	10	37	3 hot salt cracks
		Std. + 1650 F, WQ (No aging)	73	94	0.133	150	164	9	34	No salt
70	Ti-4Al-3Mo-1V	Std. + 1650 F, WQ + 4 hr, 1000 F, AC	No exposure		--	153	176	10	24	Control
		Std. + 1650 F, WQ + 4 hr, 1000 F, AC	85	75	Not gaged ^(a)	--	137	~ 2	~ 3	Many salt cracks ^(b)
74	Ti-8Al-3Mo-1V	Std. + 1750 F, WQ + 4 hr, 1000 F, AC	No exposure		--	156	199	7	12	Control
		Std. + 1750 F, WQ + 4 hr, 1000 F, AC	116	85	Not gaged ^(a)	--	117	~ 1	~ 3	Many salt cracks ^(b)
74	Ti-8Al-3Mo-1V	Std. + 1750 F, WQ + 24 hr, 1200 F, AC	No exposure		--	164	180	7	10	Control
		Std. + 1750 F, WQ + 24 hr, 1200 F, A AC	116	85	Not gaged ^(a)	--	128	~ 1	~ 1	Many salt cracks ^(b)

(a) Salted exposure.

(b) Damage plainly visible.

plus 24 hours at 1022 F. A preliminary experiment had shown that this treatment lowers the salt-water fracture toughness in Ti-8Al-1Mo-1V⁽¹⁾. The current experiment was designed to confirm this result as well as to characterize the stabilized material for tensile and toughness properties. Table 16 gives the results of this series of tests.

The effect of the ordering treatment is very marked. The air and salt-water fracture toughnesses of the Ti-8Al-base alloys are drastically reduced by the increased presence of Ti₃Al, whereas the yield stress is only marginally increased. Conversely the fracture-toughness parameters of the Ti-4Al-base alloys are slightly increased by the ordering heat treatment. This is consistent with the Ti-Al phase diagram proposed by Blackburn⁽²⁾ which shows that Ti-8Al is within the $\alpha + \alpha_2$, 2-phase region at 1100 F, whereas Ti-4Al is in the single-phase α region. It is significant that the sharp reduction in fracture toughness exhibited by the Ti-8Al-base alloys is not accompanied by a large increase in yield stress. Apparently, increasing the amount of Ti₃Al does not affect the yielding behavior, but does make crack propagation easier. A possible explanation of this behavior is that the α_2 particles fracture under the stress of coplanar dislocation pile-ups and nucleate cleavage microcracks.

In each part of the testing program reported here, groups of alloys with constant aluminum content and variable beta-stabilizer content have shown an inverse relationship between yield strength and fracture toughness in air or salt water. This trend is also evident for alloys given the Ti₃Al stabilization treatment as shown in the following summary of the data:

Alloy	Composition, weight percent	Condition	Yield Stress, ksi	Stress Intensity, ksi $\sqrt{\text{in.}}$	
				Air	Salt Water
70	Ti-4Al-3Mo-1V	Std. anneal	114	94.9	88.2
		α_2 exposure	114	99.4	91.4
72	Ti-4Al-1.5Mo-0.5V	Std. anneal	102	91.7	83.4
		α_2 exposure	104	97.6	94.7
73	Ti-8Al	Std. anneal	100	96.5	30.7
		α_2 exposure	105	41.6	20.5
75	Ti-8Al-1Mo	Std. anneal	119	68.7	28.0
		α_2 exposure	126	28.3	19.3
78	Ti-8Al-1Mo-1V	Std. anneal	136	64.4	24.0
		α_2 exposure	140	32.6	15.1
74	Ti-8Al-3Mo-1V	Std. anneal	140	54.9	14.0
		α_2 exposure	Br.	24.2	13.8

The effect of beta-stabilizer content on the strength and toughness of alpha-beta alloys must be considered together with the result that ordering produces a drastic decrease in toughness, but little change in strength. It is suggested that much of the strengthening effect of the beta-stabilizer additions is due to the fact that for a constant

TABLE 16. ROOM-TEMPERATURE TENSILE AND AQUEOUS STRESS-CORROSION DATA FOR
1112 F PLUS 1022 F STABILIZED ALLOYS^(a)

Alloy	Composition, weight percent	Environment	Fracture Toughness		Room-Temperature Tensile				
			Loading Method ^(d)	Stress Intensity for Failure, ksi√in.	Total Exposure Time, min	0.2 Percent Offset Yield Stress, ksi	Ultimate Stress, ksi	Elongation in 1 Inch, percent	Reduction in Area, percent
70	Ti-4 Al-3 Mo-IV	Air	Step	99.4	160	115	117	17	30
		Salt water	Step	98.9	167	114	121	17	28
		Salt water	C	92.8	37				
		Salt water	C	89.9 ^(e)	360 ^(e)				
		Critical or average values ^(b)	C	91.35	--	114	119	17	29
		Critical or average values ^(c)	C	88.25	--	114	119	16	46
72	Ti-4 Al-1.5 Mo-0.5V	Air	Step	97.6	107	104	111	23	42
		Salt water	Step	98.4	116	103	110	18	44
		Salt water	C	96.7	2				
		Salt water	C	92.7 ^(e)	360 ^(e)				
		Critical or average values ^(b)	C	94.7	--	104	110	20	43
		Critical or average values ^(c)	C	83.4	--	102	108	20	36
73	Ti-8 Al	Air	Step	41.6	78	105	112	21	27
		Salt water	Step	21.2	37	106 ^(f)	106 ^(f)	6 ^(f)	12 ^(f)
		Salt water	C	21.1	3				
		Salt water	C	19.9 ^(e)	360 ^(e)				
		Critical or average values ^(b)	C	20.5	--	105	112	21	27
		Critical or average values ^(c)	C	30.7	--	100	101	26	36
75	Ti-8 Al-1 Mo	Air	Step	28.3	43	126	128	5	8
		Salt water	Step	19.5	36	-- ^(g)	131	3	10
		Salt water	C	19.5	5				
		Salt water	C	19.1 ^(e)	360 ^(e)				
		Critical or average values ^(b)	C	19.3	--	126	128	5	8
		Critical or average values ^(c)	C	28.0	--	119	124	20	30

TABLE 16. (Continued)

		Fracture Toughness				Room-Temperature Tensile			
				Stress Intensity for Failure, ksi√in.	Total Exposure Time, min	0.2 Percent Offset Yield Stress, ksi	Ultimate Stress, ksi	Elongation in 1 Inch, percent	Reduction in Area, percent
Alloy	Composition, weight percent	Environment	Loading Method(d)						
78	8 Al-1 Mo-IV	Air	Step	32.6	45	141	145	4	8
		Salt water	Step	17.1	12	138	141	5	9
		Salt water	C	16.1	3				
		Salt water	C	14.1 (e)	360 (e)				
Critical or average values (b)		Salt water	C	15.1	--	140	143	4	8
Critical or average values (c)		Salt water	C	24.0	--	136	149	16	21
74	Ti-8 Al-3 Mo-1V	Air	Step	24.2	6	-- (g)	146	2	4
		Salt water	Step	14.4	16	-- (g)	132	1	4
		Salt water	C	14.0	2				
		Salt water	C	13.6 (e)	360 (e)				
Critical or average values (b)		Salt water	C	13.8	--	--	139	2	4
Critical or average values (c)		Salt water	C	14.05	--	140	158	20	24

(a) 1/8-inch thick, transverse samples.

(b) Values obtained after standard annealing plus 24 hours at 1112 F plus 24 hours at 1022 F.

(c) Values obtained after standard annealing (prior data).

(d) C = constant load tests.

(e) No failure in 360 minutes. Test discontinued.

(f) Defective sample.

(g) Brittle failure.

total aluminum content the aluminum concentration of the α phase increases with increasing volume fraction of beta phase. In this way beta-stabilizer additions could increase the amount of Ti_3Al in the α phase, and it has been shown that this condition is related to low fracture toughness in air and salt water.

MECHANISMS OF STRESS-CORROSION CRACKING

Aqueous Environments

The mechanism of aqueous stress-corrosion cracking outlined in the previous report⁽¹⁾ assumes that the critical process is the precipitation of strain-induced hydrides in the active $\{10\bar{1}0\}$ slip planes. The hydrides reduce plastic flow in the vicinity of the crack tip by blocking the slip planes and cause cleavage of the α phase. The environment may also act to reduce the cleavage strength of the α phase by adsorption of some surface-active species.

During the past year a series of specialized experiments has been performed to test the hypotheses in this mechanism. Most of the experiments were designed with the hydride mechanism in mind. For example, the kinetics of hydrogen absorption were studied as a function of composition and heat treatment, the mechanism of hydride nucleation in slip bands was investigated further by transmission electron microscopy, and the effects of dissolved hydrogen and hydrides on the mechanical properties of Ti-8Al-1Mo-1V were determined. However, some general stress-corrosion experiments were performed which do not involve any prior assumptions about mechanism. These experiments provide factual details about the stress-corrosion behavior of Ti-8Al-1Mo-1V which are consistent with the proposed hydride mechanism, but which can also be interpreted in other ways. It is believed that the parameter which most clearly defines an alloy's susceptibility to stress-corrosion cracking is the rate of subcritical crack growth ("slow" crack growth). Accordingly, crack growth rates in Ti-8Al-1Mo-1V were measured as a function of stress intensity, temperature, and concentration of chloride ions in the environment. Also complete stress-strain curves for this alloy were determined for various specimen thicknesses, strain rates, and environments.

These experiments are described below, starting with the most general and proceeding to the ones that were intended to investigate a specific effect or mechanism. All of the results are considered together in the discussion section.

Crack Velocity Measurements

A test stand for single-edge-notched cantilever specimens was modified to enable continuous measurements of crack length to be made during subcritical crack growth. A transducer was mounted on the lever arm of the test stand and connected via a linear variable differential transformer to a pen recorder. Thus a continuous record of lever arm deflection was obtained, and this could be converted to crack length by calibrating the apparatus.

The specimen material was commercial Ti-8Al-1Mo-1V, having the following analysis (weight percent): 7.9Al, 1.0Mo, 1.0V, 0.06Fe, 0.02C, 0.088 O, 0.0078 H. This material was hot rolled to 0.24-inch-thick plate and annealed as follows:

1/2 hour at 1778 F, furnace cool to 1200 F,
1/2 hour at 1200 F, air cool, and
3 hours at 1200 F in vacuum (5×10^{-5} torr).

Transverse specimens 8 inches long and 2 inches wide were cut from this material and precracked in the usual way.

The apparatus was calibrated by placing a specimen containing a precrack (saw cut and fatigue crack) of known length in position and zeroing the recorder. The specimen was then loaded in air and the LVDT reading was recorded for each load. The specimen was loaded and unloaded several times to verify that the relationship between LVDT reading and load is single-valued for a constant crack length. Next a bottle of salt water was placed around the crack, a load was applied and the crack was allowed to grow approximately 0.1 inch in length. The salt water was then removed, the specimen washed and dried, and the LVDT-load relationship determined for the new crack length. This procedure was repeated until a family of curves was generated representing the relationship between LVDT reading and load for various crack lengths ranging from 0.30 inch to 1.3 inch (Figure 6).

The actual tests were carried out by loading the specimen incrementally until subcritical crack growth began. The crack was then allowed to propagate at constant load until final fracture occurred. A calibration curve for each test was constructed by drawing a vertical line on the calibration chart (Figure 6) corresponding to the load used during crack propagation, and reading off the LVDT reading as a function of crack length. The LVDT readings which were recorded during the test could then be converted to crack lengths, and the crack velocities calculated from plots of crack length against time. For each test, two checks were made on the accuracy of the calibration curve. The crack lengths before and after the test were measured accurately, and the LVDT reading given by the calibration curve was compared with the actual readings. In most cases these comparisons showed good agreement (within 10 percent).

In the single-edge-notched cantilever test the stress intensity at the crack tip, K_I , increases continuously as the crack propagates. Thus the relationship between crack velocity and stress intensity can be determined from a single test. All of the results are presented as plots of crack velocity, \dot{a} , against K_I . The 0.24-inch thick specimens were thick enough to ensure that the conditions for plain strain fracture were satisfied during subcritical cracking. Furthermore, the stress-corrosion fractures were all "flat" with no evidence of shear lips. Therefore, the stress intensities reported for subcritical cracking are valid plain-strain values.

The results for the tests performed under standard conditions (room temperature, 3.5 percent NaCl solution) are given in Figure 7. Data from two independent tests are given to show that the reproducibility is excellent. The most striking feature of the $\dot{a} - K_I$ curve is the rapid decrease in the dependence of crack velocity on stress intensity as the crack propagates. Extrapolation of the curve past the value of K_I at which final fracture occurs suggests that \dot{a} approaches a limiting velocity of 6.2×10^{-3} inches per second, which is independent of K_I . It can be shown that this limiting velocity is a function of the material and environment only by conducting a test at a load much larger than

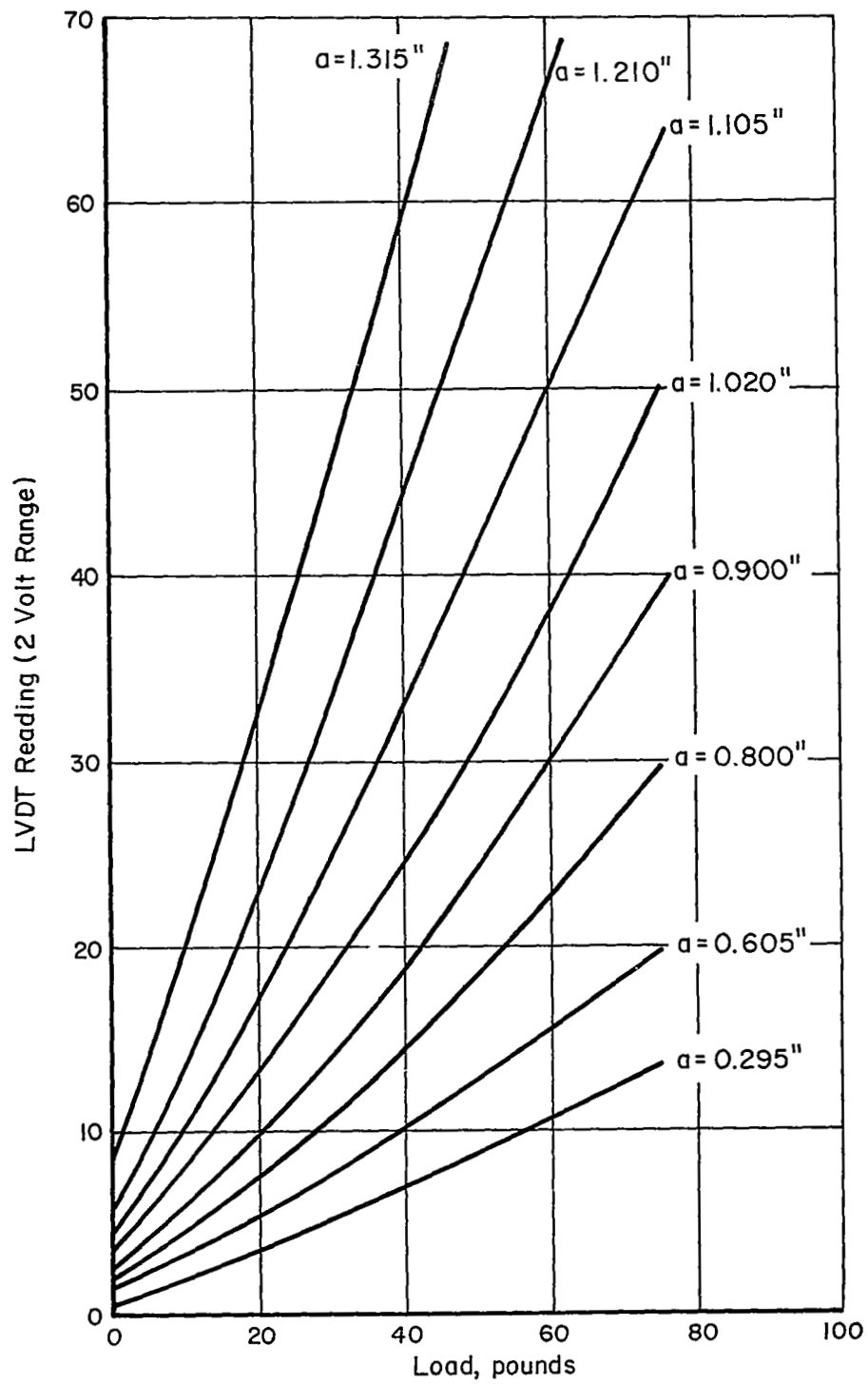


FIGURE 6. CALIBRATION CHART FOR CRACK VELOCITY MEASUREMENTS

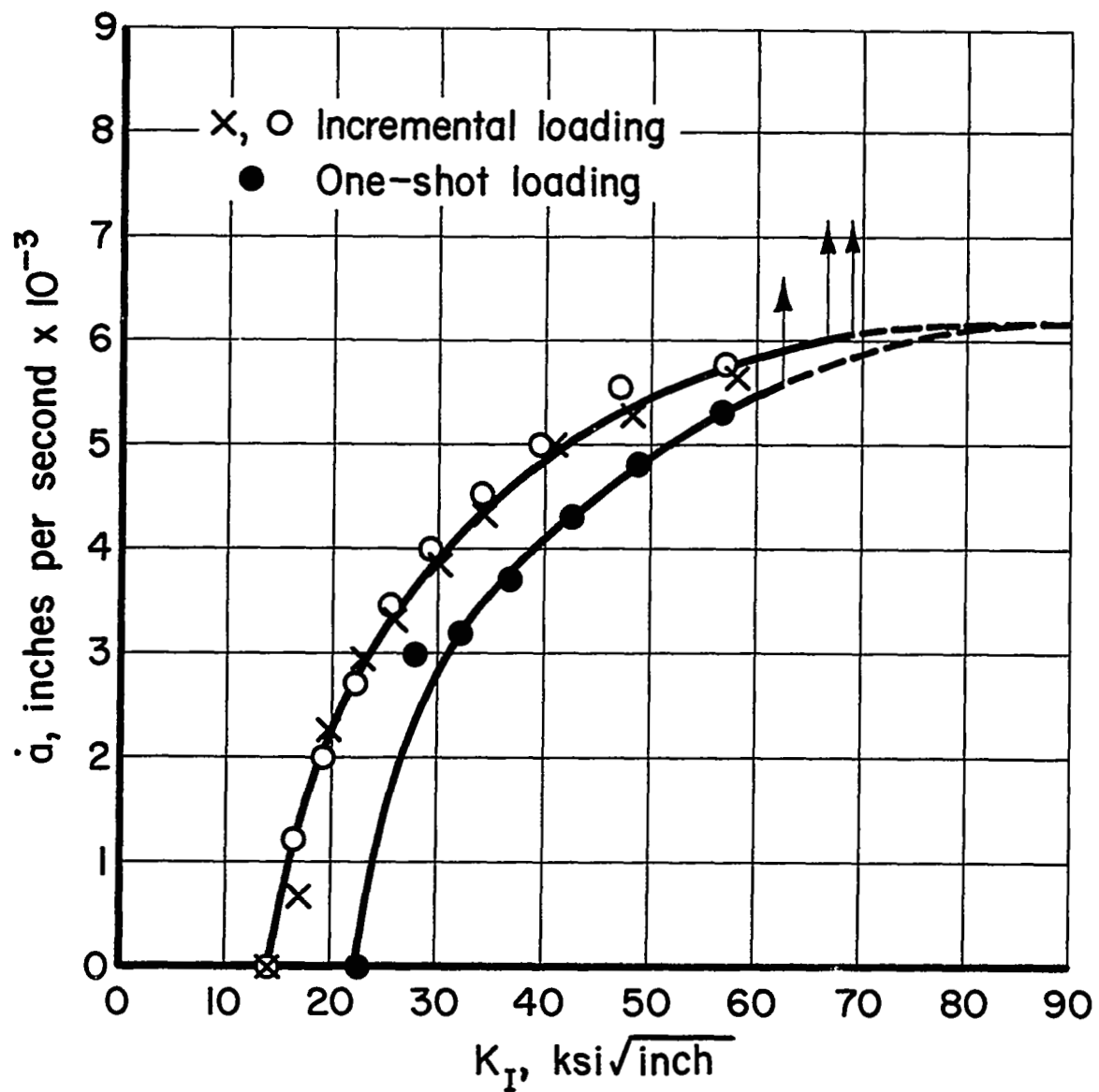


FIGURE 7. SUBCRITICAL-CRACK-GROWTH RATES FOR
Ti-8Al-1Mo-1V, IN 3.5 PERCENT NaCl, AT R.T.

that required to initiate subcritical cracking. The results of such a test are also given in Figure 7. In this case the specimen was overloaded by a single load application which produced a higher K_I and $\partial \dot{a} / \partial K_I$ at the onset of cracking than with the standard incremental loading. However, \dot{a} approaches the same limiting velocity in both cases.

The dependencies of crack velocity on the environmental temperature and chloride-ion concentration have been investigated. The results of these tests are illustrated in Figures 8 and 9. The following observations are made:

- (1) All of the $\dot{a} - K_I$ curves show a continuously decreasing dependence of \dot{a} on K_I . This effect is most pronounced at the higher temperatures and lower chloride-ion concentrations where the crack velocity becomes independent of K_I before final fracture occurs.
- (2) The critical stress intensity for initiation of subcritical cracking, K_{ISCC} , varies inversely with the chloride-ion concentration, but does not show any significant temperature dependence.
- (3) The stress intensity at which final rapid fracture occurs, K_C , is 59-69 ksi $\sqrt{\text{in.}}$.

The limiting crack velocity, \dot{a}^* , is taken to be the most precise parameter for comparing the stress corrosion behavior of various alloys and/or environments. In the present study the alloy composition and heat treatment were kept constant and some environmental variables were changed. The results are summarized in Table 17. Where necessary, \dot{a}^* was determined by extrapolating the $\dot{a} - K_I$ curve past K_C . By plotting $\log \dot{a}^*$ against $1/T$ (Figure 10) the temperature dependence of \dot{a}^* for 3.5 percent NaCl is found to be

$$\dot{a}^* = 1.2 \exp(-3200/RT) \quad (1)$$

TABLE 17. SUMMARY OF SUBCRITICAL CRACK-VELOCITY STUDIES

Temperature, K	X_{Cl^-} , ppm	K_{ISCC} , ksi $\sqrt{\text{in.}}$	K_C , ksi $\sqrt{\text{in.}}$	\dot{a}^* , in./s
272	21,000(a)	17.7	65.4	3.3×10^{-3}
295	21,000	14.0	67.4	6.2×10^{-3}
333	21,000	14.7	62.1	9.5×10^{-3}
366	21,000	18.4	66.3	15.9×10^{-3}
295	0.1(b)	24.2	59.5	0.90×10^{-3}
295	100	20.8	58.7	2.4×10^{-3}
295	6,000	18.4	60.3	4.8×10^{-3}
295	21,000	14.0	67.4	6.2×10^{-3}

(a) 3.5 weight percent NaCl.

(b) Doubly distilled, de-ionized water.

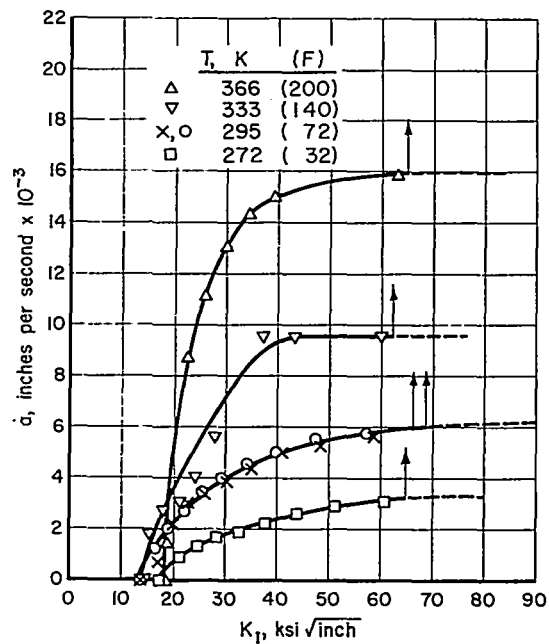


FIGURE 8. SUBCRITICAL-CRACK-GROWTH RATES FOR Ti-8Al-1Mo-1V IN 3.5 PERCENT NaCl AT VARIOUS TEMPERATURES

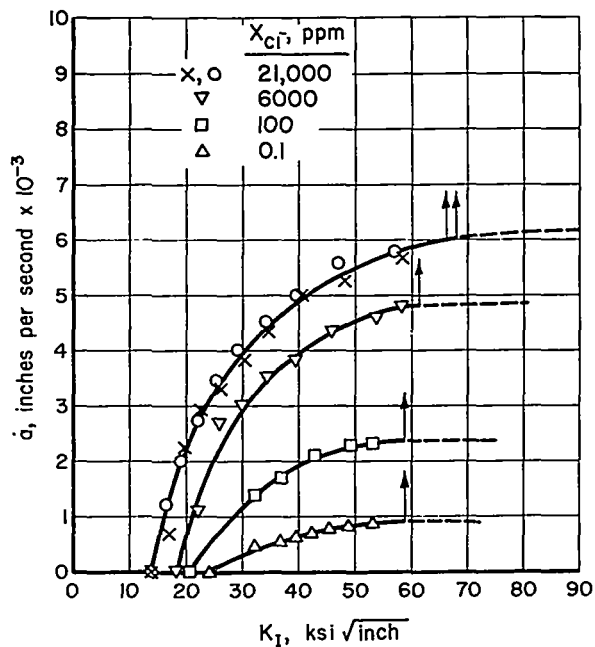


FIGURE 9. SUBCRITICAL-CRACK-GROWTH RATES FOR Ti-8Al-1Mo-1V IN SALT WATER AT ROOM TEMPERATURE AS A FUNCTION OF CHLORIDE ION CONCENTRATION, X_{Cl^-}

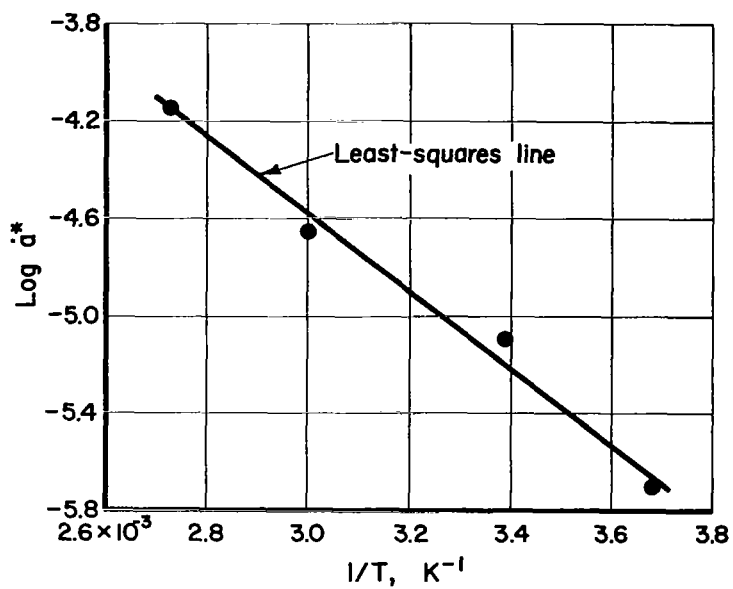


FIGURE 10. TEMPERATURE DEPENDENCE OF SUBCRITICAL CRACK VELOCITY FOR Ti-8Al-1Mo-1V IN 3.5 PERCENT NaCl

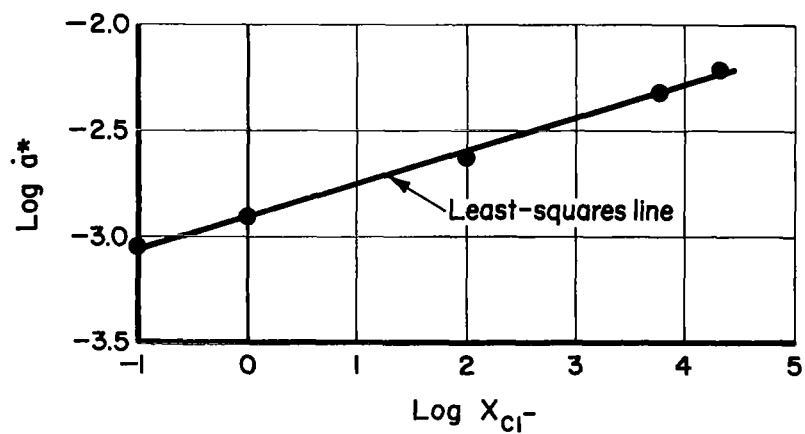


FIGURE 11. CONCENTRATION DEPENDENCE OF SUBCRITICAL CRACK VELOCITY FOR Ti-8Al-1Mo-1V AT ROOM TEMPERATURE

The relationship between \dot{a}^* and chloride-ion concentration, X_{Cl^-} , is revealed by plotting $\log \dot{a}^*$ against $\log X_{Cl^-}$ (Figure 11). The functional relationship for $T = 295$ K is found to be

$$\dot{a}^* = 1.2 \times 10^{-3} (X_{Cl^-})^{0.16} \quad (2)$$

Effect of Specimen Thickness and Strain Rate
on Yielding and Fracture of Ti-8Al-1Mo-1V
in Air and Salt Water

The effect of environment on the yielding behavior of Ti-8Al-1Mo-1V was investigated by performing tensile tests in air and salt water. Specimens having the geometry shown in Figure 12 were prepared from the same annealed material that was used for the crack-velocity measurements. Four different specimen thicknesses were used; in order to ensure that all specimens had the same microstructure, the desired thicknesses were obtained by machining and surface grinding. One specimen of each thickness was deformed to fracture in air, and in 3.5 percent NaCl solution at strain rates of .005 and 2.0 minute^{-1} . The 0.2 percent offset yield stress and the percent reduction in area for each specimen are listed in Table 18. The complete stress-strain curves for the thickest and thinnest specimens are given in Figure 13. The following conclusions are drawn from these results:

TABLE 18. TENSILE DATA FOR ANNEALED Ti-8Al-1Mo-1V AS A FUNCTION OF SPECIMEN THICKNESS

Specimen	Thickness, inch	$\dot{\epsilon}$, per min.	Environment	Yield Stress, ksi	Reduction in Area, percent
1A	.020	.005	Air	139	14.8
2A	.020	2.0	Air	147	16.2
3A	.020	.005	NaCl	147	14.8
4A	.020	2.0	NaCl	155	16.2
1B	.050	.005	Air	130	23.0
2B	.050	2.0	Air	140	26.4
3B	.050	.005	NaCl	139	12.1
4B	.050	2.0	NaCl	144	12.1
1C	.100	.005	Air	141	10.7
2C	.100	2.0	Air	135	32.3
3C	.100	.005	NaCl	134	15.5
4C	.100	2.0	NaCl	141	36.4
1D	.220	.005	Air	119	13.1
2D	.220	2.0	Air	150	35.1
3D	.220	.005	NaCl	124	8.7
4D	.220	2.0	NaCl	130	13.1

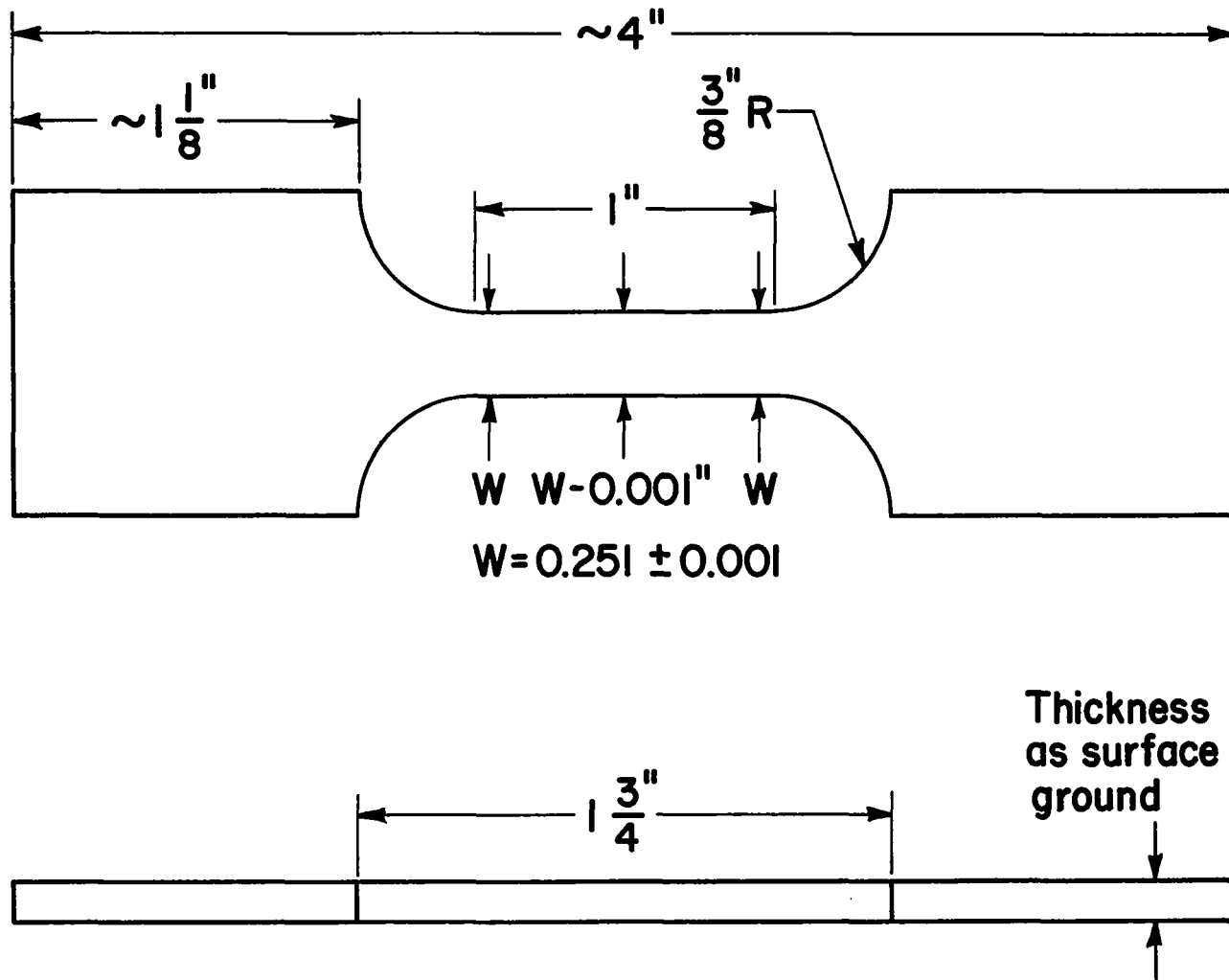


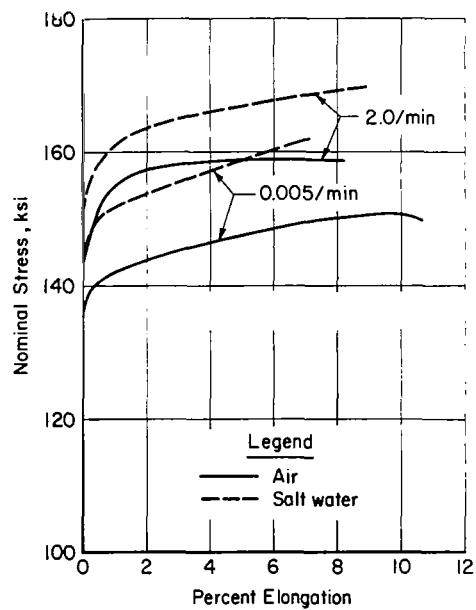
FIGURE 12. DETAILS OF TENSILE SPECIMEN

- (1) The yield stress varies inversely with specimen thickness for both strain rates and both environments (Figure 14). This effect is probably an artifact produced by the machining and surface grinding. Some tensile tests described later (Table 20 and Figure 24) indicate that the yield stress of 0.20-inch-thick specimens of Ti-8Al-1Mo-1V in air is much less than reported here.
- (2) The yield stress and initial rate of work hardening are higher in salt water than in air at comparable strain rates. This effect is most pronounced in the thinnest specimens.
- (3) The reduction in area is larger at the higher strain rate for all specimen thicknesses and in both environments.
- (4) For comparable strain rates the reduction in area is significantly less in salt water than in air only for the thickest specimen (0.220 inch). The reduction in area is not very sensitive to environment for specimens thinner than this.

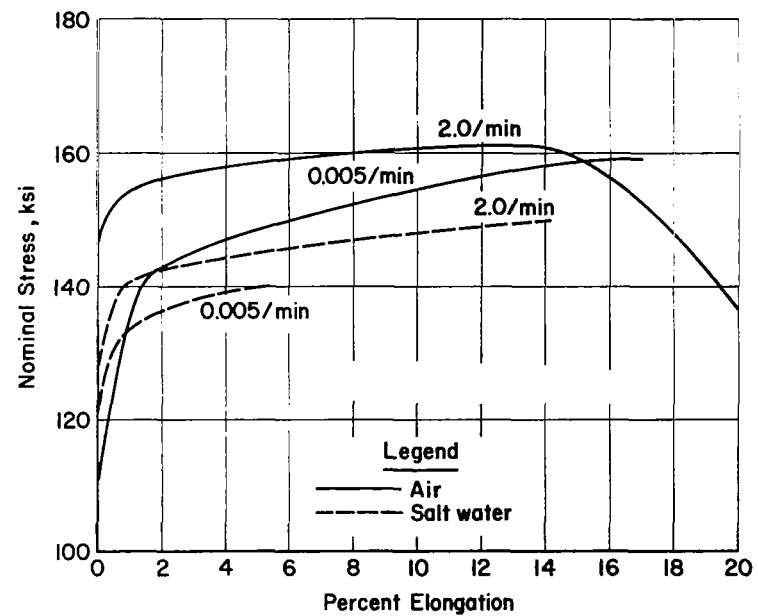
Kinetics of Hydrogen Absorption

It was reported previously⁽¹⁾ that for titanium-aluminum alloys near the stoichiometric composition, Ti-25 atomic percent Al, the rate of ingress of hydrogen into an alloy increases with increasing degree of long-range order (Figure 15). This could be another contribution to the strong correlation between the volume fraction of ordered Ti₃Al phase and an alloy's susceptibility to aqueous stress-corrosion cracking. It also accounts for the observation that hydrides form more readily in high-aluminum alloys than in pure titanium when exposed to acidic solutions.⁽³⁾ Thus an alloy's susceptibility to aqueous stress-corrosion cracking could be determined partially by the rate at which it can absorb hydrogen from the environment. Accordingly, the kinetics of hydrogen absorption were determined for several titanium alloys representing various aluminum contents.

Specimens of three different alloys in the form of 2.0 by 0.75 by 0.015 inch strips were given the standard α/β anneal-plus-stabilization treatment to produce an equiaxed microstructure (Table 19). One specimen of Ti-8Al was quenched from the annealing temperature to minimize the amount of Ti₃Al. The hydrogen-charging technique was the same as that described previously^(1,4). The specimens were rapidly heated to the charging temperature by sliding a preheated furnace over the reaction chamber. In each case hydrogen first began to enter the specimen when the temperature reached 1200 F. Apparently this represents the minimum temperature at which titanium alloys will absorb hydrogen under low pressure (~0.3 atmosphere). All tests were performed at this temperature. Special care was taken to ensure that the specimens were shiny and visibly free from tarnish following hydrogen charging at 1200 F. The results are given in Figure 16.



a. 0.020-Inch-Thick Specimens



b. 0.220-Inch-Thick Specimens

FIGURE 13. NOMINAL STRESS-ELONGATION CURVES FOR Ti-8Al-1Mo-1V IN AIR AND SALT WATER AT TWO DIFFERENT STRAIN RATES

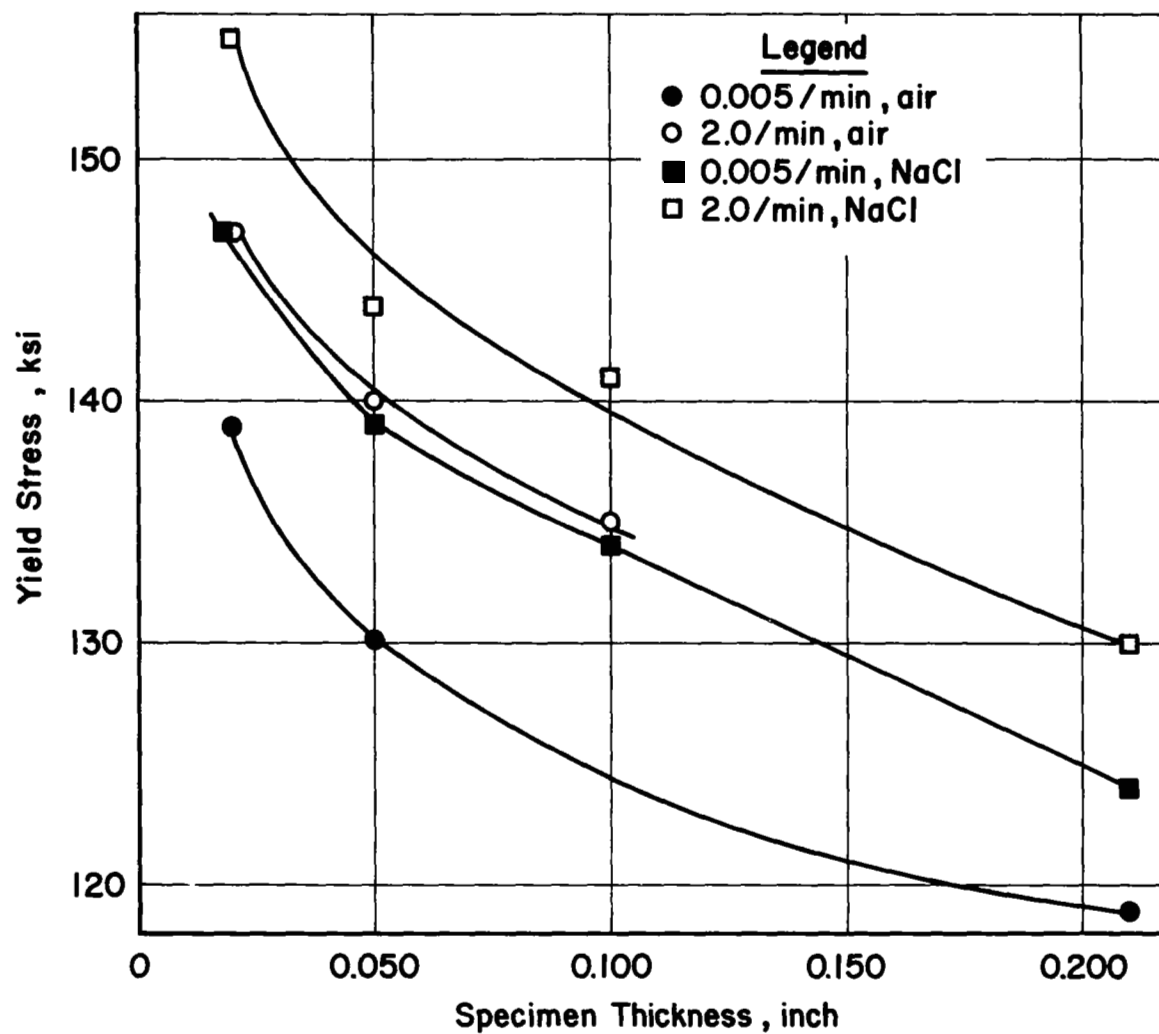


FIGURE 14. VARIATION IN YIELD STRESS WITH SPECIMEN THICKNESS FOR Ti-8Al-1Mo-1V AS A FUNCTION OF STRAIN RATE AND TEMPERATURE

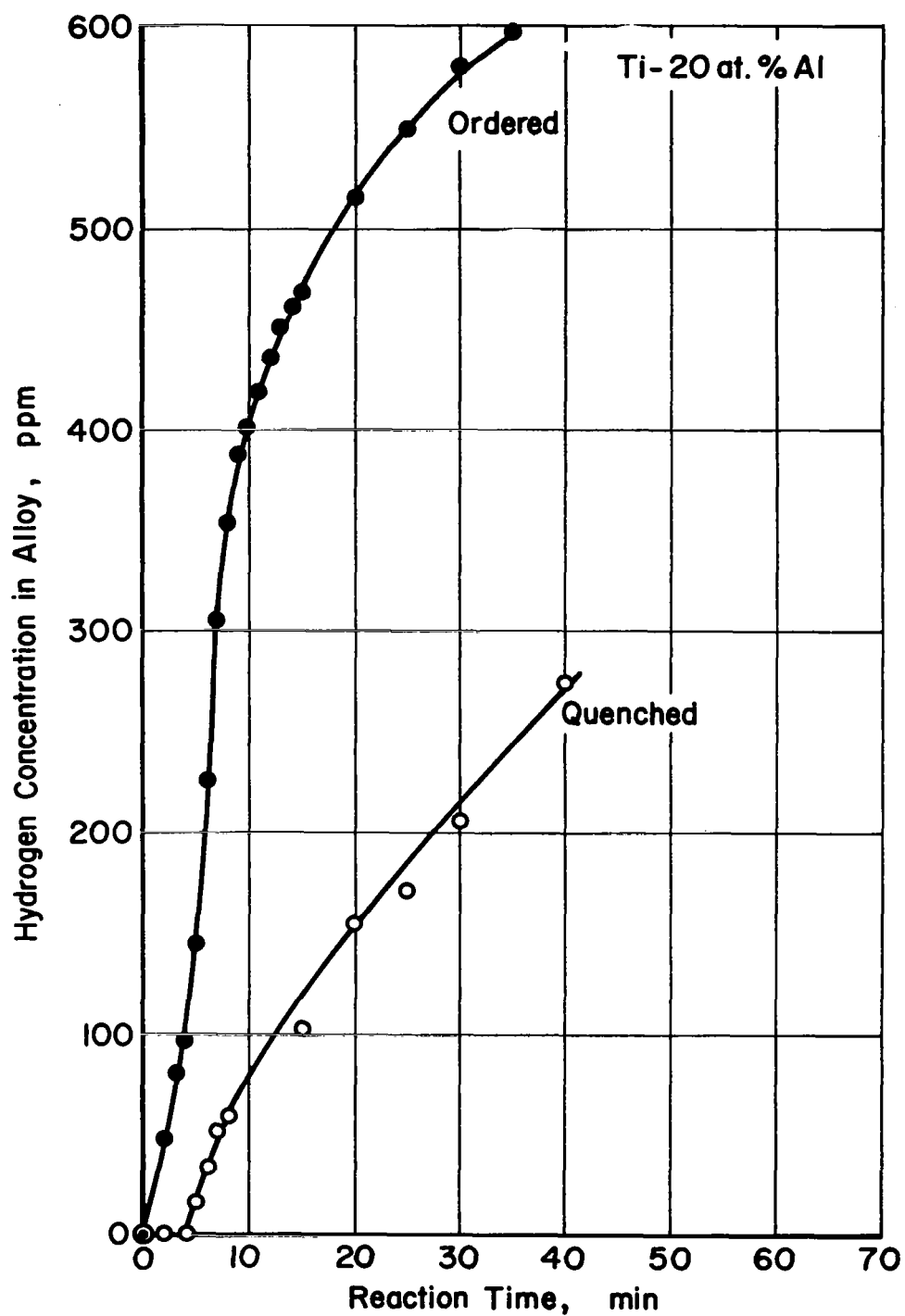


FIGURE 15. HYDROGEN ABSORPTION RATES FOR Ti-20 ATOMIC PERCENT ALUMINUM AT 1200 F SHOWING THE EFFECT OF ORDERING

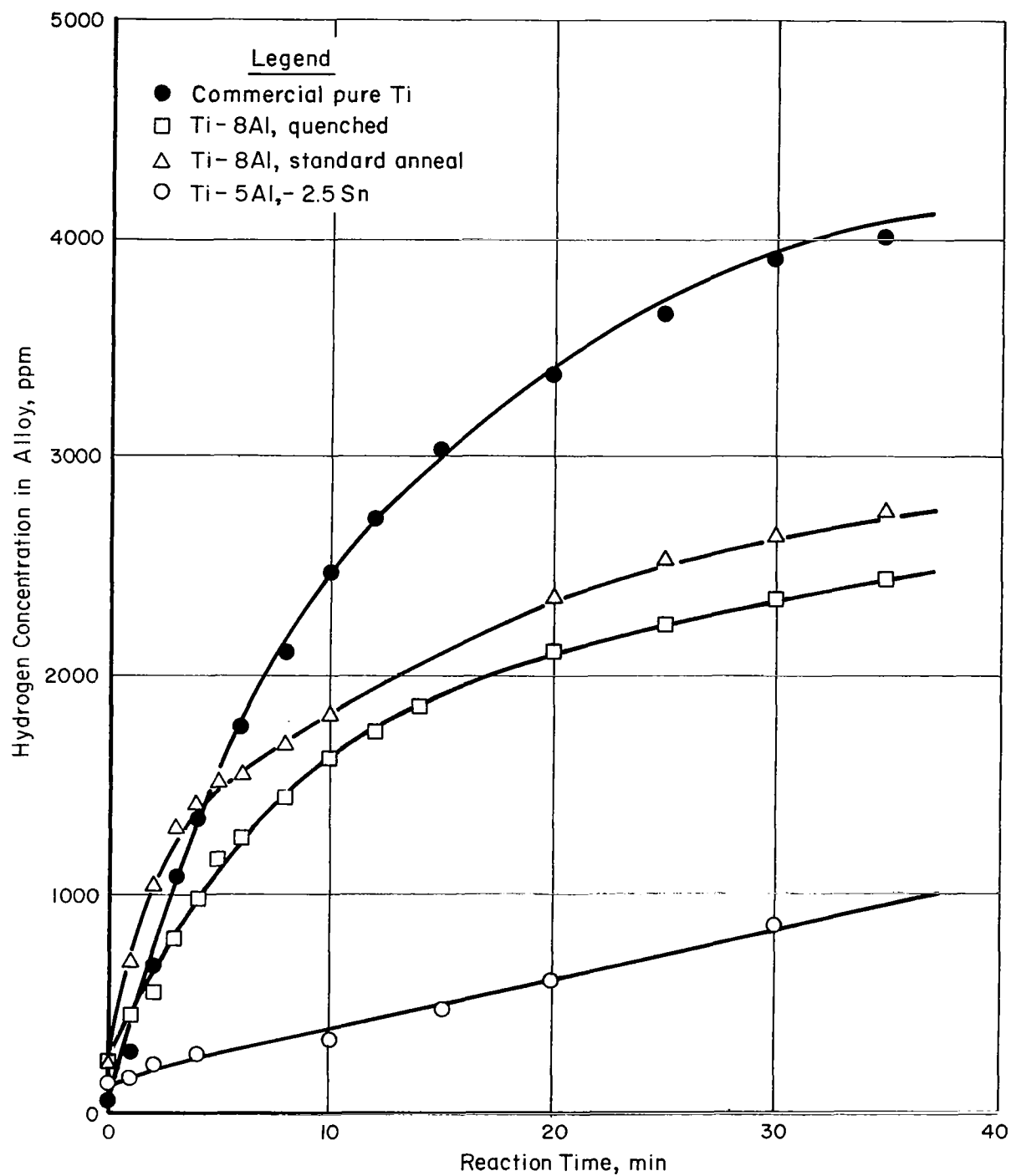


FIGURE 16. HYDROGEN ABSORPTION RATES AT 1200 F

TABLE 19. HEAT TREATMENT OF ALLOYS FOR
HYDROGEN-CHARGING EXPERIMENTS

Composition, weight percent	Annealing Treatment
Commercial Pure Ti	1 hr at 1470 F, furnace cool to 1200 F 6 hr at 1200 F, air cool
Ti-8Al	1 hr at 1650 F, furnace cool to 1200 F 6 hr at 1200 F, air cool
Ti-8Al	1 hr at 1650 F, air cool
Ti-5Al-2.5Sn	1 hr at 1650 F, furnace cool to 1200 F 6 hr at 1200 F, air cool

Clearly there are significant differences in the hydrogen absorption rates for the three alloys investigated. The commercial-purity titanium absorbs hydrogen at the fastest rate until a saturation concentration of approximately 4200 ppm is reached after 50 minutes charging time. The other alloys show no evidence of reaching saturation after 80 minutes charging time. The effect of Ti_3Al is illustrated by comparing the rates for the two Ti-8Al specimens. The alloy given the standard anneal shows a faster absorption rate than the quenched alloy. Indeed, the initial absorption rate for the stabilized Ti-8Al is faster than that for pure titanium. Thus, the hydrogen absorption rate is related to the volume fraction of Ti_3Al in the predicted way. However, the difference in absorption rates for the two Ti-8Al specimens is much less than that found for alloys closer to the Ti_3Al stoichiometric composition (Figure 15). Also the difference in absorption rates for the two Ti-8Al specimens is small compared to the differences between the three different compositions (Figure 16).

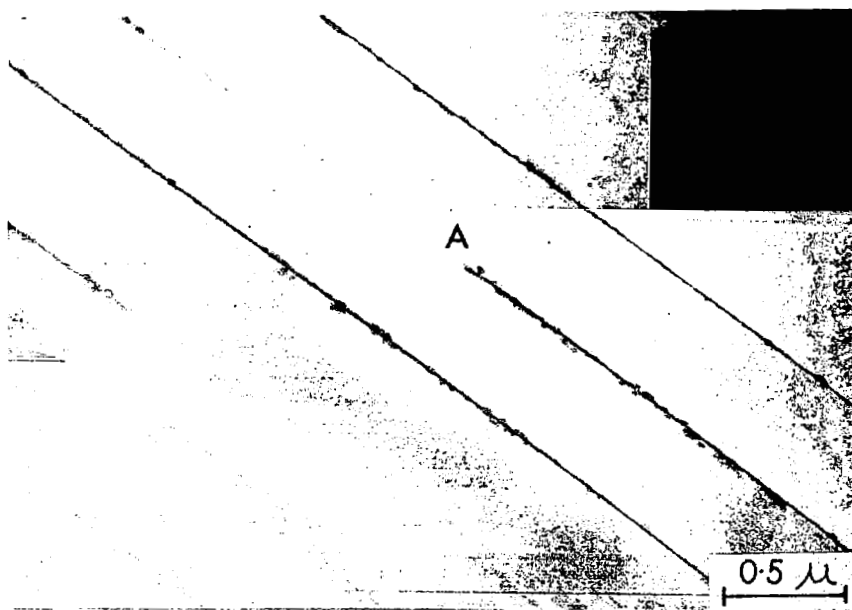
The location of dissolved hydrogen atoms in the h. c. p. titanium lattice has not been determined conclusively, but it is thought that the hydrogen initially enters octahedral interstitial positions, then shifts to tetrahedral sites^(6, 7). Both the "c" and "a" lattice parameters and hence the size of both types of interstitial holes, decrease with increasing aluminum content. Therefore, since interstitial hydrogen expands the titanium lattice,⁽⁷⁾ the rate of hydrogen absorption and equilibrium hydrogen solubility is expected to vary inversely with aluminum content. However, the structure of Ti_3Al is such that the titanium atoms are displaced from their exact DO_{19} superlattice sites so as to form more closely-packed tetrahedra around the aluminum atoms⁽⁵⁾. In this way the size of the octahedral holes is increased and the size of the tetrahedral holes is decreased. Calculations based on the hard-sphere model indicate that the change in size of the interstitial holes can be as much as 5 percent. This increase in the size of the octahedral holes accounts for the very rapid hydrogen absorption rates for ordered Ti_3Al compared with a disordered alloy of the same composition. Thus, there are two competing effects which influence the hydrogen absorption rates in Ti-Al alloys. Increasing the aluminum content should decrease the size of the interstitial holes but, at higher aluminum contents, Ti_3Al will begin to form which absorbs hydrogen very rapidly. The results suggest that the effect due to the changes in lattices parameters with aluminum content is dominant. The hydrogen absorption rate is fastest for pure titanium because it has the largest lattice parameters and a perfectly ordered structure. The absorption rate decreases rapidly with increased aluminum content although for a fixed aluminum level the absorption rate can be increased somewhat by increasing the volume fraction of Ti_3Al . The structure and composition of the specimen surface layer will

certainly affect the hydrogen absorption kinetics and could be a factor in the observed relationship between absorption rates and alloy composition. The thickness and/or structure of the oxide or hydride that forms on the surface may depend strongly on alloy composition. This is a possible explanation of the difference in absorption rates between Ti-8Al and Ti-5Al-2.5Sn which have roughly equivalent α -stabilizer contents.

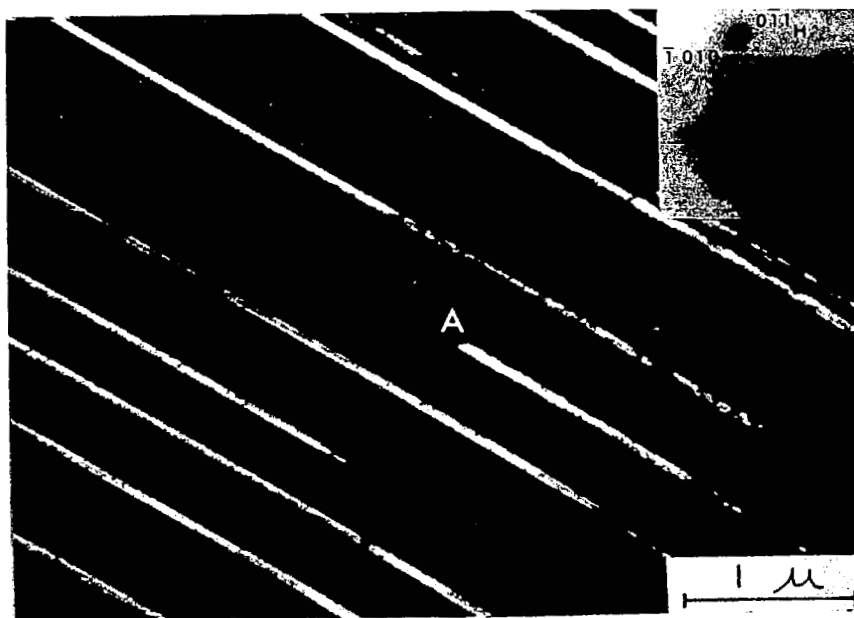
Mechanism of Hydride Nucleation

Further study was made of the strain-induced nucleation of hydrides in Ti-8Al-1Mo-1V at low hydrogen contents (200-400 ppm). Figure 17 illustrates the morphology of the strain-induced hydrides. The structure of the strain-induced hydride was determined by electron diffraction to be b. c. c. with "a" = 3.3 Å. An example of an indexed pattern is given in Figure 18. The orientation relationship between the h. c. p. matrix and the b. c. c. hydride was found to be $(0001)_\alpha \parallel (011)$, $[\bar{1}\bar{1}20]_\alpha \parallel [1\bar{1}1]$ (Figure 19). By locating the trace of the hydride habit planes on each indexed diffraction pattern, it was possible to determine the orientation of the habit-plane interface relative to the two lattices. In the example shown in Figure 18 the trace of the habit plane corresponds to $(1\bar{1}00)_\alpha$, which is parallel to $(21\bar{1})$ in the b. c. c. hydride lattice. The atomic structure of the habit-plane interface is best visualized by considering sections normal to the interface. From the $[\bar{1}\bar{1}20]_\alpha$ section (Figure 20(a)), it can be seen that there is exact correspondence between the $(0001)_\alpha$ planes and the (011) hydride planes. The $[0001]_\alpha$ section (Figure 20(b)), shows planes which are discontinuous across the interface since the spacing of two $(\bar{1}\bar{1}20)_\alpha$ planes is almost equal to the spacing of three $(1\bar{1}1)$ planes in the hydride lattice. It is suggested that this small misfit can be accommodated by an array of $\frac{a}{3}[\bar{1}\bar{1}20]$ edge dislocations like the one illustrated in Figure 21. By considering separately the arrangement of atoms on either side of the interface, it may be seen that such an interface dislocation corresponds to an $\frac{a}{3}[\bar{1}\bar{1}20]$ dislocation in the h. c. p. lattice, and to an $\frac{a}{2}[1\bar{1}1]$ dislocation in the b. c. c. lattice. Both of these Burgers vectors are the ones having the lowest energy in their respective lattices, and would constitute a relatively low-energy semicoherent interface. Thus, the structure across the habit-plane interface is such that there is zero misfit in the $[0001]_\alpha$ direction, and a 2 percent misfit in the $[\bar{1}\bar{1}20]_\alpha$ direction, which can be accommodated by an array of parallel $\frac{a}{3}[\bar{1}\bar{1}20]$ edge dislocations. The equilibrium spacing of the interface dislocations can be calculated from the Brooks formula⁽⁸⁾, and is found to be approximately 150 Å.

The dislocation structure of the habit-plane interface of the strain-induced hydrides was characterized by electron microscopy, using the standard g, b analysis. Due to the preferred orientation of the starting material, it was not possible to obtain micrographs with the habit-plane interfaces parallel to the plane of the micrograph. Thus, the hydrides were always inclined to the surface of the foil, which meant the dislocation images were often obscured by displacement-fringe contrast⁽⁹⁾. Figure 22 illustrates that under these conditions the images of the interface dislocations can be very complex compared to the clear images of the dislocations in the matrix. Nevertheless it was possible to identify the Burgers vector of the interface dislocations as $\frac{a}{3}\langle\bar{1}\bar{1}20\rangle$. Figure 23 shows an array of such dislocations which are in the edge orientation, although their spacing is somewhat larger than the equilibrium spacing of 150 Å. Generally, however, the interface dislocations were of mixed character, such as those shown in Figure 23(b).

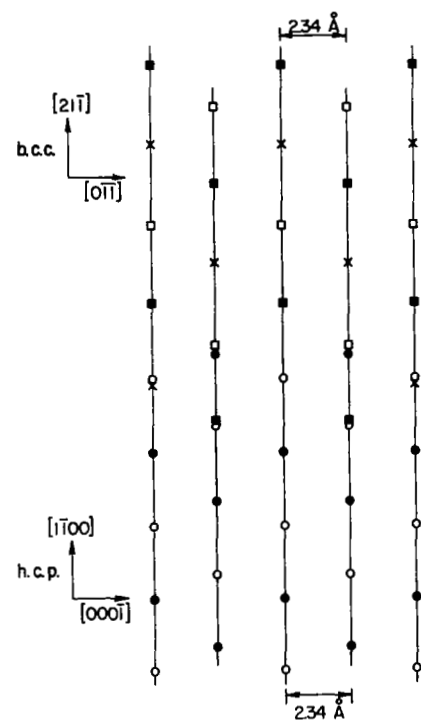


(a) Dark-field micrograph from $(0\bar{1}1)$ hydride reflection

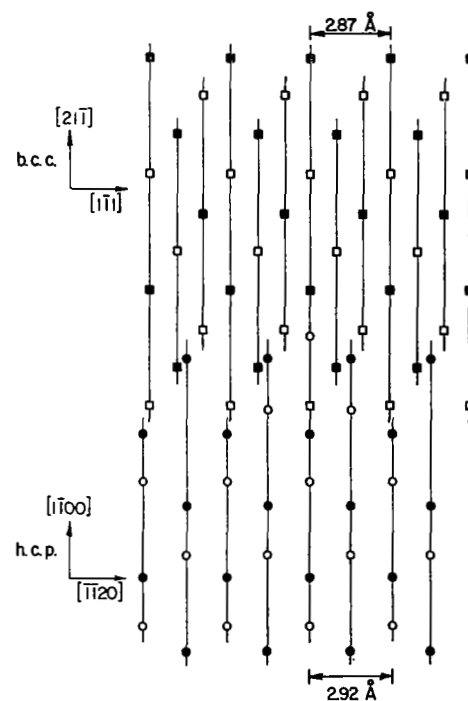


(b) Same area tilted to make (1100) planes normal to the plane of the micrograph

FIGURE 17. Ti-8Al-1Mo-1V, CHARGED WITH 400 ppm H_2 , THEN DEFORMED APPROXIMATELY 2 PERCENT AT ROOM TEMPERATURE, SHOWING HYDRIDES ON $(\bar{1}100)$ SLIP PLANES



(a) $[1\bar{1}20]_{\alpha}$ section.



(b) $[0001]_{\alpha}$ section.

FIGURE 20. STRUCTURE OF THE HABIT-PLANE INTERFACE OF STRAIN-INDUCED HYDRIDE, ●, ○ ATOMS IN α LATTICE; ■, □, x ATOMS IN HYDRIDE LATTICE

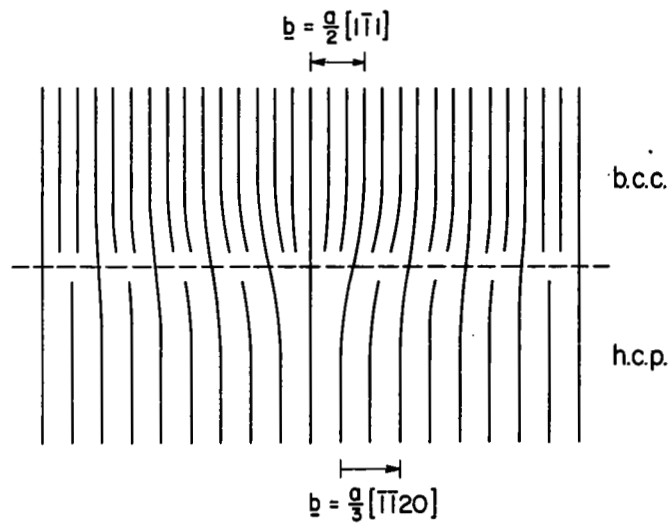


FIGURE 21. STRUCTURE OF AN INTERFACE DISLOCATION BETWEEN A b.c.c. AND AN h.c.p. LATTICE

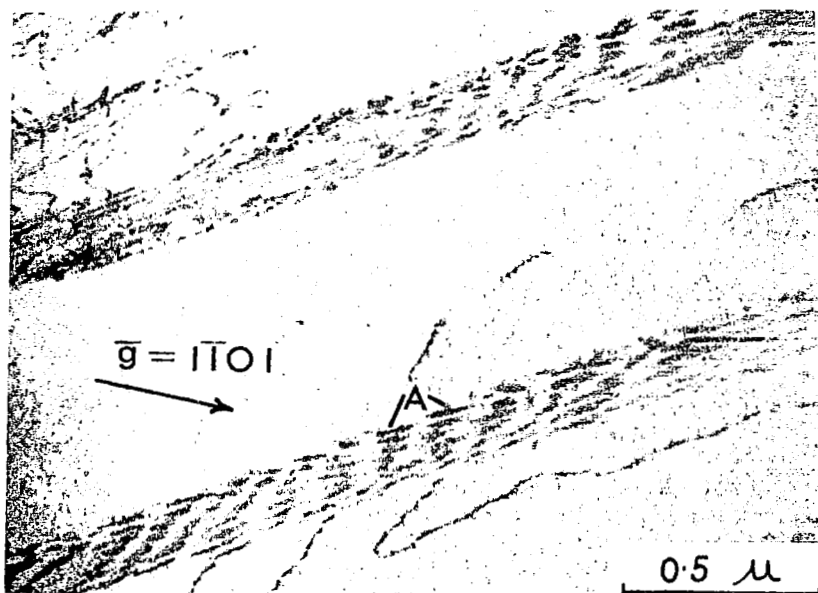
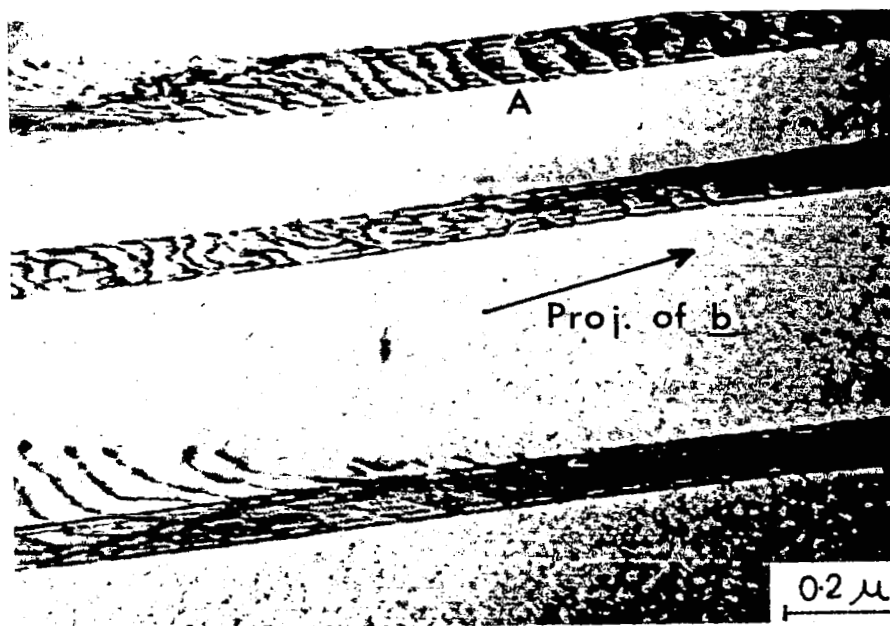
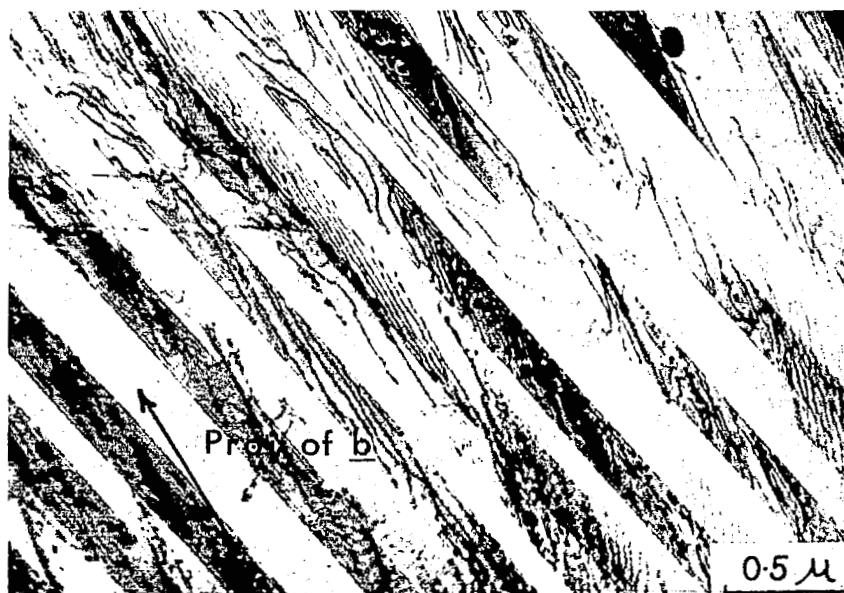


FIGURE 22. STRAIN-INDUCED HYDRIDES [COMPARE THE BROAD IMAGES OF THE INTERFACE DISLOCATIONS (E. G., AT A) WITH THE NORMAL IMAGES OF THE MATRIX DISLOCATIONS]



(a) Dislocations in edge orientation (e. g., at A)



(b) Dislocations of mixed character

FIGURE 23. STRAIN-INDUCED HYDRIDES, SHOWING THE DISLOCATION STRUCTURE OF THE HABIT-PLANE INTERFACES

The nucleation mechanism of the strain-induced hydrides is discussed in detail elsewhere⁽¹⁰⁾. The important conclusions of this work are:

- (1) The specific volume of the b. c. c. hydride phase is only 4 percent larger than that of the Ti-8Al α phase. Hence the elastic strain energy is a small fraction of that involved in the nucleation of γ .
- (2) The structure of the b. c. c. hydride phase is such that a low energy, semicoherent interface can exist between it and the α phase. The interface dislocations which constitute the semicoherent interface have as Burgers vector $\underline{b} = \frac{a}{3} [\bar{1}\bar{1}20]_{\alpha}$ which is exactly equivalent to $\underline{b} = \frac{a}{2} [1\bar{1}1]$ in the b. c. c. lattice. This is the ideal interface dislocation since it has the lowest energy \underline{b} for both lattices. Furthermore, there is no difficulty in forming the interface dislocations since the glide dislocations in the deformed α grains are available.
- (3) The glide dislocations in the α phase act as heterogeneous nucleation sites, and hydrogen diffusion is sufficiently rapid that significant hydride growth can occur during deformation at ordinary strain rates. It is possible that movement of the $\frac{a}{3} [\bar{1}\bar{1}20]$ dislocations in $(1\bar{1}00)$ planes could assist the edgewise growth of the hydride plates.

Effect of Hydrogen on the Tensile Properties of Ti-8Al-1Mo-1V

A series of 0.020-inch thick strip tensile specimens of Ti-8Al-1Mo-1V were deformed to fracture to determine the effect of hydrogen content and strain rate on the room-temperature tensile properties. The nominal stress-elongation curves are shown in Figure 24, and the tensile data are summarized in Table 20. The microstructure of the two 400-ppm specimens was studied after deformation by transmission electron microscopy. The electron-microscopy specimens were cut from the gauge lengths, remote from the necked regions. Both the high and low strain-rate specimens contained strain-induced hydrides lying in the prismatic slip bands.

TABLE 20. EFFECT OF HYDROGEN CONTENT AND STRAIN RATE ON THE TENSILE PROPERTIES OF Ti-8Al-1Mo-1V

Specimen	H ₂ Content, ppm	$\dot{\epsilon}$, per min ⁻¹	Yield Stress, ksi	Reduction in Area, percent	Elongation, percent
A	1000	3	149	--	3.2
B	400	3	148	25	16
C	400	3×10^{-3}	145	24	20
D	80(a)	3	142	18	14
E	80(a)	3×10^{-3}	127	22	17

(a) Base hydrogen content.

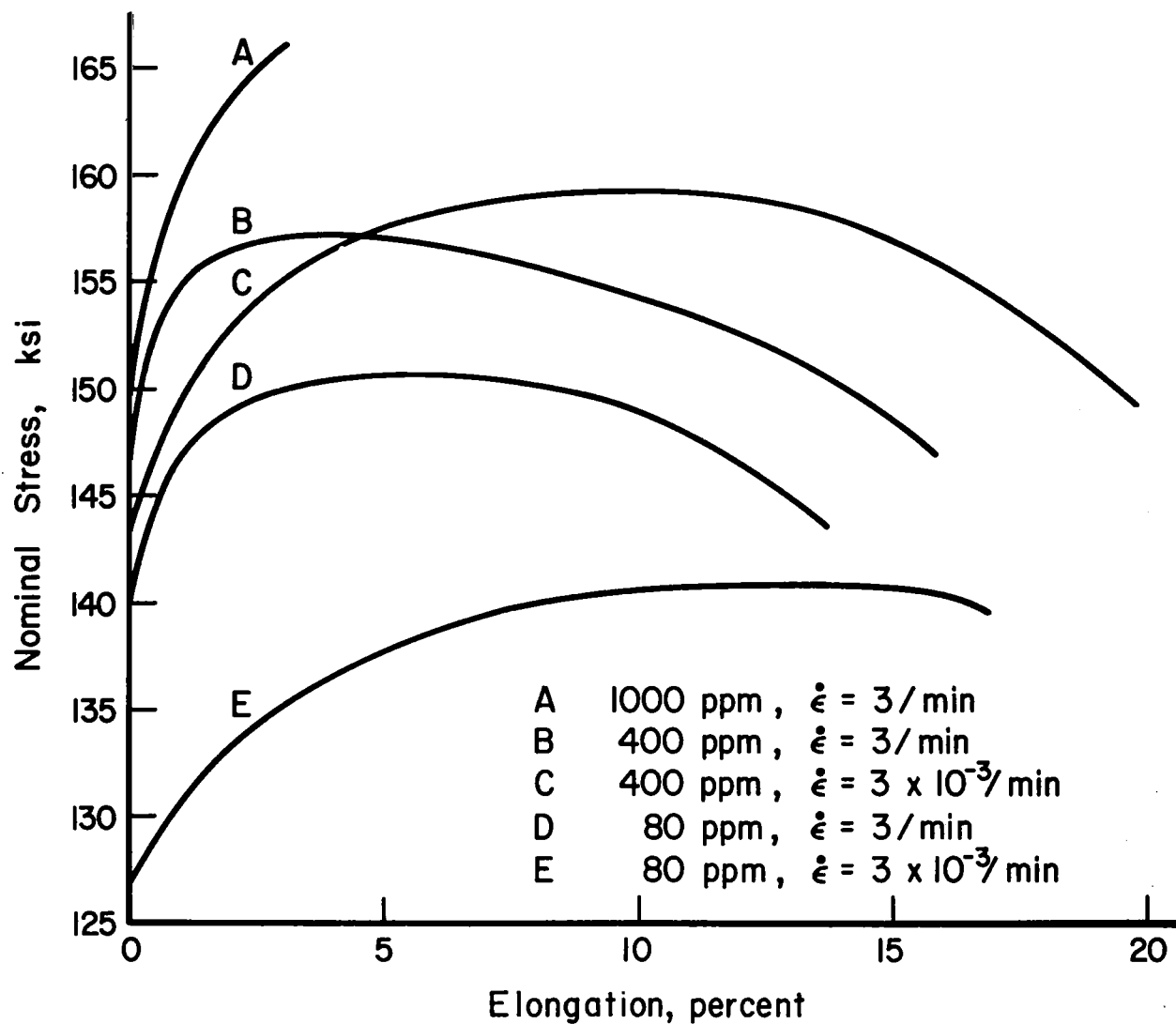


FIGURE 24. EFFECT OF HYDROGEN ON THE ROOM-TEMPERATURE TENSILE PROPERTIES OF Ti-8Al-1Mo-1V

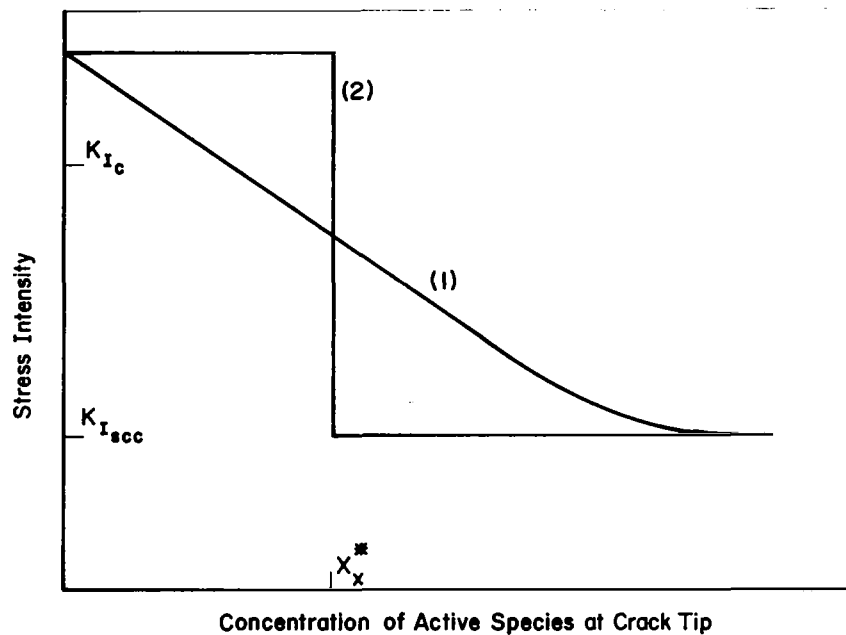


FIGURE 25. SCHEMATIC ILLUSTRATION OF POSSIBLE RELATIONSHIPS BETWEEN THE CRITICAL CONCENTRATION OF SPECIES X AND THE STRESS INTENSITY, K_I

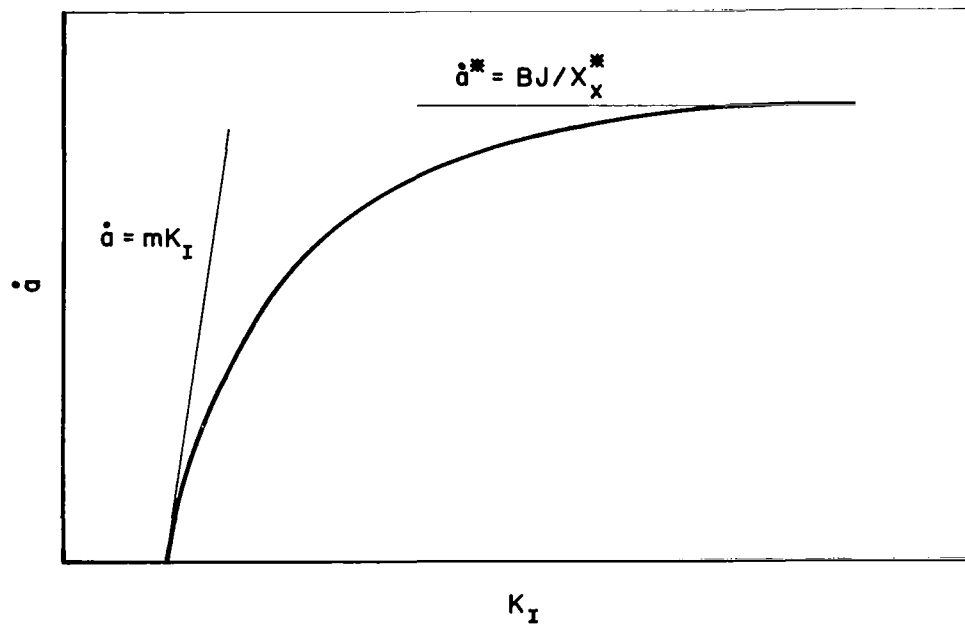
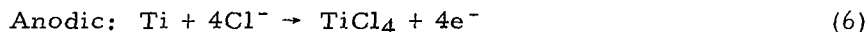


FIGURE 26. SCHEMATIC INTERPRETATION OF THE RELATIONSHIP BETWEEN CRACK VELOCITY AND STRESS INTENSITY

with all the experimental observations presently available is the one outlined in the previous report⁽¹⁾, whereby strain-induced hydrides form in the active $\{10\bar{1}0\}$ slip bands and inhibit plastic flow around the crack tip. It was shown that during the propagation of a stress-corrosion crack in 3.5 percent NaCl the hydrogen concentration at the surface of Ti-8Al-1Mo-1V could be as much as 300 ppm, and this is sufficient to nucleate strain-induced hydrides. This is a conservative estimate of the amount of hydrogen absorbed from the aqueous environment. The amount of absorbed hydrogen could be increased by the presence of Ti_3Al . The measurements of hydrogen absorption kinetics show that the overall hydrogen absorption rate in Ti-8Al is not changed much by increasing the amount of Ti_3Al . However, pure Ti_3Al absorbs hydrogen very rapidly and, in an alloy containing Ti_3Al particles, there could be localized areas on the crack surface where hydrogen is absorbed at a rate higher than the average for the whole surface. The tensile data reported in Table 18 and Figure 14 show that the yield stress of Ti-8Al-1Mo-1V is significantly higher in salt water than in air. Furthermore, this increment in yield stress is largest for the thinnest specimens indicating a surface-hardening effect due to the aqueous environment. It is interesting that the difference between the air and salt-water values of the yield stress for the 0.020-inch specimens is comparable to the yield stress increment produced by the presence of strain-induced hydrides (Table 20). Therefore, it is concluded that sufficient hydrogen can enter Ti-8Al-1Mo-1V during aqueous stress-corrosion cracking to nucleate strain-induced hydrides in the vicinity of the crack tip, and that the hydrides increase the yield stress of the material by blocking the egress of dislocations where $(10\bar{1}0)$ slip bands intersect the crack surface. Unfortunately, no direct evidence has been found for the existence of strain-induced hydrides in specimens deformed in salt water.

The effect of active species in the environment on the cleavage strength of the α phase is less well understood. Subcritical cracking has been found to occur in Ti-8Al-1Mo-1V in a dry-air environment due to migration of hydrogen to the crack-tip region⁽¹¹⁾. In addition cleavage cracks form when the same alloy is deformed in a pure hydrogen atmosphere⁽¹⁷⁾. Thus there is some evidence that hydrogen reduces the cleavage strength of α -titanium. However, in an aqueous environment there are other species such as halide ions that could adsorb at the crack tip and reduce the cleavage strength. Since the crack velocity increases with increasing chloride-ion concentration (Figure 9), it could be argued that cleavage results from the adsorption of those ions. However, the amount of hydrogen released at the cathodic regions of the crack tip is proportional to the amount of chloride ion that reacts with titanium at the anodic region according to the equations:



Hence the results of the crack-velocity experiments do not identify the active species in the aqueous environment. Experiments are in progress to determine the fracture energy of Ti-8Al-1Mo-1V in air and salt water. This is being done by measuring the fracture stress as a function of grain size and doing a Stroh-Petch analysis. In addition, a theoretical study is planned to determine the effect of various adsorbed species on the cleavage strength of titanium. The arrangement of atoms in the vicinity of a crack tip is being studied at Battelle by means of computer simulation. It is hoped to extend this technique to the case of cracks with adsorbed foreign atoms at the surface.

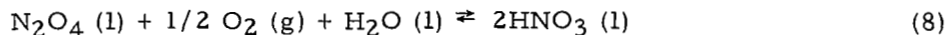
To summarize, the experimental observations show that hydrogen is absorbed by titanium alloys during aqueous stress-corrosion cracking and that small quantities of hydrogen can lead to cleavage cracking. Therefore, it is concluded that hydrogen is an important factor in the aqueous stress-corrosion cracking of titanium alloys.

N₂O₄ Environments

Chemical Study

Previous work has shown that "green" N₂O₄ which contains H₂O and NO does not produce stress-corrosion cracking of Ti-6Al-4V alloy. This alloy is, however, susceptible in "red" N₂O₄.

It was proposed in earlier work from thermodynamic considerations that HNO₃ would be produced in the N₂O₄ - H₂O - NO (i. e. , "green" N₂O₄) system with the presence of O₂. Thus, in the presence of O₂, "green" N₂O₄ can be converted into "red" N₂O₄, and "red" N₂O₄ should contain HNO₃ from the reaction



In order to test the validity of this proposal, an experiment was conducted to produce HNO₃ by this chemical reaction. The apparatus used is shown in Figure 27.

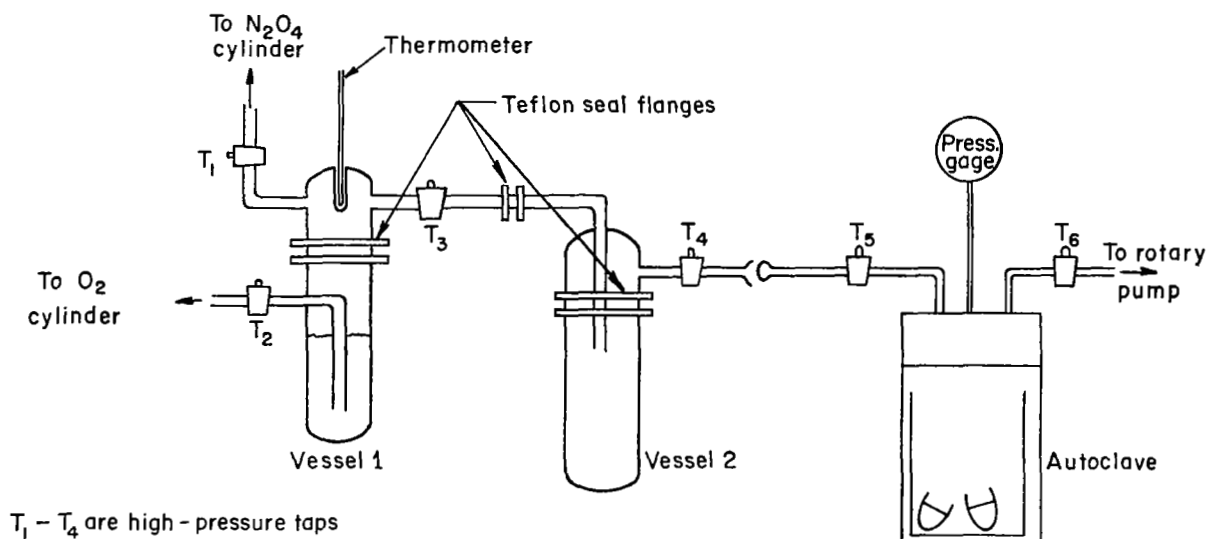


FIGURE 27. APPARATUS FOR PREPARING HNO₃ FROM N₂O₄

Vessels 1 and 2 were purged with O₂ and evacuated. 3.6 ml of distilled H₂O and 100 ml of "green" N₂O₄ were then admitted to Vessel 1 via Tap T1. Taps T1 and T3 were

closed and O₂ admitted into Vessel 1 until the pressure was 20 psig. For a period of 4 days, O₂ was admitted into Vessel 1 to retain the pressure at 20 psig. On the second day, the solution had changed from a dark green color to a very clear red color, and a viscous liquid layer was evident at the bottom of the vessel. At the end of the fourth day, very little drop in O₂ pressure had occurred, indicating that equilibrium had been established. Vessel 2 was then placed in ice and evacuated. The remaining N₂O₄ (red) in Vessel 1 was distilled into Vessel 2 at a temperature between 70 and 80 F until only the reddish-brown viscous liquid layer remained in Vessel 1. This reddish-brown solution was analyzed and found to contain 58.0 percent HNO₃, 37.7 percent NO₂, and 4.3 percent H₂O. The HNO₃ produced was 70 percent of the theoretical yield according to Reaction (8). The experiment indicated that Reaction (8) occurs at a reasonable rate even at pressures as low as 20 psig O₂, and thus substantiated the thermodynamic considerations. (These considerations are in agreement with analytical experiments conducted by other workers.⁽¹⁸⁾)

Experiments have been continued in which small H₂O additions (0.20 ml/500 ml "green" N₂O₄) have been made to commercial "green" N₂O₄. Solution-heat-treated-and-aged and annealed Ti-6Al-4V U-bend specimens have been exposed to these environments in the presence of oxygen (Figures 28 and 29). These experiments are summarized in Table 21. The experiments summarized in Table 21 were conducted using apparatus

TABLE 21. EFFECT OF OXYGEN PRESSURE ON THE STRESS-CORROSION-CRACKING BEHAVIOR OF TYPE Ti-6Al-4V U-BENDS IN N₂O₄

Solution	Partial Gas Pressures, psig	Exposure Time, hr	Temperature, F	Results
0.20 ml H ₂ O per 500 ml green N ₂ O ₄	250 O ₂	60	104	All failed (large cracks, see Figure 28)
0.20 ml H ₂ O per 500 ml green N ₂ O ₄	90 O ₂ 160 He	60	104	All failed (microcracks) see Figure 29
0.20 ml H ₂ O per 500 ml green N ₂ O ₄	65 O ₂	60	104	No failures

described in a previous report⁽¹⁾. The results indicated that in the presence of 0.2 ml H₂O in 500 ml green N₂O₄, a critical O₂ pressure range exists above which stress-corrosion cracking occurs. The critical O₂ pressure range for this system was between 65 and 90 psig O₂, (i.e., between 4.5 and 6.0 atm O₂) at 104 F. In order to determine the HNO₃/H₂O ratio present in the system at critical pressures between 65 and 90 psig O₂, it was first required to determine the partial oxygen pressure in the liquid N₂O₄ phase at autoclave pressures of 65 to 90 psig O₂, and the partial pressure of oxygen which had undergone reaction. In the experiments summarized in Table 21, the total number of moles of oxygen used in reaction and dissolved in the liquid N₂O₄ was determined by the pressure drop in the system. The final equilibrium oxygen partial-pressure value was then used to determine the moles of oxygen dissolved in the liquid

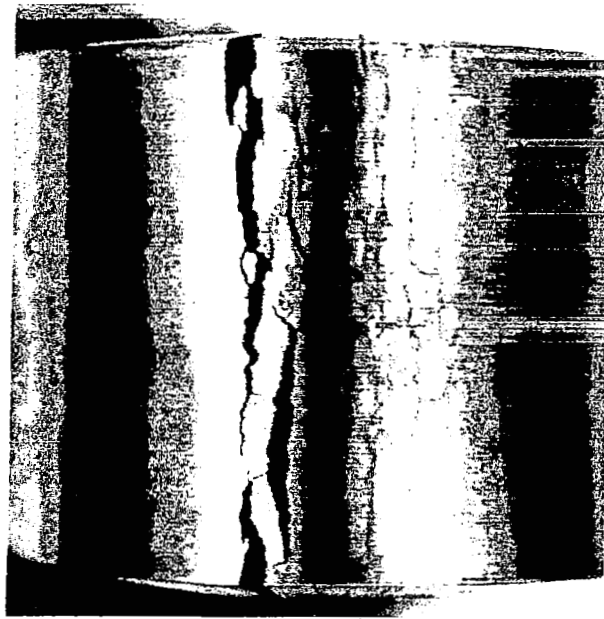


FIGURE 28. Ti-6Al-4V SOLUTION-HEAT-TREATED-AND-AGED U-BEND EXPOSED TO 500 ml N_2O_4 WITH 0.2 ml H_2O ADDITION AND 250 psig O_2

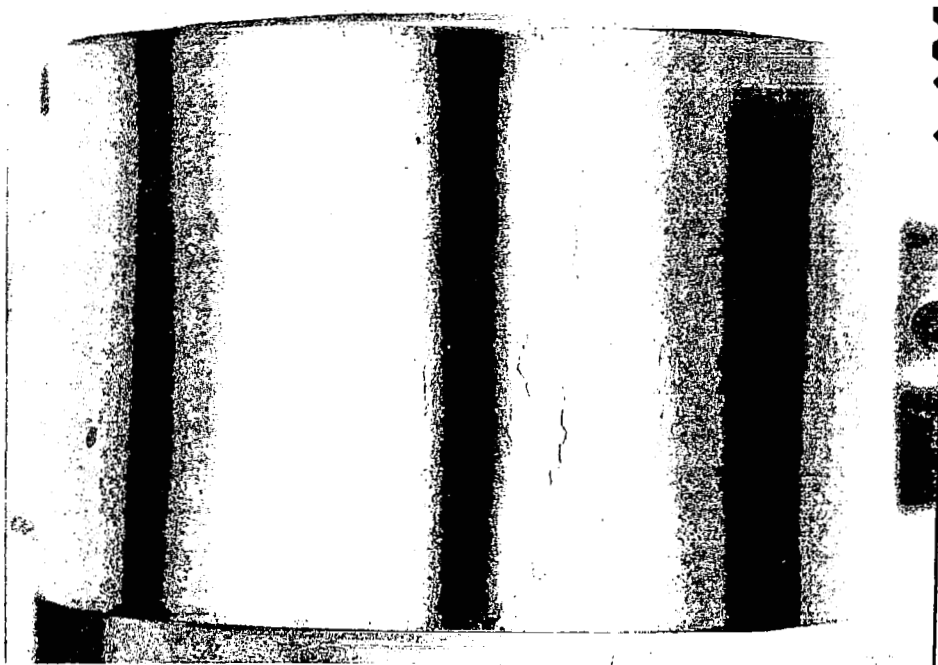


FIGURE 29. Ti-6Al-4V SOLUTION-HEAT-TREATED-AND-AGED U-BEND EXPOSED TO 500 ml N_2O_4 WITH 0.2 ml H_2O ADDITION AND 90 psig O_2

N_2O_4 , using the solubility data of Chang and Gokeen⁽¹⁹⁾. The moles of oxygen used in Reaction (8) and in Reaction (9)



were thus determined and, by means of equilibrium equations similar to those used in Quarterly Reports 4 and 5, the $\text{HNO}_3/\text{H}_2\text{O}$ ratios were calculated. The results of the $\text{HNO}_3/\text{H}_2\text{O}$ ratio calculations are summarized in Table 22. Data in Table 22 indicate that at oxygen pressures of 65, 90, and 250 psig, the original green N_2O_4 system containing additions of 0.20 ml $\text{H}_2\text{O}/500$ ml N_2O_4 has calculated values of 2531, 2778, and 7836, respectively, for the $\text{HNO}_3/\text{H}_2\text{O}$ ratio. Since the data in Table 21 indicate that the pressure range between 65 and 90 psig O_2 is a critical stress-corrosion-cracking condition, it must be concluded that this critical condition is associated with a $\text{HNO}_3/\text{H}_2\text{O}$ solution ratio between 2500 and 2800 for the specified composition of green N_2O_4 at a temperature of 104 F. At such $\text{HNO}_3/\text{H}_2\text{O}$ ratios and larger, the N_2O_4 is, of course, in the red condition.

TABLE 22. CALCULATED $\text{HNO}_3/\text{H}_2\text{O}$ RATIOS IN OXYGEN PRESSURIZED N_2O_4

Oxygen Pressure, psig	H_2O Added/ 500 ml N_2O_4	Calculated Moles $\text{HNO}_3/500$ ml N_2O_4	Calculated Moles $\text{H}_2\text{O}/500$ ml N_2O_4	$\text{HNO}_3/\text{H}_2\text{O}$
65.0	0.20 ml	$6.383 \cdot 10^{-2}$	$2.521 \cdot 10^{-5}$	2531
90.0	0.20 ml	$6.383 \cdot 10^{-2}$	$2.298 \cdot 10^{-5}$	2778
250	0.20 ml	$6.386 \cdot 10^{-2}$	$8.15 \cdot 10^{-6}$	7836

Autoradiographic Experiments. At the time of the above work, the $\text{HNO}_3/\text{H}_2\text{O}$ ratio in N_2O_4 appeared extremely significant in the stress-corrosion-cracking mechanism. Although the red N_2O_4 system appeared to be an oxidizing system, it was believed that HNO_3 could possibly play a role in the stress-corrosion-cracking mechanism by means of hydrogen embrittlement, and that this possibility could not be overlooked. Three autoradiographic experiments were therefore undertaken using tritiated H_2O additions (0.20 ml and 0.50 ml $\text{H}^3_2\text{O}/500$ ml green N_2O_4) to green N_2O_4 and subsequent pressurization with oxygen to 250 psig. The apparatus for doping the N_2O_4 was similar to that described in Figure 20 in Quarterly Report 5. It was believed that under the given conditions, the tritiated H^3_2O would be converted into H^3NO_3 according to Reaction (8). If hydrogen embrittlement was involved in the stress-corrosion-cracking mechanism, it was believed that up to a small distance adjacent to the cracks the failed U-bends would retain sufficient tritiated hydrogen (in solution or possibly as a hydride phase) to produce autoradiographs. Samples of tritiated H_2O at radiation levels of 20 mc/ml and 1000 mc/ml were used in the experiments together with U-bends and unstressed specimens of Ti-6Al-4V alloy in both the solution-heat-treated-and-aged and annealed conditions. The results of the experiments are summarized in Table 23. Table 23 shows that in all three experiments the U-bends failed in less than 60 hours at 104 F but that the presence of tritiated hydrogen could not be detected in the failed U-bends by means of the autoradiographic technique. It should be noted, however, that

the detection limit of this technique was approximately 200 ppm H_2 (0.238 ppm radioactive H_2) based upon the requirement of 5×10^7 β disintegrations per cm^2 for a measurable autoradiograph and an exposure period of 1 month. A hydrogen embrittlement mechanism cannot therefore be conclusively ruled out based on this experiment. However, as shown later from potential measurements the hydrogen embrittlement theory does become more doubtful.

TABLE 23. TRITIATED H^3_2O STUDIES IN N_2O_4 *

H^3_2O add n/500 ml green N_2O_4 , ml	H^3_2O Radiation Level, mc/ml	Oxygen Pressure, psig	Results
0.20	20	250	U-bends failed. All autoradiographs negative
0.50	20	250	U-bends failed. All autoradiographs negative
0.20	1000	250	U-bends failed. All autoradiographs negative

*Exposure time of 60 hr at a temperature of 104 F. Autoradiographic films exposed at least 4 weeks to U-bends after failure.

Potential Measurements. In order to measure the potential of a Ti-6Al-4V U-bend specimen in N_2O_4 , the cell shown in Figure 30 was used.

The cell contained a Ti-6Al-4V U-bend specimen similar to specimens exposed in the autoclave tests. Smooth Pt and Ag/AgCl electrodes were used as reference electrodes in this experiment. The Ag/AgCl electrodes were prepared from 5- cm^2 platinum substrates according to the method described in the literature⁽²⁰⁾. In the cell used above, the N_2O_4 was thermostated at 32 F by the use of an ice-water bath. Potential measurements were made using a Model 602 Keithley solid-state electrometer which possesses a very high input impedance of $>10^{14}$ ohms. This instrument is particularly useful for measurements in electrolyte solutions of very low conductance.

The cell was first evacuated using a rotary pump and then green N_2O_4 was added in sufficient quantity to cover the Pt and Ag/AgCl electrodes and also the lower half (apex) of the U-bend specimen. The electrode potential of the Ti-6Al-4V specimen was quickly established at a value between +0.7 and +0.8 volt vs. the Ag/AgCl electrode and remained at this value for a period of 2 hours. The measurements vs. the Pt electrodes gave a value of +1.5 to +1.6 volts but the Pt electrodes appeared highly irreversible. Upon the passage of O_2 into the green N_2O_4 , the potential moved to +2.5 volts vs. Ag/AgCl electrode within 4 minutes and then steadily decreased to a value +1.2 volt at which time O_2 was stopped and the color of the solution had changed from dark green to an orange brown. Several experiments were attempted to pass O_2 into the system for a longer period of time, but it was found impossible to retain the temperature at 32 F overnight and the N_2O_4 boiled off. Attention was therefore turned toward an experiment

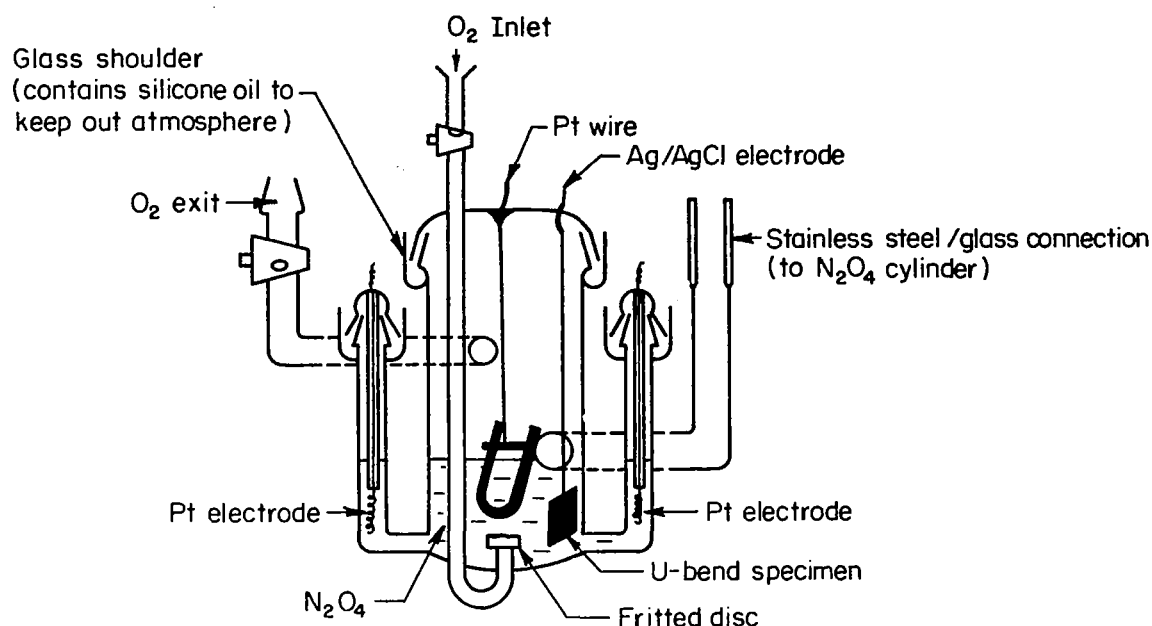


FIGURE 30. ELECTROCHEMICAL CELL FOR POTENTIAL MEASUREMENTS

in an autoclave. Such an experiment was also considered as more typical of previous stress-corrosion-cracking studies. The autoclave used in this experiment was adapted such that the autoclave top contained two spark plugs which served as electrical connections to an Ag/AgCl reference electrode and a Ti-6Al-4V U-bend specimen. In this experiment, Ag sheet was used as the substrate for the Ag/AgCl electrode since the previous studies had indicated that Ag/AgCl film on Pt substrates had tended to exfoliate. The area of the Ag/AgCl electrode in this experiment was 24 cm². The autoclave was loaded with green N₂O₄ and pressurized to 250 psig with O₂, and prior to immersion in the thermostated bath, the Ti-6Al-4V U-bend specimen had a potential of +0.56 volt vs. the Ag/AgCl electrode at 74 F. Overnight, the pressure had dropped to 215 psig at 24 F and the potential value was +0.56 volt. The autoclave was then immersed in a bath at 102 F. The potential was continuously recorded for a period of 5 days in which time the potential increased slowly to a value of +0.85 volt at 102 F with a pressure of 210 psig. The pressure on the system was decreased to 45 psig for a period of 24 hours; however, the potential remained at +0.85 volt. The electrode was removed and found to have cracked at the apex of the U-bend. The fractured surface was typified by a bluish-and-gold film on the edge and a dull metallic luster on the inside.

Assuming that the Cl⁻ concentration in the N₂O₄ is approximately 0.001 percent, the Ag/AgCl electrode would have a value of approximately +0.42 volt vs. the standard hydrogen electrode for an aqueous solution. Thus, the potential-measurement data appear to indicate that stress-corrosion-cracking occurs at a potential much more noble than the hydrogen-evolution reaction and a hydrogen-embrittlement mechanism. The noble potential value of 0.6 to 0.9 volt, if correct, would indicate that the titanium dissolves in a high

oxidation state (i.e., probably TiO^{++}). However, it should be noted that there is no information concerning the reliability of the Ag/AgCl electrode in this environment and that the potential recorded would be a mixed overall value and not necessarily the value at the crack area. A hydrogen embrittlement theory thus cannot be conclusively ruled out, although it appears doubtful.

Exposure Experiments in Purified N_2O_4 . Previous studies indicated that red N_2O_4 was associated with a large $\text{HNO}_3/\text{H}_2\text{O}$ ratio and it was concluded that it should be possible to distill N_2O_4 from red N_2O_4 which would not crack type Ti-6Al-4V U-bend specimens. Thus it was believed that distillation would give a pure N_2O_4 distillate which did not have stress-corrosion-cracking properties. The following series of experiments was conducted using the apparatus shown in Figure 31.

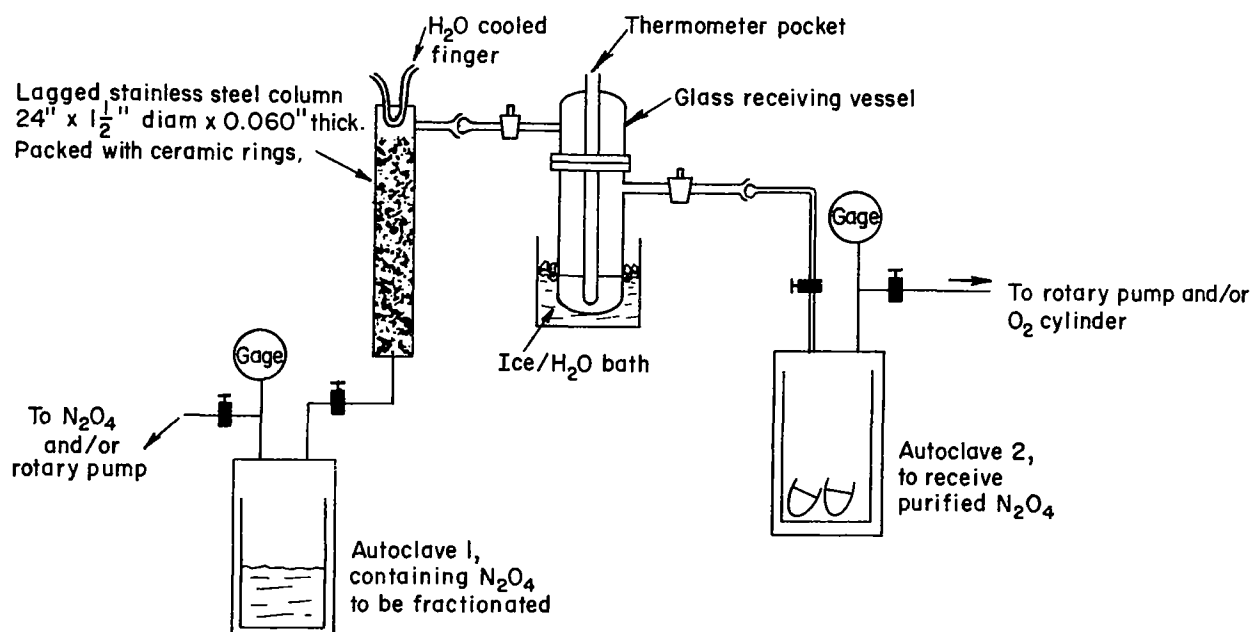
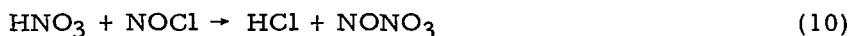


FIGURE 31. APPARATUS FOR DISTILLATION OF N_2O_4

In the first experiment, 500 ml of green N_2O_4 was pressurized for 5 days at 250 psig with O_2 at 104 F to assure the production of red N_2O_4 . The pressure was reduced and 100 ml N_2O_4 was distilled into the evacuated glass vessel and then redistilled into the evacuated autoclave containing solution-heat-treated-and-aged and annealed Ti-6Al-4V U-bend specimens. These specimens failed after exposure for 3 days at 104 F and 250 psig O_2 , and contained large cracks. Over successive days, two further 100-ml and one 60-ml fractions were distilled from Autoclave 1 and transferred to autoclaves containing Ti-6Al-4V U-bend specimens. These autoclaves were similarly pressurized to 250 psig with O_2 and exposed for 3 days at 104 F. In these further three exposure tests, the U-bends failed due to the presence of very fine cracks at the apex of the U-bends.

In the second experiment, 75 gm of P_2O_5 was added to the 500 ml green N_2O_4 and the system was pressurized with O_2 at 250 psig for 4 days at 104 F. P_2O_5 was added because of the possibility that H_2O in the system was being distilled with the N_2O_4 and converted to HNO_3 (as per Reaction (8)) upon pressurization with O_2 . It was believed that P_2O_5 would be an efficient dehydrating agent. To insure that H_2O was not admitted by means of a contaminant in the O_2 gas, the gas line was passed through a CO_2 /acetone bath. The latter procedure was continued for all further experiments. 100 ml of the N_2O_4 was distilled into the glass vessel using the apparatus shown in Figure 31. The N_2O_4 was frozen using CO_2 /acetone; it had a freezing point of +12 F and was colorless. $NOCl$ and HCl were possible contaminants in the N_2O_4 . As a precaution against the carry-over of HCl with the N_2O_4 , which could be produced according to Reaction (10), the vessel containing the frozen N_2O_4 was evacuated using a rotary

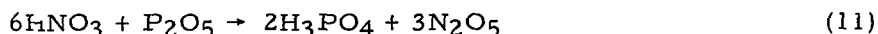


pump. The temperature was allowed to increase slightly during evacuation in order to remove $NOCl$. The N_2O_4 was then melted and passed into a second evacuated autoclave containing Ti-6Al-4V and Ti-75A U-bend specimens. The autoclave was pressurized with helium to 250 psig and the specimens were exposed for 3 days at 104 F. After 3 days, there were no failures of the solution-heat-treated-and-aged Ti-6Al-4V, the annealed Ti-6Al-4V, or the Ti-75A U-bend specimens.

Prior to removal of the specimens from the autoclave, the N_2O_4 was distilled directly into another evacuated autoclave containing similar U-bend specimens. The latter autoclave was pressurized to 250 psig with O_2 and maintained at a temperature of 104 F for 3 days. After 3 days, all specimens had failed due to microcracks; however, a leak had developed in the autoclave and the pressure had dropped to zero. A further 100 ml was distilled from the green $N_2O_4 - P_2O_5 - O_2$ system, and the freezing point of the N_2O_4 was recorded as between +14 and +12 F. The evacuated gases from above the solidified material were drawn into a glass vessel and retained. The 100 ml of N_2O_4 was then transferred to an autoclave containing Ti-6Al-4V and Ti-75A U-bend specimens, and the autoclave was pressurized to 250 psig with O_2 . These specimens were exposed for 5 days at 104 F. After 5 days all specimens had failed. The retained vapors were dissolved in 50 ml of deionized H_2O ; an analysis showed 6 ppm Cl^- and the absence of phosphorus.

The second experiment was repeated using a small amount (30 gm) of P_2O_5 . The vapors from the first distillate were found to contain 15 ppm Cl^- in 50 ml H_2O . The N_2O_4 was further dried with P_2O_5 before being passed into the second autoclave and pressurized with O_2 at 250 psig. After 5 days of exposure at 106 F, Ti-6Al-4V and Ti-75A U-bend specimens had failed. The residue in the glass container, after burn-off, was dissolved in 50 ml of deionized H_2O and an analysis revealed 50 - 100 parts Ti: 30 parts V: 7 parts Al. This ratio suggests that the β phase, which contains vanadium as a stabilizer, is the most susceptible phase to dissolution of the Ti-6Al-4V alloy.

It was realized that in these exposure experiments, failures had occurred only in those systems containing N_2O_4 pressurized with O_2 . Furthermore, it was realized that in the experiments in which N_2O_4 was reacted with P_2O_5 some N_2O_5 could have been produced in the system by the reaction



and that the N_2O_5 could play a role in the stress-corrosion-cracking mechanism. It was therefore considered necessary to conduct an experiment in which N_2O_5 was added to the green N_2O_4 .

An experiment was conducted in which 25 ml of 99 percent RFNA was reacted with 15 g P_2O_5 according to a method described in the literature⁽²¹⁾. The temperature of the reaction vessel was increased slowly from -43 to +77 F; at +77 F the solution effervesced. The reaction was completed at +95 F. The N_2O_5 was passed into an evacuated autoclave containing Ti-6Al-4V and Ti-75A U-bend specimens. 250 ml green N_2O_4 was added and the autoclave was pressurized to 250 psig with helium. The specimens were exposed for 4 days at a temperature of 104 F after which time it was noted that burn-off did not occur readily and that a deep orange-red liquid remained. There were no failures in any of the exposed specimens. This experiment indicated that N_2O_5 does not play a major role in the stress-corrosion-cracking mechanism. Furthermore, it should be noted that N_2O_5 would react with the H_2O present in the green N_2O_4 and produce HNO_3 according to Reaction (12):



This reaction is expected to be well "to the right" since its free energy change is -9.53 kcal/mole at 298 K. A large $\text{HNO}_3/\text{H}_2\text{O}$ ratio would thus be anticipated in the solution due to the reaction between green N_2O_4 and N_2O_5 . This experiment therefore suggests that a large $\text{HNO}_3/\text{H}_2\text{O}$ ratio is not the only requirement for occurrence of stress-corrosion cracking - if, indeed, it is necessary at all.

Fractographic Studies

The experimental alloys were stressed at 90 percent of their 0.2 percent offset yield stress by constant deflection of sheet specimens in stainless steel three-point-loading fixtures. The compositions of the alloys and the exposed stress level for each are given in Table 24.

Specimens of these alloys were placed at random in a 5-liter stainless-steel autoclave which was then sealed and evacuated. Enough liquid N_2O_4 was placed in the autoclave to cover all of the specimens. The autoclave at 90 F was then pressurized to 250 psig with O_2 , and was placed in a water bath at 104 F and maintained at that temperature for 15 days. (These same specimens had previously been exposed to N_2O_4 without oxygen added and did not show signs of cracking after two weeks.)

When the specimens were removed from the autoclave there was a pronounced difference in the appearance of the specimens at the top of the autoclave and those at the bottom of the autoclave; both the specimens and the stainless steel holders at the bottom of the autoclave were darker than those at the top.

All of the specimens had cracked. The depth of cracks in the specimens at the bottom of the autoclave were deeper than those in specimens of the same alloy which were at the top of the autoclave. However, the primary modes of fracture were independent of the location within the autoclave and dependent only on specimen composition and stress level.

The Ti-4Al alloy failed entirely by an intergranular path as can be seen in Figure 32. However, at a higher magnification (Figure 33), it is evident that some transgranular slip has occurred. When 4 V is added to this alloy as a β stabilizer, the fracture mode appears to depend on the stress intensity at the root of the crack.

TABLE 24. TITANIUM ALLOYS EXPOSED TO N_2O_4

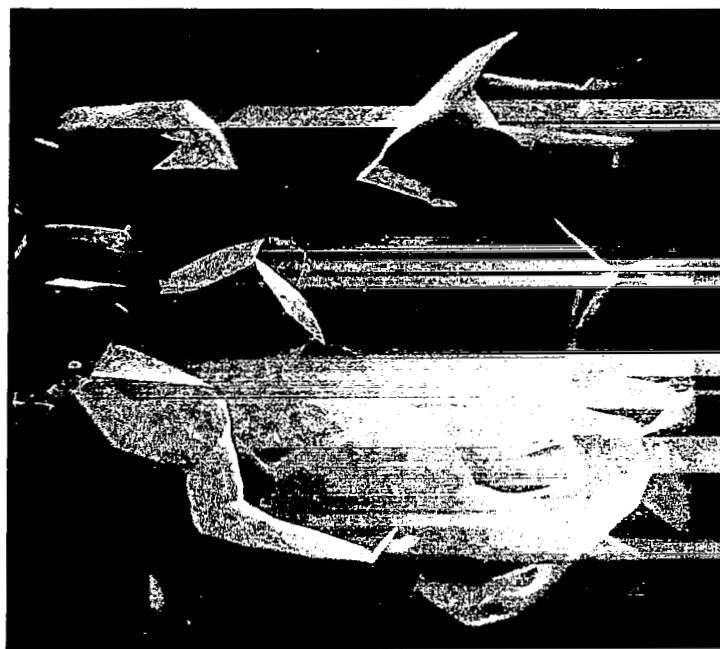
Alloy	Composition, weight percent	Stress Level, ksi
67	Ti-4Al	60
8	Ti-4Al-3Mo	99
9	Ti-4Al-4V	95
0	Ti-4Al-3Mo-1V	103
41	Ti-4Al-3Mo-1V	110
1	Ti-4Al-2Mo-2V	97
2	Ti-4Al-1.5Mo-0.5V	92
--*	Ti-6Al-4V	145
3	Ti-8Al	90
5	Ti-8Al-1Mo	107
21	Ti-8Al-2Mo	97
6	Ti-8Al-2V	107
78	Ti-8Al-1Mo-1V	122
81	Ti-8Al-1Mo-1V	111
4	Ti-8Al-3Mo-1V	127
77	Ti-8Al-1.5Mo-0.5V	117

*Commercially obtained material in solution-heat-treated-and-aged condition.

A high stress intensity factor (near the initiating edge of the fracture) appears to favor transgranular cleavage as shown in Figure 34. Lower stress intensity factors (near the root of the fracture in constant-deflection specimens) tend to favor intergranular fracture. Figure 35 illustrates the zone of transition between transgranular cleavage and intergranular cracking.

The Ti-8Al alloy with no β stabilizer also exhibited both transgranular and intergranular fracture. However, the transgranular fracture produces a surface pattern different from that found in the Ti-4Al-4V alloy. Figures 36a and 36b show two magnifications of the initiating edge of a crack in a Ti-8Al specimen. At the lower magnification it can be seen that both intergranular and transgranular fracture have occurred at the edge. The higher magnification shows a distinct pattern of main lines in the direction of fracture intersected by much closer spaced, fainter lines which indicate a stepwise propagation of the crack front. One possibility is a periodic buildup and cracking of an oxide film. Another possibility is periodic restricted slip. This rupture mode is believed to be associated with the initiation stage because as the crack deepens the fracture mode becomes predominantly intergranular as can be seen in Figure 37.

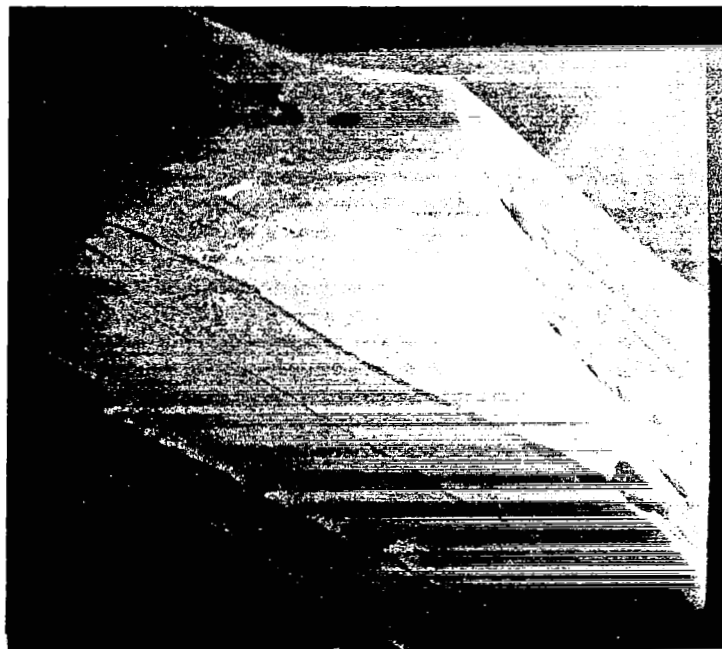
With β stabilizers added to the Ti-8Al alloy the mode of fracture becomes predominantly transgranular. At the initiating edge the fracture pattern is similar to the



500X

SEM-251

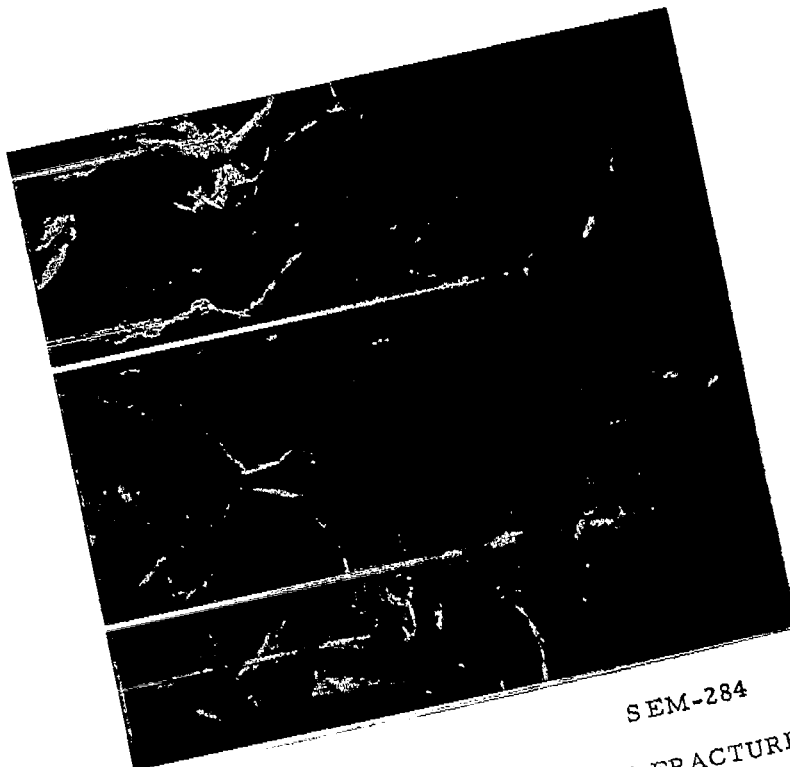
FIGURE 32. INTERGRANULAR CRACKING OF Ti-4Al IN $\text{N}_2\text{O}_4 + \text{O}_2$



500X

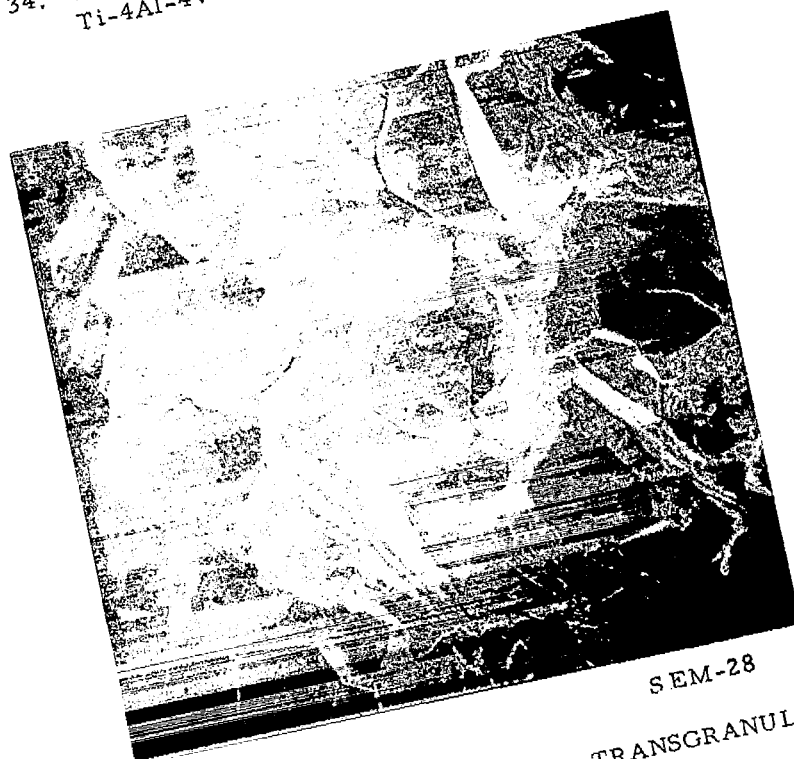
SEM-248

FIGURE 33. TRANSGRANULAR SLIP IN Ti-4Al
CRACKED IN $\text{N}_2\text{O}_4 + \text{O}_2$



SEM-284

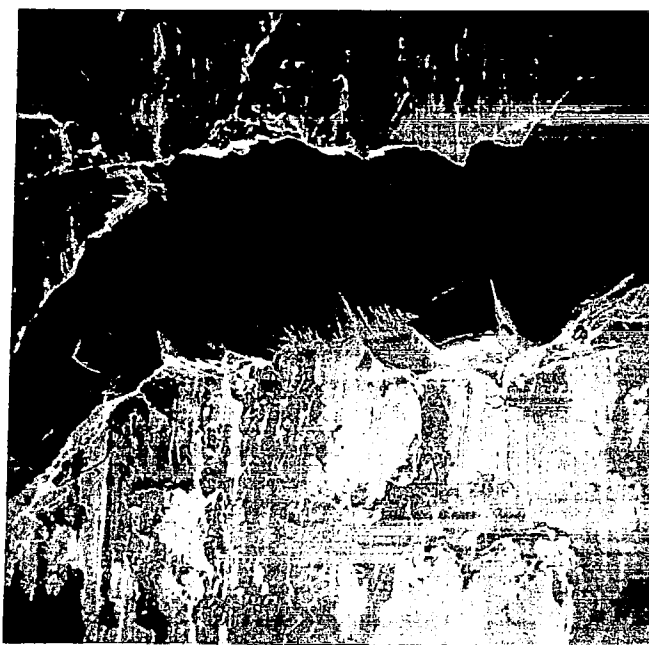
2000X
FIGURE 34. TRANSGRANULAR CLEAVAGE FRACTURE OF
Ti-4Al-4V IN $N_2O_4 + O_2$



SEM-28

2000X

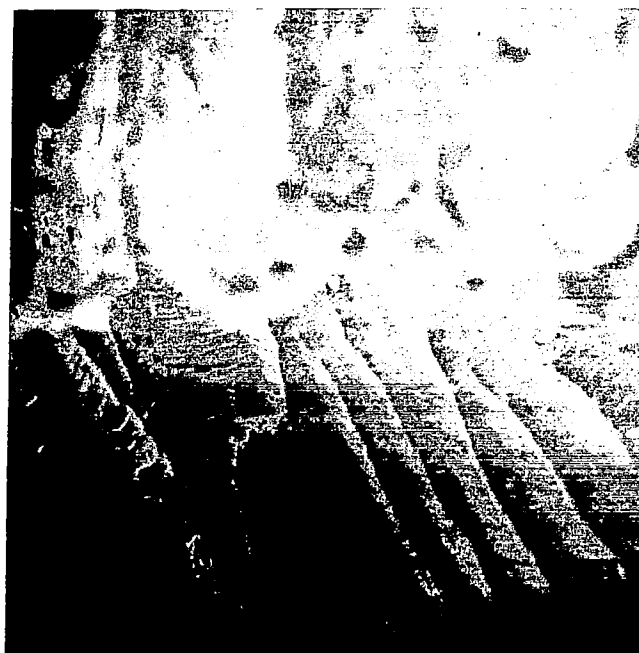
TRANSGRANULAR-TRANSGRANULAR FRACTURE
IN $N_2O_4 + O_2$



500X

SEM-229

(a)

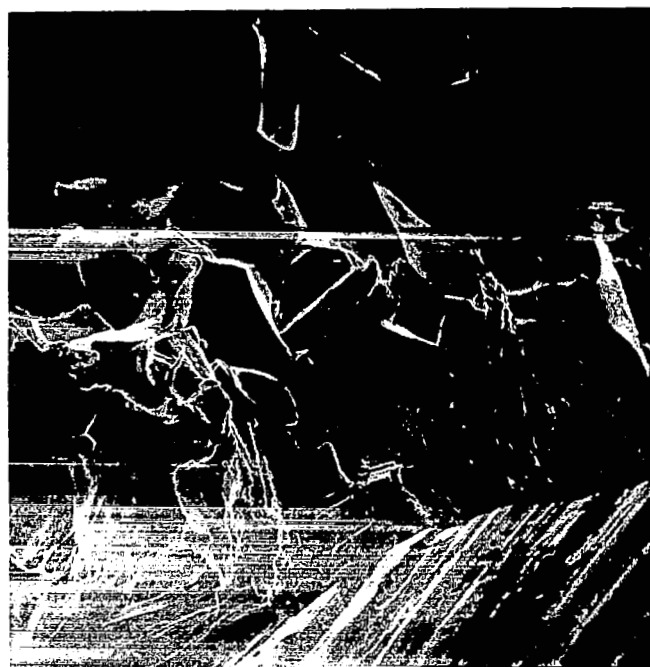


5000X

SEM-230

(b)

FIGURE 36. Ti-8Al CRACKED IN $N_2O_4 + O_2$



500X

SEM-238

FIGURE 37. Ti-8Al CRACKED IN $\text{N}_2\text{O}_4 + \text{O}_2$



2000X

SEM-278

FIGURE 38. BRITTLE FRACTURE IN Ti-8Al-1Mo-1V
CRACKED IN $\text{N}_2\text{O}_4 + \text{O}_2$

transgranular fracture in the Ti-8Al; however, when the crack progresses to a certain depth, it appears that a fast brittle cleavage occurs. Figure 38 shows a pattern typical of a fast brittle cleavage. The crack depths at which the brittle fracture mode started and stopped can be calculated from Figures 39a and 39b.

The stress-intensity factor at the bottom of a crack in these three-point-loaded constant-deflection specimens is

$$K_I = \frac{[D + a - w] 6ED (w - a)^3}{[3D - 4(w - a)] 9w^{1.5}} \left[35.2 \left(\frac{a}{w}\right) - 72 \left(\frac{a}{w}\right)^2 + 234 \left(\frac{a}{w}\right)^3 \right]^{1/2}$$

where

D = specimen deflection in inches

a = crack depth in inches

w = specimen thickness in inches

E = modulus of elasticity in ksi

K_I = ksi $\sqrt{\text{in.}}$ stress intensity factor.

The first part of the equation is derived from moment balances on a three-point load specimen and is

$$\frac{PL}{B} = \frac{[D - t] 6DEt^3}{[3D - 4t] 4L^2}$$

where

t is the remaining specimen thickness in inches

D is the deflection in inches

B is the thickness in inches

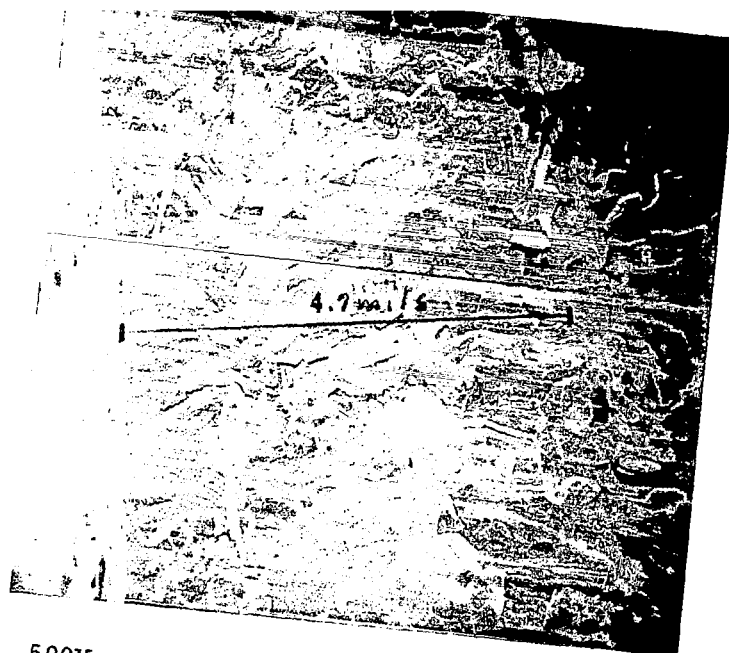
L is the distance between load points in inches

P is the required load in 1000 pounds.

The derivation is in the Appendix.

A plot of the stress-intensity factor as a function of crack depth is shown in Figure 40 for the Ti-8Al-1Mo-1V specimen.

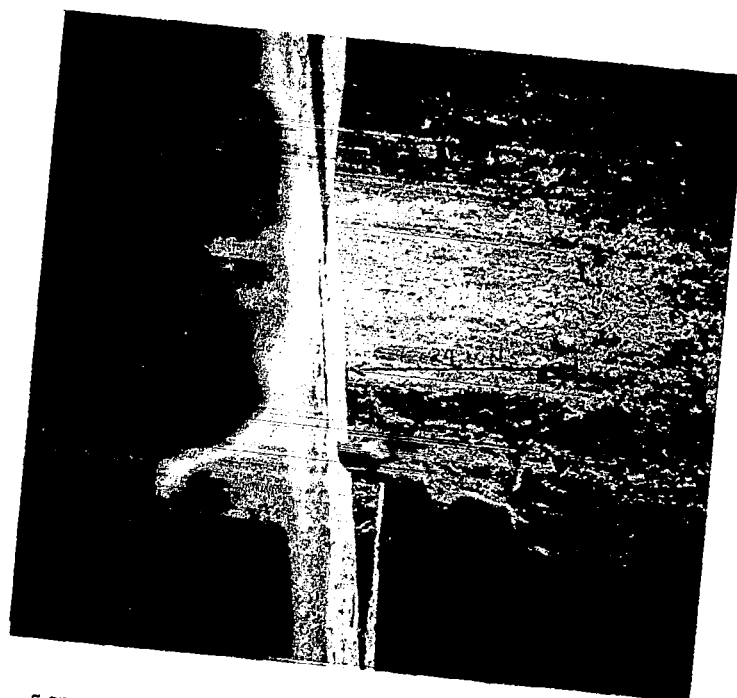
The stress-intensity factors at which the brittle fracture started and stopped are 19.4 and 19.9 ksi $\sqrt{\text{in.}}$ respectively. This behavior suggests that a critical stress-intensity factor for brittle mechanical fracture in N_2O_4 exists which is lower than it is in air. However, other modes of fracture occur which do not have a critical stress-intensity factor. The rate of transgranular initiation and intergranular propagation may be stress dependent but not as discrete values.



500X

SEM-255

(a)



50X

SEM-286

(b)

FIGURE 39. Ti-8Al-1Mo-1V CRACKED IN $N_2O_4 + O_2$,
SHOWING START AND STOP OF BRITTLE,
FRACTURE MODE

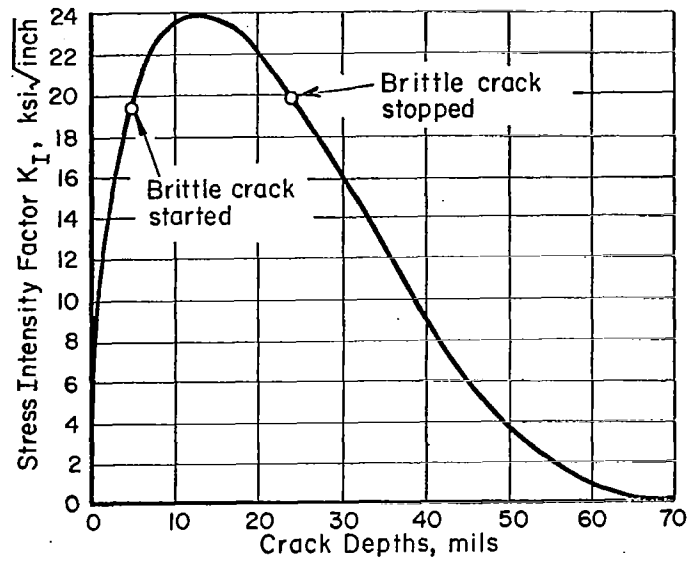


FIGURE 40. VARIATION IN STRESS INTENSITY FACTOR AS A FUNCTION OF CRACK DEPTH FOR 0.0715-INCH THICK Ti-8Al-1Mo-1V SPECIMEN DEFLECTED 0.15 INCH BY THREE-POINT LOADING

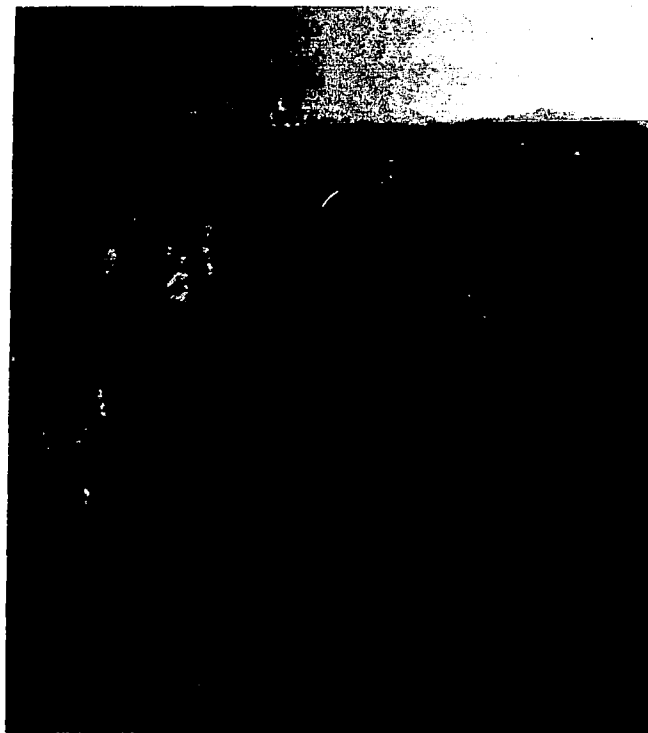


FIGURE 41. INITIATION EDGE OF Ti-8Al-3Mo-1V SPECIMEN CRACKED IN $N_2O_4 + O_2$

Figure 41 shows the initiation edge of a fracture surface of a Ti-8Al-3Mo-1V specimen. Again there is a distinct change in the transgranular fracture mode. At this crack depth, the stress-intensity factor is calculated to be $11.7 \text{ ksi}\sqrt{\text{in.}}$ for this specimen. The change in fracture mode was not nearly as evident as shown in these two examples. However, it is interesting to note that these values obtained in N_2O_4 correlate well with values for the same alloys obtained in salt water. It is likely that for the lower strength alloys the deflection of the specimens was not sufficient to cause brittle fracture and that slow chemical attack occurred, either by a transgranular or an intergranular path.

The transgranular fracture of the Ti-4Al-4V suggests that the beta phase is more susceptible to the chemical attack than are the grain boundaries of the all-alpha alloy, Ti-4Al.

Discussion of Results

The validity of the thermodynamic consideration that HNO_3 can be produced by the reaction of green N_2O_4 with H_2O and O_2 has been proven by experiment. Therefore, the thermodynamic consideration that red N_2O_4 which is contaminated with H_2O and O_2 contains HNO_3 has been substantiated by experiment. Experiments and thermodynamic calculations have indicated that the stress-corrosion-cracking of Ti-6Al-4V U-bends in N_2O_4 is associated with a $\text{HNO}_3/\text{H}_2\text{O}$ ratio $> (2500 \text{ to } 2800)$ and the presence of oxygen. From early experiments, it was believed that the $\text{HNO}_3/\text{H}_2\text{O}$ ratio played the major role in the stress-corrosion-cracking mechanism and that HNO_3 could possibly lead to hydrogen embrittlement of the titanium alloy. Although the hydrogen embrittlement theory cannot be conclusively ruled out at this stage, data from autoradiographic studies and potential studies do not substantiate this theory. Thus, autoradiographic studies using tritiated H_2O to produce tritiated HNO_3 did not show the presence of H_2 on fracture surfaces greater than the detection limit of 200 ppm. Furthermore, potential studies indicated that stress-corrosion cracking appears to occur at very noble potentials (+0.6 to +0.9 volt vs. $\text{Ag}/\text{Ag}/\text{Cl}$ and increasing with exposure time) which are well above the potential for the hydrogen evolution reaction. In aqueous environments, stress-corrosion cracking is usually associated with a smooth decrease of potential which ends with a drop when the metal completely fractures. It is possible in the N_2O_4 experiment, however, that the potential measured was the overall mixed potential and not very representative of potential changes near or within the crack tip.

An experiment conducted in green N_2O_4 with the addition of N_2O_5 , which would undoubtedly produce a large $\text{HNO}_3/\text{H}_2\text{O}$ ratio, produced no stress-corrosion cracking failures, thus indicating that the $\text{HNO}_3/\text{H}_2\text{O}$ ratio did not necessarily play the major role in the failure mechanism. It was noted in other experiments, however, that failures occurred in systems pressurized with O_2 and that the U-bend failures contained a larger number of cracks with larger oxygen pressures. Experiments conducted with purified N_2O_4 produced stress-corrosion-cracking failures of Ti-6Al-4V and Ti-75A, U-bend specimens in the presence of O_2 but not in the presence of helium. This data, although limited, suggested that O_2 played an important role in itself in the stress-corrosion-cracking mechanism.

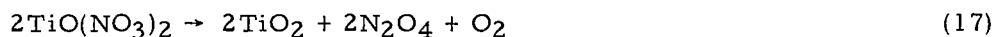
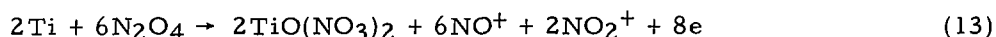
The production of an approximate 400 to 700 Å thick film on the fracture surface of failed U-bends, as revealed by interference colors, indicated that an aggressive environment must exist within the stress-corrosion crack. The crack walls therefore are not

readily passivated. If the potential value of +0.6 to +0.9 volt vs. Ag/AgCl is considered as reliable then the titanium probably dissolves in the TiO^{++} state. In the case of the Ti-6Al-4V alloy, the beta phase of the alloy appears to undergo preferential dissolution.

On the basis of the above data, the stress-corrosion-cracking mechanism should account for

- (1) The importance of the presence of O_2
- (2) The high oxidation state of the alloy
- (3) The production of a thick film on the fracture surface due to the presence of an aggressive environment within the crack.

A mechanism has been proposed which, although obviously tentative since the hydrogen embrittlement theory cannot be conclusively ruled out, is as follows:



It is believed that the production of bare Ti metal for a crack initiation point can occur through Reaction (17) proceeding in the reverse direction in the presence of a strained TiO_2 film. A nonprotective $\text{TiO}(\text{NO}_3)_2$ film is produced which reveals fresh bare Ti metal due to yielding of the crack tip by the applied stress. The crack tip undergoes electrochemical dissolution according to Reaction (13), and Reaction (14) is the most likely cathodic reaction occurring outside the crack. The corrosion potential for these reactions is likely to be noble and of the order of +0.8 volt vs. Ag/AgCl. Reaction (13), however, produces reducible ions within the crack and thus the crack sides undergo electrochemical dissolution according to Reaction (13), with Reactions (14), (15), and (16) acting as cathodic reactions. The dissolution Reaction (13) produces further reducible ions within the crack. The decomposition of the unstable $\text{TiO}(\text{NO}_3)_2$ film yields a stable TiO_2 film and O_2 which helps to depolarize cathodic reactions within the crack. However, insufficient O_2 is produced by Reaction (17) to account for all the local cathodic current. Thus, the difference in O_2 concentration between the bulk solution and the solution within the crack would favor the formation of a nonprotective film within the crack. It appears on this mechanistic basis that HNO_3 which is present in red N_2O_4 does not impart passivity to the stress-corrosion crack. It must also be noted that, in red N_2O_4 which has a large $\text{HNO}_3/\text{H}_2\text{O}$ ratio, the H_2O content of red N_2O_4 is very much smaller than that of green N_2O_4 , and then green N_2O_4 could impart passivation through its H_2O content.

Failures were observed for all of the experimental alloys stressed at 90 percent of their 0.2 percent offset yield stress and exposed to red N_2O_4 . The fracture mode of the alloys was dependent on the composition and stress level. Stress-intensity calculations

suggest that a critical stress-intensity factor for brittle mechanical fracture in N_2O_4 exists which is lower than the value in air. In the lower strength alloys, the stress level was not sufficient to cause a brittle fracture and slow chemical attack either by a transgranular or an intergranular path occurred.

Future Work on N_2O_4 Cracking Mechanism

Studies with Ti-6Al-4V alloy clearly indicate that the beta phase of this alloy is the most susceptible to dissolution in red N_2O_4 . Since there is a broad selection of experimental alpha/beta and beta alloys, the susceptibility of these phases in red N_2O_4 will be the prime objective of future study. The susceptibility of these alloys with regard to phase types can be studied as follows:

- (1) Exposure to red N_2O_4 under various strained conditions and subsequent analysis of the solutions for metallic ion content
- (2) Measurement of electrode potentials of combinations of the alloys in red N_2O_4 under the strain conditions used above
- (3) Determination of the polarization behavior of these alloys in red N_2O_4 with regard to type of phase.

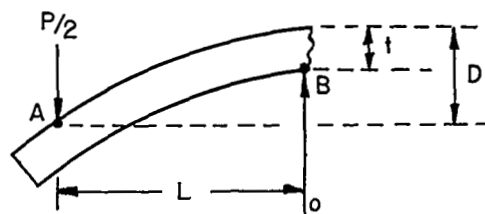
Thus, the susceptibility of the alloys can be determined with regard to structure and electrode potential. The susceptible potential (or range) for these alloys will thus be determined. By the application of current to these alloys, it should be possible to get them into a potential range where they are not susceptible, and so a means of protection can be found. The same data should, however, reveal why the alloys are susceptible (because the potential controls the oxidation state of the dissolving species) and thus the stress-corrosion-cracking mechanism can now be clarified with regard to alloy structure and composition.

Since the nature of the oxide film is undoubtedly important in the stress-corrosion-cracking mechanism, a similar study with alloys containing Ta or Pd additions is proposed. The filming properties of these additions can possibly result in an alloy which is not susceptible to stress-corrosion cracking based on our present theory. Fractographic studies of the failed alloys of course will still be continued with the scanning electron microscope to determine the type of failure.

REFERENCES

- (1) J. D. Boyd, et al., "The effect of Composition on the Mechanism of Stress-Corrosion Cracking of Titanium Alloys in N_2O_4 , and Aqueous and Hot Salt Environments", Annual Summary Report to National Aeronautics and Space Administration, Contract No. NASr-100(09), January, 1969.
- (2) M. J. Blackburn, "The Ordering Transformation in Titanium-Aluminum Alloys Containing up to 25 at.% Aluminum", Trans. AIME, 239, 1200 (1967).
- (3) G. Sanderson and J. C. Scully, "Hydride Formation in Thin Foils of Dilute Ti-Al Alloys", Trans. AIME 239, 1883 (1967).
- (4) J. D. Boyd, "Deformation-Assisted Nucleation of Titanium Hydride in an Alpha-Beta Titanium Alloy", Proceedings of the International Conference on Titanium, London, England, May, 1968, in press.
- (5) P. C. Gehlen, "The Crystallographic Structure of Ti_3Al ", Proceedings of the International Conference on Titanium, London, England, May, 1968, in press.
- (6) M. Hoch, "Statistical Model for Nonsubstitutional Solutions: (a) Interstitial Solutions, (b) Deviation from Stoichiometry in Inorganic Compounds", Trans. AIME, 230, 138 (1964).
- (7) H. Margolin and H. Portisch, "Hydrogen-Induced Expansions in Titanium-Aluminum Alloys", Trans. AIME, 242, 1901 (1968).
- (8) H. Brooks, Metal Interfaces, ASM, Cleveland (1952), p 50.
- (9) P. B. Hirsch, et al., Electron Microscopy of Thin Crystals, Butterworths, London (1965), p 341.
- (10) J. D. Boyd, "Precipitation of Hydrides in Titanium Alloys", submitted to ASM Transactions Quarterly.
- (11) A. Sandoz, "Subcritical Crack Propagation in Ti-8Al-1Mo-1V in Organic Environments, Salt Water and Inert Environments", Proceedings of Conference on Fundamental Aspects of Stress-Corrosion Cracking, NACE, Houston, 1969, p 684.
- (12) H. H. Johnson and A. M. Willner, "Moisture and Stable Crack Growth in a High Strength Steel", App. Mat. Res., January (1965), p 34.
- (13) K. R. Evans, "The Embrittlement and Fracture of Ti-8 pct Al Alloys", Trans. AIME, 245, 1297 (1969).
- (14) M. J. Blackburn and J. C. Williams, "Metallurgical Aspects of the Stress-Corrosion Cracking of Titanium Alloys", Proceedings of Conference on Fundamental Aspects of Stress-Corrosion Cracking, NACE, Houston, 1969, p 684.
- (15) K. R. Evans, "Deformation Mechanisms in Titanium and Titanium Aluminum Alloys", Trans. AIME, 242, 648, (1968).

- (16) E. N. Pugh, J.A.S. Green, and A. J. Sedriks, "Current Understanding of Stress-Corrosion Phenomena", to be published in Proceedings of the International Conference on Interfaces, Melbourne, Australia, August, 1969.
- (17) G. F. Pittinato, "The Reactivity of Hydrogen with Ti-6Al-4V Under Fatigue Cycling at Ambient and Cryogenic Temperatures", ASM Trans., 62, 410 (1969).
- (18) "A Study of the Mechanism of Chemical Reactivity of Nitrogen Tetroxide with Titanium Alloys", Fourth Quarterly Report, NAS8-21207, Hercules, Inc, November 1, 1968.
- (19) E. T. Chang and N. A. Gokeen, J. Phys. Chem., 70, 2394 (1966).
- (20) D. J. Ives and G. J. Janz, Reference Electrodes, Academic Press, New York (1961), p 205.
- (21) L. F. Audrieth, "Inorganic Syntheses", 3, 78, McGraw Hill (1950).



Moment Balances

Around Point A

$$PL = B \int_0^t \sigma(D-t+x)dx$$

Around Point B

$$\frac{PL}{2} = B \int_0^t \sigma x dx$$

$$\sigma = a + bx$$

$$\int_0^t (a + bx) (D-t+x)dx = 2 \int_0^t (a+bx)x dx$$

$$a(D-t)t + \frac{b(D-t)t^2}{2} + \frac{at^2}{2} + b \frac{t^3}{3} = \frac{2at^2}{2} + \frac{bt^3}{3}$$

$$a \left[(D-t)t + \frac{t^2}{2} - \frac{2t^2}{2} \right] = b \left[\frac{t^3}{3} - \frac{(D-t)t^2}{2} \right]$$

$$a [6Dt - 6t^2 + 3t^2 - 6t^2] = b [2t^3 - 3Dt^2 + 3t^3]$$

$$a [6D - 9t] = b [5t^2 - 3Dt]$$

$$a = b \frac{[5t^2 - 3Dt]}{[6D - 9t]}$$

$$a = \frac{b [5t^2 - 3Dt]}{[6D - 9t]}$$

$$a = \sigma_o - bt$$

$$\sigma_o - bt = \frac{bt [5t - 3D]}{[6D - 9t]}$$

$$\sigma_o = 1 + \frac{[5t - 3D]}{[6D - 9t]} bt$$

$$\sigma_o = \frac{[6D - 9t + 5t - 3D]}{6D - 9t} bt$$

$$\sigma_o = \frac{[3D - 4t]}{[6D - 9t]} bt$$

$$b = \frac{\sigma_o}{t} \left[\frac{6D - 9t}{3D - 4t} \right]$$

$$a = \sigma_o - bt$$

$$a = \sigma_o - \frac{\sigma_o (6D - 9t)}{(3D - 4t)}$$

$$a = \frac{[3D - 4t - 6D + 9t]}{(3D - 4t)} \sigma_o$$

$$a = \left[\frac{5t - 3D}{3D - 4t} \right] \sigma_o$$

$$\frac{PL}{B} = 2 \int_0^t (a + bx) x dx$$

$$\frac{PL}{B} = \frac{2at^2}{2} + \frac{2bt^3}{3}$$

$$\frac{PL}{B} = \sigma_o \left[\frac{5t - 3D}{3D - 4t} \right] t^2 + \frac{2\sigma_o}{3} \left[\frac{6D - 9t}{3D - 4t} \right] t^2$$

$$\frac{PL}{B} = \frac{[5t - 3D + 4D - 6t]}{[3D - 4t]} \sigma_o t^2$$

$$\frac{PL}{B} = \left[\frac{D - t}{3D - 4t} \right] \sigma_o t^2$$

$$D = \frac{4\sigma_o L^2}{6Et}$$

$$\frac{PL}{B} = \left[\frac{D - t}{3D - 4t} \right] \frac{6Dt^3 E}{4L^2}$$

$$*K = \frac{PL}{BW}^{3/2} \left[\frac{1}{(1 - \nu^2)} \left(31.7 \left(\frac{a}{W} \right) - 64.8 \left(\frac{a}{W} \right)^2 + 211 \left(\frac{a}{W} \right) \right) \right]^{1/2}$$

assume $\nu = .33$

From Piper, D. E., Smith, S. H., and Carter, R. V., "Corrosion Fatigue and Stress-Corrosion Cracking in Aqueous Environment", 1966 National Metals Congress, Chicago, October 31 to November 3.